CONTROL AND ESTIMATION METHODS TOWARDS SAFE ROBOT-ASSISTED EYE SURGERY

by

Ali Ebrahimi

A dissertation submitted to The Johns Hopkins University in conformity with the requirements for the degree of Doctor of Philosophy

Baltimore, Maryland

August, 2022

Abstract

Vitreoretinal surgery is among the most delicate surgical tasks in which physiological hand tremor may severely diminish surgeon performance and put the eye at high risk of injury. Unerring targeting accuracy is required to perform precise operations on micro-scale tissues. Tool tip to tissue interaction forces are usually below human tactile perception, which may result in exertion of excessive forces to the retinal tissue leading to irreversible damages. Notable challenges during retinal surgery lend themselves to robotic assistance which has proven beneficial in providing a safe steady-hand manipulation. Efficient assistance from the robots heavily relies on accurate sensing and intelligent control algorithms of important surgery states and situations (e.g. instrument tip position measurements and control of interaction forces). This dissertation provides novel control and state estimation methods to improve safety during robot-assisted eye surgery.

The integration of robotics into retinal microsurgery leads to a reduction in surgeon perception of tool-to-tissue forces at sclera. This blunting of human tactile sensory input, which is due to the inflexible inertia of the robot, is a potential iatrogenic risk during robotic eye surgery. To address this issue, a sensorized surgical instrument equipped with Fiber Bragg Grating (FBG) sensors, which is capable of measuring the sclera forces and instrument insertion depth into the eye, is integrated to the Steady-Hand Eye Robot (SHER). An adaptive control scheme is then customized and implemented on the robot that is intended to autonomously mitigate the risk of unsafe scleral forces and excessive insertion of the instrument. Various preliminary and multi-user clinician studies are then conducted to evaluate the effectiveness of the control method during mock retinal surgery procedures.

In addition, due to inherent flexibility and the resulting deflection of eye surgical instruments as well as the need for targeting accuracy, we have developed a method to enhance deflected instrument tip position estimation. Using an iterative method and microscope data, we develop a calibration- and registration-independent (RI) framework to provide online estimates of the instrument stiffness (least squares and adaptive). The estimations are then combined with a state-space model for tip position evolution obtained based on the forward kinematics (FWK) of the robot and FBG sensor measurements. This is accomplished using a Kalman Filtering (KF) approach to improve the instrument tip position estimation during robotic surgery. The entire framework is independent of camera-to-robot coordinate frame registration and is evaluated during various phantom experiments to demonstrate its effectiveness.

ABSTRACT

Primary Reader and Advisor:

- Iulian Iordachita, PhD

  Research Professor

  Department of Mechanical Engineering

  Johns Hopkins University

Secondary Readers:

- Russell H. Taylor, PhD

  Johns C. Malone Professor

  Department of Computer Science

  Johns Hopkins University

- Louis L. Whitcomb, PhD

  Professor

  Department of Mechanical Engineering

  Johns Hopkins University

Acknowledgments

First and foremost, I would like to express my sincere gratitude to my supervisor Dr. Iulian Iordachita for offering me the PhD position in his lab and giving me this perfect opportunity to pursue my education at the Laboratory for Computational Sensing and Robotics (LCSR). I am immensely thankful for his expert guidance throughout my research, and his gracious support and patience during the challenging term of PhD. Huge special thanks goes to Dr. Peter Gehlbach for his continued support and help and for his constructive comments and feedback that guided my research towards a correct clinically-relevant path. I think I have been very lucky and privileged to work with extraordinary colleagues, exceptional professors, and outstanding staff at LCSR to conduct research on medical robotics and to learn from excellent and knowledgeable people during the past five years. I am very grateful to all of those individuals, without whom this work would have not been accomplished.

Secondly, I would like to specially thank Dr. Russell Taylor and Dr. Louis Whitcomb for generously agreeing to read the thesis and to be a committee member for my defense, and more importantly for providing me with priceless insightful advises for my future career and research feedback during the past few years. Many thanks also to my second advisor Dr. Marin Kobilarov from whom I learned a lot.

A huge thank you to my great collaborators, Dr. Nirav Patel, Dr. Changyan He, Dr. Marina Roizenblatt, and Dr. Muller Urias who substantially contributed to the development of this work, and from whom I learned a lot. I am very grateful to the researchers and collaborators from other labs for their assistance and help during my PhD including Dr. Shahriar Sefati, Dr. Farshid Alambeigi, Dr. Adnan Munawar, and Anton Duguet. I highly appreciate that they helped with various research problems that I faced and generously spared the time to work with me through those problems. I also want to thank the current and former members of the Advanced Medical Instrumentation and Robotics (AMIRo) Laboratory, Emily Yang, Dr. AliReza Alamdar, Dr. Gang Li, Dimitri Lezcano, Yanzhou Wang, Jiahao Wu, Mojtaba Esfandiari for being excellent lab mates and for their support and help.

I owe a big thank you to the outstanding staff of LCSR as well as Mechanical Engineering Department, Ashley Moriarty, Lorrie Dodd, Alison Morrow, Jordan Card, Mike Bernard, Kevin Adams, John Soos, and Alison Wampler for their great professional competence in handling the substantial load of administrative work and academic advising.

I want to greatly thank my close friends in Baltimore, Alireza Mortazavi, Navid Orduie, Babak Ghamari, Mohammad Saleh with whom I share a lot of good and fun memories. I would also like to acknowledge and appreciate the support I received for conducting research from National Institute of Health (NIH), the Link Foundation, and the Johns Hopkins University internal funds.

I have always been and will be greatly thankful to my beloved mother and father for everything they have generously done for my life and success. I do not think I can ever do anything that will make up for the things they have done for me, and I always owe them whatever I achieve in life. Same goes to my dear sister for her kind support and invaluable influence on me. I would also like to sincerely thank my very kind and empathetic grandmother for her continued support in every single challenge and difficulty that I have encountered.

Ali Ebrahimi

August 2022

Dedication

To Mom, Dad, Shima, and Grandma

Contents

List of Tables

List of Figures

Chapter 1

Introduction

1.1 Vitreoretinal Surgery

Ophthalmic surgical procedures are among the most challenging surgical tasks [1] as they target delicate, non-regenerative, micro-scale tissues. At the same time, they are among the most commonly occurring surgical tasks worldwide [2, 3]. Due to the required micro-scale tissue manipulation within the confined area of the eyeball as well as milli-Newton scale interaction forces, these procedures pose a challenge to human visual acuity, physical dexterity and motor coordination [4]. Despite all of these challenges, huge advancements have been made within special fields of ophthalmic surgery in the past few decades [5]. For instance, phacoemulsification has revolutionized the field of cataract surgery by providing much rapid patient recovery and near perfect visual outcome [5, 6]. However, some sub-specialities in ophthalmic surgery, e.g. vitreoretial surgery, have unresolved challenges and difficulties.

Vitreoretinal eye surgery is one of the most technically difficult microsurgeries and refers to a group of intraocular surgical procedures that are done deep inside the eye's interior. Vitreoretianl surgery is the standard of care for multitude of retinal disorders including but not limited to diabetic retinopathy, retinal detachments or tears, age-related macular degeneration (AMD), and macular holes. In developed countries, it is reported that diabetic retinopathy and age-related macular degeneration are among the most prevalent reasons for loss of vision [7–10]. It is expected that the demographic trends in the

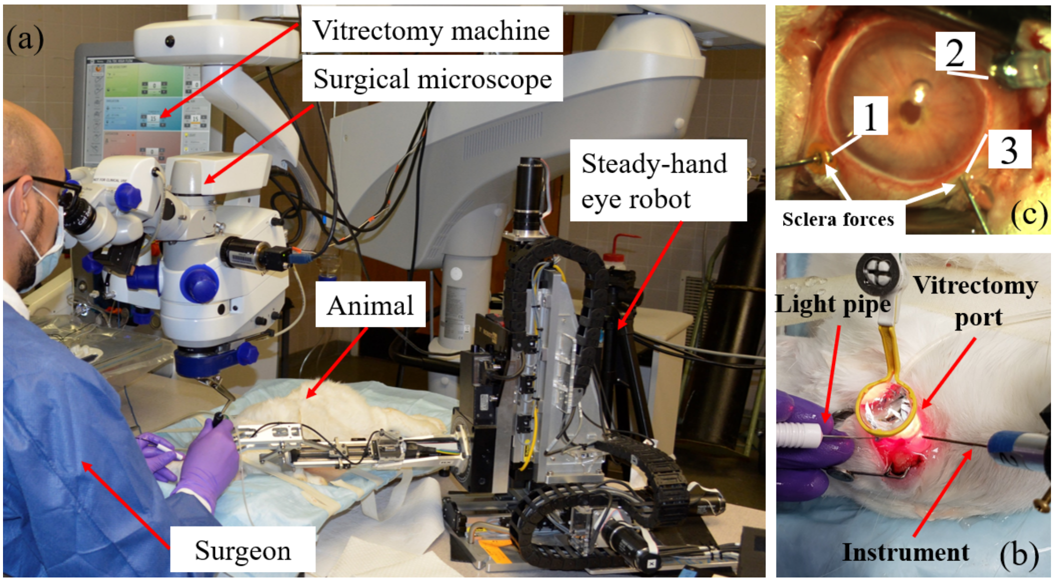

Figure 1.1: Vitreoretinal surgery. (a) The surgeon is using a robot to perform the surgery on an animal while visualizing the surgical field via a stereoscopic microscope. (b) Close-up view of the instruments. (c) Three sclerotomy ports on the eye and the place where the sclera forces are exerted by the tool shaft.

developing world will increase the occurrence of retinal diseases [11,12]. Vitreoretinal surgery entails delicate tissue manipulation as well as advanced and highly sensitive procedures. Fine and precise motion is required to manipulate extremely delicate tissue within the small and constrained space of the eye. These procedures are often accompanied with forces that are below human tactile perception [4]. The surgical tasks related to vitreoretinal surgery are conducted in the areas of the eye where the vitreous and retina are located, as depicted in Fig 1.2.

Virteoretinal surgery procedures are usually performed bimanually. Surgeons hold primary surgical instrument in their dominant hand and a endo-illuminator, e.g., a fiber-optic light pipe in their other hand to illuminate the

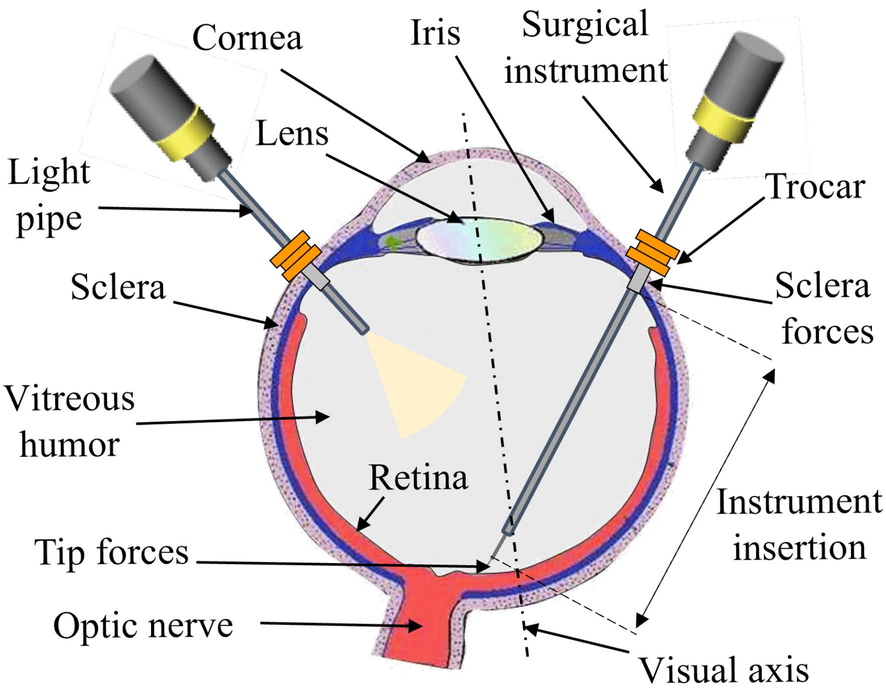

Figure 1.2: Schematic illustration of human eye and surgical instruments setup for retinal surgery. The picture shows where the sclera and tip forces are exerted. (Image credit to [1])

target area on the retina. A typical environment of vitreoretinal surgery is depicted in Fig. 1.1. To provide a magnified view of the eyeball interior a surgical microscope is placed on top of the patient head. Surgeons usually move the microscope up and down and use different lenses to obtain the required magnification, depth perception, field of view, and clarity of view. This is always a compromise because, for example, quite limited field of view is achieved once high magnification is configured for fine surgeries. The surgeon sits behind the patients head and performs the surgical tasks bimanually while visualizing the the surgical field through the microscope. A vitrectomy operation is commonly performed prior to any vitreoretianl surgical procedure in order to suction out the jelly-like vitreous fluid to make it easier to reach to the retina and repair it [13]. In order to insert the required instruments into the eyeball usually three small incision entry points (three-port approach) are made in the pars plana. One port is for the primary surgical tool, such as a vitreous cutter, pick, forceps, scissors, laser probe, and so forth. The other sclerotomy is for the endo-illuminator, which is held by the surgeon throughout the surgery. The third port is an infusion sclerotomy line, which supplies saline solution in order to maintain the pressure inside of the eye during and after vitrectomy. Using the two instruments (primary instrument and light pipe), surgeons try to make coordinated motions to move and reorient the eyeball such the desired targeted area is within their field of view under the microscope. Then, they can proceed with performing the required treatments and operations such as retinal vein cannulation, subretianl injection, membrane peeling, laser photocoagulation, etc. It is noted that in ophthalmic surgical procedures 20 to 25 Ga instruments are used, which range from 0.9 to 0.5 mm in diameter.

1.2 Vein Cannulation

Retinal Vein Occlusion (RVO) is becoming increasingly prevalent and it has been reported to be the second most common retinal vascular occlusive disease after diabetic retinopathy in the elderly [14]. RVO occurs when clots are formed in the central or branch retinal veins [15] or due to other reasons such as thickening of the crossing artery, low flow, hyper-coagulability, or thrombosis in the retinal veins of the eye. Branch RVO (BRVO) or central RVO (CRVO) can lead to detrimental visual outcomes and are often accompanied by blurred and distorted vision [16]. The number of people affected by RVO is reported 16.4 million people worldwide [17], and it has a prevalence of 1.8% and 0.5% for CRVO and BRVO, respectively [18]. On the basis of a sample of 4439 patients, the Beijing Eye Study declares that the 10-year incidence of BRVO is 1.6 per 100 subjects and the incidence of CRVO is 0.3 per 100 people [19]. In BRVO the clots are formed where two veins and arteries cross, and in CRVO the clots are made where the central vein enters the lamina cribrosa to exit the eye [20]. The contralateral eye has a 7% chance of developing RVO within 3 years when RVO occurs in one eye [21]. In many cases, macular edema and death of retianl cells are among the consequences of RVO. Other serious complications of RVO are neovascularization, vitreous hemorrhage, and retinal detachment [16, 22].

At the present time RVO does not have a surgical option as standard of care to directly resolve the occlusion. However, it relies indirectly on treatment of complications of the underlying condition to maintain vision. These treatments include photocoagulation, hemodilution, radial optic neurotomy, vitrectomy and intra-vitreal injections [23–27]. Among the widely effective treatments against secondary neovascularization and retinal oedema are intravitreal injections with anti-vascular endothelial growth factor (VEGF) or corticosteroids and retinal laser photocoagulation [28]. Some researchers, on the other hand, have tried to remove or dissolve the clot in order to treat the cause. Radial optic neurotomy, arteriovenous sheathotomy and chorioretinal venous anastomosis are all non-thrombolytic mechanical approaches either to bypass the interrupted circulation or to reduce the compressive forces of the adjacent artery on the affected vein [29–32]. Among the other treatments for RVO that targets the causes of the disease are intravitreal injection of recombinant tissue plasminogen activator (rtPA) to restore blood flow and systemic or local administration of intravenous rtPA [33–35]. The latter is possible when performing a retinal vein cannulation (RVC) and is referred to as retinal endovascular surgery (REVS). The procedure for conducting RVO is described as follows:

1. Inserting a cannula with a sharp tip into the eyeball thorough the sclerotomy port and bringing it in the vicinity of the target area.

2. Precisely puncturing the vessel with the cannula tip and inserting the tip to a desired and safe depth into the vessel.

3. Holding the cannula in place for several minutes for infusion of the clot-dissolving tissue plasminogen activator (t-PA) directly into the occluded

vein.

1.2.1 Challenges in Vein Cannulation

The skills required to perform the relevant micro surgical tasks in RVC mentioned in Section 1.2 are at the limit of human motor capabilities. Injection into a vessel with diameter of approximately $150\ \mu m$ and maintaining the needle tip into the vessel includes operations that are at the limit of human performance. There are two main challenges that can severely hamper a successful RVC, which are delineated as follows:

- First, for an ophthalmic surgeon, a root mean squared (RMS) of $182\ \mu m$ was measured for tremor amplitude [36], which is a comparable value when considering the retinal vessels diameters (i.e., between $50 - 150\ \mu m$ [37]). This amount of tremor makes it very difficult for surgeons to accurately target the goal position for puncture and to maintain the needle tip inside the vessel throughout the drug delivery, which can take several minutes [34].

- The second challenge stems from the fact that the interaction forces between the needle tip and the vessel are too small for human tactile perception (below $10\ mN$ [38, 39]). This makes it extremely difficult for surgeons to detect the instant when puncture takes place, to appropriately pierce the needle into the desired depth and to inject the medicine inside of the vessel. In contrary to retinal vessel cannulation, during conventional venipuncture happening on larger structures the resulting tactile forces are within the human tactile perception range and are familiar to experienced phlebotomists. Specifically, the clinician can feel the moment of vessel puncture [40].

Therefore, a surgeon's physiological hand tremor, limited motor control, and imperceptible forces which all might be intensified by visual, physical, and mental fatigue may put the eye at high risk of sight-damaging iatrogenic trauma. Due to the present technical difficulties and human limitations for performing ophthalmic surgical procedures specially vitreoretianl practices, it may be beneficial to integrate advanced technological systems and sensorized instruments into the standard of care for such surgeries. Consistent monitoring of the interaction forces between the instrument and the surrounding delicate tissue using sensor-equipped instruments can potentially raise the surgeon's awareness of the interaction force variations and to inform them of the moment of venous puncture during RVC. On the other hand, robotic platforms and technological devices may be useful in providing a steady-hand tremor-free operation where high precision for instrument targeting can be attained. In the following sections, related works in terms of technology development in the field of robot-assisted eye surgery are provided.

1.3 Technology Advancement in Retinal Surgery

1.3.1 Robot-assisted Eye Surgery

In order to overcome physiological human constraints, advanced robotic platforms have been engineered to suppress tremor and enhance targeting accuracy of the instrument that will function inside of a very small and fragile eyeball. Ueta et al. [41] report that a robotic platform has obtained more accurate retinal vessel cannulation in porcine eyes as compared to freehand. Similarly, Jacobsen et al. [42] report that robot-assisted vitreoretinal surgery improves precision and limits tissue damage, albeit at the cost of increased surgical time. The developed robotic systems for such purposes are broadly divided into tele-operated, cooperatively controlled, and handheld robots categories. In the tele-operated approaches (e.g., [43–49]) the surgeon manipulates the robot from a remote location. The Steady-Hand Eye Robot (SHER) [50] developed at the Johns Hopkins University (Fig. 1.1) and also the KU Leuven eye-surgical robot [51] are notable examples of collaborative platforms. These robots are characterized by a direct human-machine interface where the surgical tool can be attached to the robot and the surgeon and the robot share control of the instrument [39, 50, 52–55]. In addition, the first clinically-approved collaborative robots for in-human eye surgery has been designed and successfully evaluated by Edwards et al. [56] and Gijbels et al. [51]. Using the Preceyes Surgical System the results of a first-in-human study of robot-assisted retinal surgery performed through a telemanipulation at Oxford's John Radcliffe Hospital was reported in [56]. In January 2017, eye surgeons at University Hospitals Leuven were the first to demonstrate robot-assisted RVC in human patients using the system described at [51]. In contrast to table-mounted robots, handheld devices have also been engineered and developed, which provide a steady needle tip motion by actively suppressing the surgeon's physiological hand tremor [57–65].

1.3.2 Force Sensing and Visualization

In order to augment the force-sensing and visual perception of the surgical procedure in ophthalmic surgery several studies have been conducted. As mentioned in Section 1.2.1, some tool-to-tissue interaction forces in vitreoretinal surgery are rendered imperceptible. It is noted that in eye surgical procedures the instrument is inserted through a sclretomoy port into the eye. There are two main locations that interaction forces are exerted on the instrument. The first location is at the trocar (Fig. 1.2) where the sclera forces are applied to the tool shaft having tens to hundreds of milli-Newton order of magnitude [66]. Other forces are located at the tip of the instrument where the target tissue operation is performed (Fig. 1.2). During vitreoretinal surgery procedures, the tip forces can be less than 10 mN (based on animal studies reported in [67]). Based on another in vitro retinal manipulation conducted on porcine cadaver eyes, around three quarters of all of the measured interaction forces were below 7.5 mN [4]. Therefore, a force sensor should have a high resolution to be able to measure the very fine forces at the tip of the instrument. Moreover, it should be able to distinguish between the tip and sclera forces. The latter rules out the option of placing a force sensor on the instrument handle because it will not be able to differentiate between the tip and slcera forces. This will be even exacerbated because the sclera forces are larger in magnitude than the tip forces resulting in low transmission and detection of the tip forces if the force sensor is mounted on the instrument handle. For this reason, to measure the tip forces the force sensor should be positioned in the vicinity of the tool tip inside of the instrument handle. This will result in more rigorous dimensional requirements for the force while necessitating biocompatibility and safety.

Fiber Bragg Grating (FBG) optical sensors are very sensitive strain (less than $1\mu\epsilon$) and temperature variation detectors. They are very small in diameter ($\Phi\, 60-200\mu m$) and hence can fit through confined spaces of the eye and thin openings. Moreover, they fulfill the biocompatibility and safety requirements as well. They have attracted increasing interest in various disciplines and applications in robotic surgeries including force sensing [54, 68, 69], needle shape

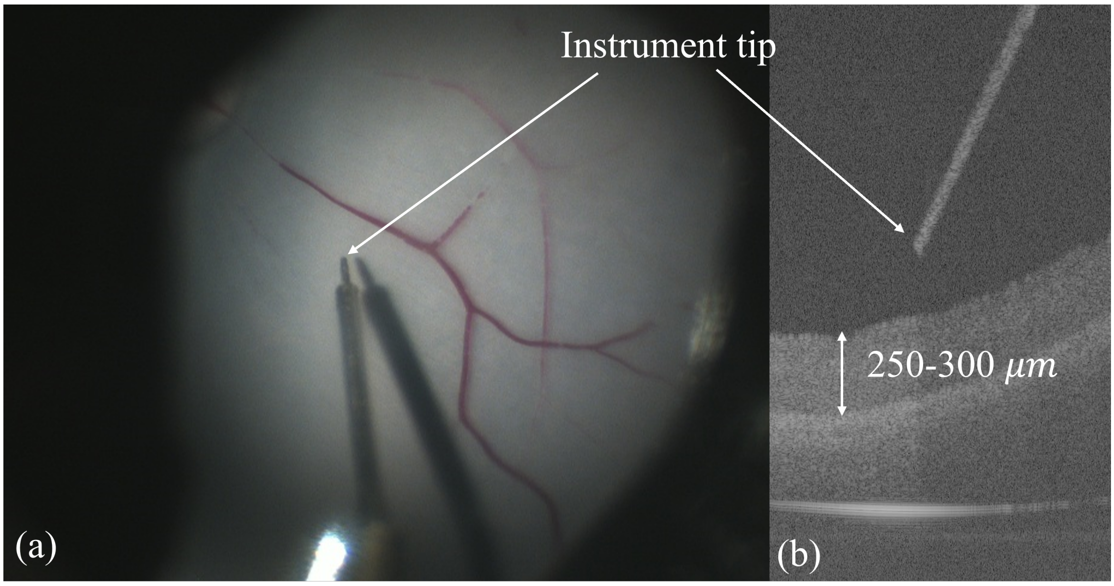

Figure 1.3: Visualization during ophthalmic surgery. (a) A top-down view of the retinal vessels and the surgical instrument inside of the eye using the stereo surgical microscope. (b) Cross-sectional OCT B-scan of the instrument showing the instrument and retinal layers. Courtesy of Peiyao Zhang.

sensing [70,71], and temperature variations sensing [72]. Attaching FBG fibers along a customized ophtalmic surgical instrument, it was shown the possibility of simultaneous measurement of tool tip and sclera forces with milli-Newton accuracy [73]. The retinal puncture moments in RVC were detected using an FBG-quipped cannulation needle [74].

As far as visualization is concerned, depth perception is still challenging in eye surgery because of the vertical enface view although advanced technological devices provide high-resolution stereo view of the eyeball interior [75]. As an alternative imaging modality, optical coherence tomography (OCT) has been integrated to surgical instruments and microscopes, which provides high-resolution cross-sectional 2D images (B-Scan) and therefore depth information in real time [75–77]. However, OCT scan range is limited, requires an an extended processing time, and is not cost-effective [78]. In order to provide visual feedback during ophthalmic interventions, intraoperative optical coherence tomography (iOCT) has also been used in various studies [79–81]. To date iOCT is the only imaging modality in the literature, which is able to detect small retinal structures at micrometer resolution while providing live-feedback during surgery [82]. A picture showing top-down microscope view and the OCT view of a surgical tool during in-vitro porcine eye manipulation is shown in Fig. 1.3.

1.3.3 Robot-assisted Vein Cannulation

In [83] an OCT-guided cannulation of blood vessels was shown in ex-vivo porcine eyes using a developed teleoperated robotic system. In [84], subretinal injection for retinal detachment as a main step for RPE replacement was reported during in vivo rabbit experiments using a co-manipulated robot. In contrary to common design of serially-actuated robots that manipulate conventional vitreoretinal tools, in [44] a subretinal injection was presented using a magnetically-navigated flexible cannula. In [44], both semi-automated and non-automated injection were reported through microscope-guided and intraoperative OCT-guided injections in ex-vivo porcine eyes. Becker et al. [85]

used a stereo camera tracking system to provide smooth, scaled motion during the retinal vessel injection in ex-vivo porcine eyes using a handheld tremor-cancelling robotic device. In [41], capability of a parallel robotic system to assist in micro cannulation of retinal vessel in ex vivo porcine eyes was evaluated.

In [48,86], a tele-manipulated laser-controlled robotic system was presented and retinal vein cannulation was performed in porcine eyes under stereo camera system, which is typical of conventional interocular surgery. The work done in [48] can be considered the first bilateral robot-assisted vein cannulation demonstration in which the surgeon can tele-manipulate two surgical instrument (a micro-syringe for vein cannulation and a light pipe). In another bilateral study in [87], the capability of accurately (micron-order) approaching a target on the fundus of an in-vitro eye model using a bilateral tele-manipulated robotic system was evaluated.

In [88, 89] the authors developed Preceyes micromanipulator and used it for retinal vein cannulation of porcine eyes by positioning a glass catheter tip using a robotic controlled micromanipulator. The first in-human subretinal injection of tissue plasminogen activator (tPA) for three human patients was reported in [56] during a telemanipulation robot-assisted retinal surgery. In [56], the authors used the Preceyes system developed in [88] for cannulation in human patiens. In another recent study [51], a unilateral tele-manipulated system was used to perform retinal vein cannulation in human patients after the system was used in previous in vivo porcine eyes experimets [15].

The feasibility of using learning from demonstration and reinforcement learning with an industrial robot to perform OCT-guided needle insertions to a target depth is presented in [90]. [91] reports that 4D microscope-integrated OCT significantly improves the control of surgical tool when surgeons are asked to manually place the instrument hundreds of microns above the retina during ex vivo porcine eye experiments. In contrast to microscope-mounted OCT system, [83] reports placing the OCT imaging probe internal to the surgical forceps and the evaluation of the benefits of OCT-integrated forceps combined with a tele-manipulated robotic system. [83] reports that the combination of OCT and robots dramatically improves phantom membrane peeling and retina approaching precision during ex vivo goat experiments.

1.4 Control, Estimation, and Autonomy in Robotic Ophthalmic Surgery

Although many of the above-mentioned studies in the literature have focused on hardware and sensor development in which surgeons benefit from a steady-hand manipulation by the resulting suppression of involuntary hand tremor, less attention has been paid to control and sensing algorithms development. Development of advanced control methods can augment robot functionalities potentially resulting in autonomous or semi-autonomous surgical procedures. Robotic systems can potentially broaden the present range of offered treatments and also provide automated procedures [92], e.g. automatic light probe holding application [78,93], automated laser photocoagulation [94], retinal vessel cannulation [41], and autonomous surgical tool navigation [95], among other applications.

When robotic assistance is used in vitreoretinal surgery, the surgeon will experience reduced sensory input that is otherwise derived from the tool's interaction with the eye wall (sclera). It has been shown that at present robot-assisted procedures exert larger scleral forces compared to manual surgeries [96]. In order to safely and reliably apply robots to ophthalmic procedures, application-specific control algorithms and sensing capabilities should be integrated into the robots to autonomously maintain, for example, interaction forces (including sclera forces and tip forces shown in Fig. 1.2), and instrument insertion depth (Fig. 1.2) into the eyeball within safe ranges.

Other safety concerns during robot-assisted eye surgeries are instrument tip position. Precise and safe positioning of the surgical instrument's tip on the retina is required to automate vitreoretinal tasks. Any inadvertent contact between the instrument tip and retinal tissue can result in devastating and permanent eye injury. This safety concern is further exacerbated when considering the fact that ophthalmic surgical tools are small gauge, flexible and they experience large deflections during the surgery [97]. Poor depth perception through stereoscopic camera also makes the situating worse. Different approaches in the literature have been adopted in order to localize the instrument tip and to estimate the distance between the tool tip and retina. Vision-based soft and hard virtual fixtures generated using the surgical microscope were generated in order to improve needle tip targeting [98]. Deep learning has also been utilized to provide an automatic tool localization using a stereo microscope [99]. However, The confined size of the workspace, small parallax in stereo microscopes, and the optical aberrations caused by the vitreous body creates unfavorable conditions for regular image processing algorithms [78]. To address such problems, OCT images have also been used for 3D needle tip localization in robot-assisted ophthalmic surgery [100–103]. Filtering techniques have also been employed. Using a state-estimating Kalman filter (KF) a feed-forward control strategy is proposed to suppress the tremor and to provide more accurate tool tip positioning [104]. Instrument's shadow was used to estimate the proximity between the instrument's tip and the retina during instrument positioning [78, 105, 106].

1.5 Thesis Overview

In order to enable the robots to be more actively and safely involved during ophthalmic surgical procedures, this dissertation reports the development of novel control and surgical state estimation algorithms to enhance safety during robot-assisted eye surgery. Surgical instruments, which are collaboratively moved by the robots, are in contact with the eye tissue from two main locations: 1) tool shaft at sclerotomy 2) tool tip with the target tissue. This dissertation describes incorporating control methods into the SHER to keep the forces at the scelrotomy (sclera forces) in safe ranges during robotic eye manipulations. In addition, state estimations methods are developed to improve the the tool tip position estimation when the tool shaft undergoes deflections. The ultimate outcome will be a robot equipped with advanced control and state estimations methods, which in turn enables safer interactions with patients and opens the way toward more advanced autonomous or semi-autonomous treatments. This dissertation contains the following main contributions where each of them constitutes a chapter of the thesis:

1) Adaptive sclera force and insertion depth control: Autonomous algorithms to control sclera forces and instrument insertion depth are integrated to the SHER. The control methods enable a velocity-controlled robot to keep the sclera forces and insertion depth within safe pre-defined boundaries while allowing surgeons to continue performing the relevant surgical maneuvers. To integrate the control methods to the robot, a customized FBG-equipped instrument providing online measurements of sclera forces and insertion depth is built and attached to the robot. Extensive preliminary experiments as well as clinician evaluations in actual operating rooms during robot-assisted eye manipulation have demonstrated the effectiveness of the methods in different surgical situations.

2) State estimation and filtering for instrument tip position and instrument insertion: In an attempt to improve the robot sensing capabilities, discrete time-varying state space models are obtained for the evolution of the 3D position of the instrument tip and instrument insertion depth inside of the eye. The state space equations are based on the robot forward kinematics model as well as the FBG-based online measurements for insertion depth and sclera forces. The sclera force measurements are transformed to quantities for instrument deflection using beam theory. Kalman Filtering (KF) algorithm is then implemented on the state space model to exploit the available information from the forward kinematics and FBG sensor measurements leading to improved estimations of instrument insertion depth and instrument tip position. More accurate measurements of the surgical states and conditions can potentially result in the development of more involved control methods, which substantially contributes toward a safer surgery with broader applications.

3) Calibration- and registration-independent tool tip position estimation: The force-based method, which utilizes state space models and KF to improve the tool tip position estimation, requires a pre-operative calibration to identify the stiffness (force-deflection relationship) of the instrument using offline data. In order to remove the dependency to any pre-operative calibration, which is time-consuming and is prone to errors, intra-operative online system identification methods are applied (calibration-independent). These methods use the visual feedback from the surgical microscope to monitor the tool tip and to attain an estimate of the instrument stiffness during the surgery. This theory is further formulated to make the entire framework independent of any requirement to know the frame transformation between the microscope and the robot coordinate frames (registration-independent).

Chapter 2

Adaptive Sclera Force and Insertion Depth Control during Robotic Ophthalmic Surgery

2.1 Background and Motivation

Surgical tasks inside of the eye encompass manipulating very delicate tissues and micron scale structures typically using instruments passing through an incision point in the sclera. The procedures in such surgeries are sometimes beyond human motor capabilities [1]. The root mean squared (RMS) value for an ophthalmic surgeon hand tremor is $182\ \mu m$ as measured by [36] which is comparable to the entire diameter of the involved retinal and choroidal vessels (i.e., between $50 - 150\ \mu m$ [37]). Furthermore, a healthy human retina has an average thickness of $212\ \mu m$ at the center of the fovea [107] which makes the precise targeting of freehand sub-retinal injections inconsistent and potentially unsafe, when the amplitude of hand tremor is considered.

In order to overcome these physiological human constraints and to perform very delicate procedures, advanced robotic platforms have been engineered to suppress tremor and enhance targeting accuracy of the instrument that will function inside of a very small and fragile eyeball. Various types of robotic systems have been designed and developed for eye surgery including collaborative robots in which surgeon and robot share the control of the surgical tool (e.g. [45,108]), tele-manipulated robots (e.g. [48,109]) and hand-held robotic devices (e.g. [110]). For instance, the Steady-Hand Eye Robot (SHER), as shown in Fig. 2.1, is an example of a collaborative robot that was fabricated at the Johns Hopkins University [54].

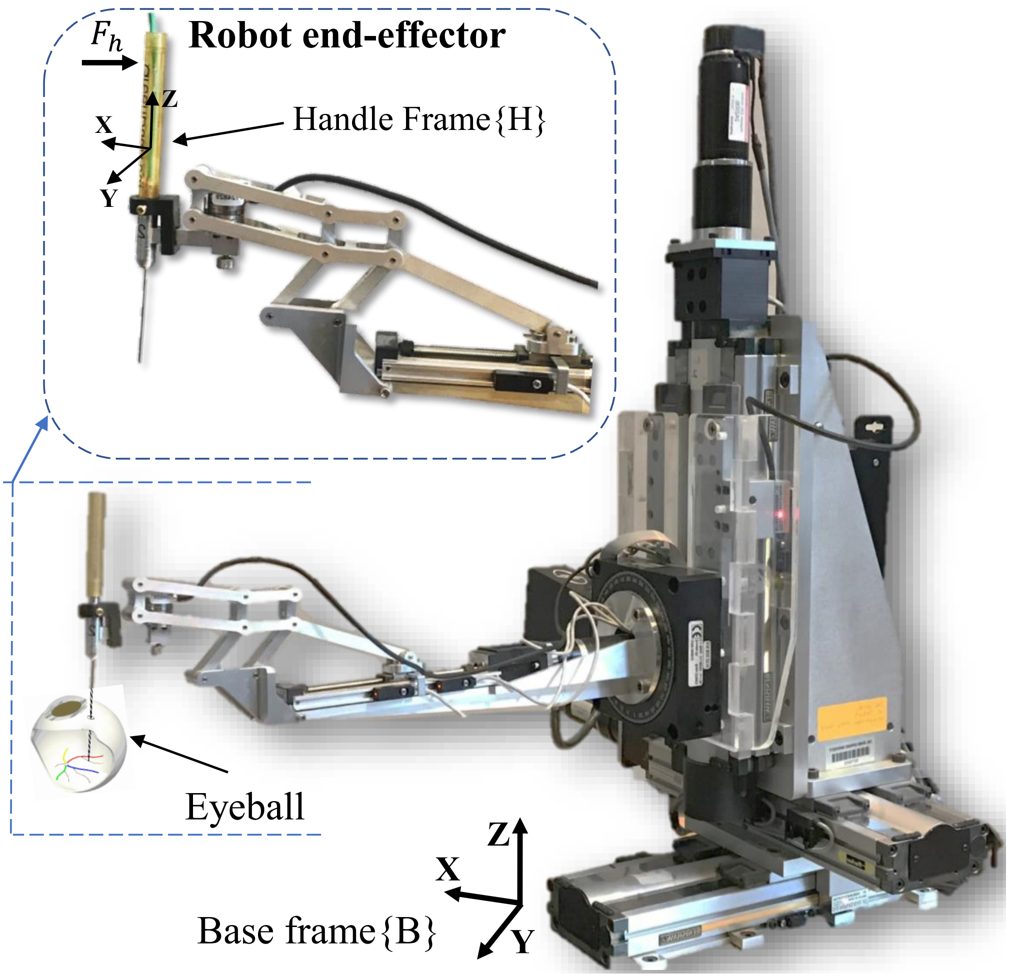

Figure 2.1: SHER and its five degrees of freedom. The first three axis indicate the translation motion and the last two axis represent the rotational motions around the associated axis. The handle frame is shown in the close-up view of the robot end-effector.

A review of the literature indicates that the focus of the above-mentioned robots have been mostly on hardware development (mainly for providing a tremor-free manipulation) while less attention has been paid to sensing and control, which are required for a reliable and safe robotic assist. In order for robots to meet the safety requirements for human use, advanced sensing ca-

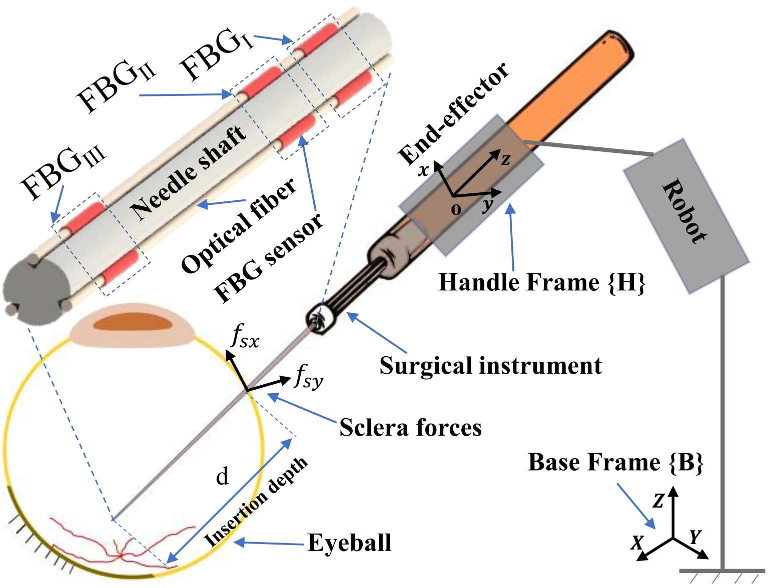

Figure 2.2: Schematic of the surgical tool attached to the robot. The base and handle frames are attached to the robot base and to the robot end-effector, respectively. Sclera forces and the instrument insertion depth are represented.

pabilities and control algorithms should be developed and implemented. This becomes even more necessary in eye surgery since the robot manipulates highly delicate and ultra-fine tissue. Robots in ophthalmic surgical procedures should not only provide high precision for the tool tip and cancel the tremor but also appropriately control the sclera forces f_{sx} and f_{sy} (components of the sclera forces along the x and y directions of the handle frame $\{H\}$ shown in Fig. 2.2) to enforce safety boundaries as well as the tool insertion depth d to avoid collision with retina (shown in Fig. 2.2).

Although major advances in instrument tip precision and safety have been made [43, 44, 83, 88, 90, 98, 102, 103, 111, 112], less attention has been paid to the relationship between the sclera and the tool shaft as well as instrument insertion safety. During freehand surgery, surgeons perceive the scleral forces and rely on them to guide both the eye movements and the instrument inside of the eye. However, the integration of robotics into ophthalmic microsurgery leads to a reduction in surgeon perception of tool-to-tissue interaction forces. Tool shaft-to-sclera, and tool tip-to-surgical target, forces are rendered either markedly reduced or imperceptible to the surgeon. This blunting of human tactile sensory input is due to the inflexible mass and large inertia of the robotic arm as compared to the milli-Newton scale of the interaction forces encountered during ophthalmic surgery. The loss of human tactile feedback, as well as the comparatively high forces that are potentially imparted to the fragile tissues of the eye, identify a potential iatrogenic risk during robotic eye surgery. Furthermore, as surgeons are working through a microscope which visualizes eyeball interior, there is no visual feedback from the tool-scleral interactions in robot-assisted surgery. It is still possible for a surgeon to unknowingly apply large sclera forces during a robot-assisted manipulation. Using robots in such procedures, may increase the risk of high force to sclera events [96]. Such inadvertent force applications may impact the retinal tasks being performed or directly injure the scleral wall.

One common approach to address this issue is the use of remote center of motion (RCM) mechanisms [48, 51]. However, the problem with RCM mechanisms is that they passively maintain the sclera forces in a prescribed safe range. Moreover, surgeons usually use a second instrument (e.g. a light pipe) during intraocular surgery and the forces resulting from the second tool increase sclera forces on the primary instrument (attached to the robot), even if RCM is present. In order to actively limit scleral forces during surgical maneuvers, He et al. [113, 114] have used a deep learning approach to predict unsafe sclera forces, and to counter them proactively to insure safety. The limitations of this method, however, include but are not limited to the large data sets required for training, and the occurrence of unreliable predictions due to network errors for untrained tool-retina interactions. Recently, the provision of auditory or haptic feedback based on sclera force has been proved to help surgeons keep those forces in safe ranges [115]. Auditory substitution or haptic feedback that has been deployed in the previous studies may have some disadvantages. First, the efficacy of feedback is highly dependent on the surgeon's reaction to it. In cases where effective action was barely executable by the subjects or when unexpected eye motion occurred, scleral forces could increase beyond safe limits [115]. Furthermore, it is now feasible to build in similar haptic and audio feedback based on tool insertion depth to enhance tool depth safety (if exceeded tool tip to retina collision occurs). However, having various types of audio and haptic feedback coming from different sources may have adverse effects on surgeon concentration during highly delicate, prolonged and intensely focused eye surgery tasks. For these and other reasons, it is potentially beneficial to control the robot such that it acts autonomously in a proper and safe way when sclera force or tool insertion depths exceed established safe boundaries.

Considering the mentioned limitations, this chapter describes the development of robotic autonomous sclera force ans insertion depth control methods. The control methods enable to robot to autonomously keep the sclera forces and insertion depth in safe prescribed ranges. This is done by integrating customized instruments to the SHER, which are able to measure sclera forces and instrument insertion in real-time.

2.2 Contribution

This chapter reports the integration of a control method to the SHER high-level control diagram such that the robot will be able to autonomously control the sclera forces and insertion depth and keep them in safe ranges. Because the SHER is a velocity-controlled robot a relation between the velocity commands and sclera force variations is required to develop such control algorithms. Because those relations are missing (unknown sclera tissue behaviour), an adaptive control method in which this relation is learned during the surgery is immensely beneficial.

For this reason, in this chapter a 1-D adaptive control method is customized for simultaneous 3-D control of sclera force and insertion depth. When the adaptive control is triggered, the robot produces translational motions along the relevant axes to correct the sclera force and/or insertion depth consistent with desired and safe trajectories. This control system is then implemented on the SHER. The adaptive control method has other useful applications in eye surgery including: control of the insertion depth when unexpected motion of the patient's head is observed or holding a light pipe in a fixed and safe position by the robot. To the best of our knowledge, adaptive control for applications in robot-assisted eye surgery has not been used before.

After several preliminary studies on the control methods, we have chosen two variants of the adaptive sclera force control method for a comprehensive evaluation with clinicians. In brief, ten ophthalmology clinicians were enrolled in robot-assisted user studies conducted in an operating room in Wilmer Eye Institute at the Johns Hopkins Hospital. The users were tasked to follow retinal vessels with a tool tip on a phantom eyeball. A piezo-actuated linear stage was utilized to simulate random motions of patient head which might occur when the patient is under anesthesia. Finally, the performance of each control method was analyzed and compared directly to the same clinician's freehand manipulations (unassisted by the algorithm or robot).

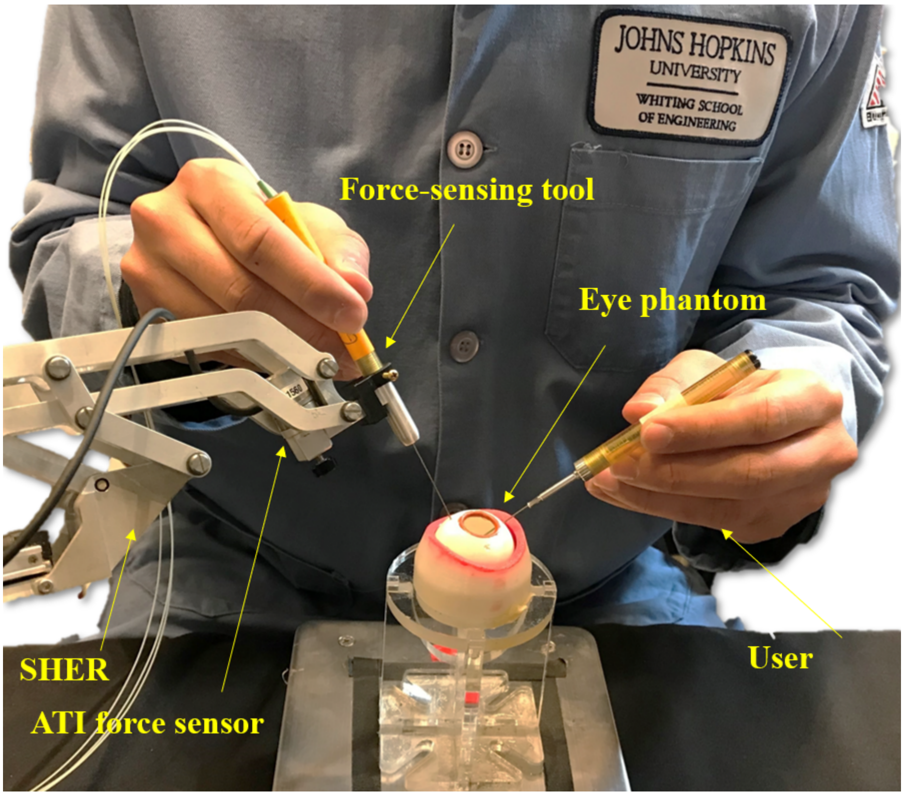

Figure 2.3: Eye phantom manipulation with the SHER– the user is grabbing the instrument which is attached to the robot in the right hand and the secondary tool in the left hand to manipulate the eye phantom.

2.3 Robot Control Framework

The SHER is a 5-degree-of-freedom (DoF) robot which provides a steady-hand manipulation for users. Various surgical tools can be attached to the robot end-effector using a quick release mechanism. The robot enables users to perform tremor-free surgical maneuvers. The users and the robot both hold the surgical instrument handle and move it collaboratively to achieve surgical goals (Fig. 2.3).

In order to describe the robot motion, two coordinate frames are incorporated into the robot: the base coordinate frame $\{B\}$ which is fixed to the robot base and the handle coordinate frame $\{H\}$ which is attached to the robot end-effector (Figs. 2.1). The rigid body transformation between $\{B\}$ and $\{H\}$ can be written as $\mathbf{F}_{bh}(q) \in SE(3)$ as a function of joint angles $q \in \mathbb{R}^5$.

$$\mathbf{F}_{bh}(q) = \begin{pmatrix} \mathbf{R}_{bh}(q) & S_{bh}(q) \\ \mathbf{0}_{1\times 3} & 1 \end{pmatrix} \tag{2.1}$$

In (2.1), the terms $\mathbf{R}_{bh}(q) \in SO(3)$ and $S_{sb}(q) \in \mathbb{R}^3$ are the rotation and translation parts of $\mathbf{F}_{bh}(q)$, respectively. Using the product of exponential formula developed in [116], $\mathbf{F}_{bh}(q)$ can be written as follows:

$$\mathbf{F}_{bh}(q) = e^{\hat{\xi}_1 q_1} ... e^{\hat{\xi}_5 q_5} g_{sb}(0) \tag{2.2}$$

where $q_i,\ i = 1, ..., 5$ is the ith element of the vector of joint angles q. $\mathbf{F}_{bh}(0)$ indicates the initial relative configuration of frames $\{B\}$ and $\{H\}$ when $q = \mathbf{0}_{5\times 1}$. Each $\xi_i = (v_i, w_i)^T$, where $(v_i)^T$ and $(w_i)^T$ are both in $\mathbb{R}^3$, is a twist coordinate representing the rigid body transformation associated with ith joint motion of the robot. For the prismatic joints of the robot (first three joints) w_i is zero vector and v_i is a unit vector along the prismatic joint direction written in frame $\{H\}$. For the revolute joints of the robot w_i is the unit vector of rotation axis of the joint and v_i is $-w_i \times q_i$ where q_i is an arbitrary point on rotation axis [116]. Then, the 4×4 matrices $\hat{\xi}_i$ for each robot joint in (2.2) can be constructed as follows:

$$\hat{\xi}_i = \begin{bmatrix} \hat{w}_i & v_i \\ 0_{3\times 1} & 0 \end{bmatrix} \tag{2.3}$$

where $\hat{w}_i$ is a 3×3 skew symmetric matrix constructed by w_i. Then, defining the body velocity of the of the frame $\{H\}$ as $V^h = \mathbf{F}_{bh}^{-1}\dot{\mathbf{F}}_{bh}$, this velocity can be written in twist coordinates as written in (2.4) using the body Jacobian $\mathbf{J}_{bh}^h$ formula.

$$V^h = \mathbf{J}_{bh}^h(q)\dot{q} \tag{2.4}$$

where $\mathbf{J}_{bh}^h$ is defined as follows.

$$\mathbf{J}_{bh}^h = \begin{bmatrix} \xi_1^\dagger & \dots & \xi_5^\dagger \end{bmatrix} \tag{2.5}$$

$$\xi_i^\dagger = Ad^{-1}_{e^{\hat{\xi}_i\theta_i}\dots e^{\hat{\xi}_5\theta_5}g_{SB}(0)}\xi_i$$

In (2.4), $V^h = (v^h, w^h)^T$ is a vector in $\mathbb{R}^6$ representing the body velocity of frame $\{H\}$ written in twist coordinates. The terms $v^h \in \mathbb{R}^{1\times 3}$ and $w^h \in \mathbb{R}^{1\times 3}$ indicate the velocity of the origin of frame $\{H\}$ and the angular velocity of the frame $\{H\}$ both expressed in the frame $\{H\}$, respectively. In (2.5), Ad is the 6×6 adjoint transformation depending on the configuration of the robot [116]. The adjoint transformation for a general rigid body transformation F with rotational and translational components R and S is as follows:

$$Ad_{\mathbf{F}} = \begin{pmatrix} \mathbf{R} & \hat{S}\mathbf{R} \\ 0_{3\times 3} & \mathbf{R} \end{pmatrix} \tag{2.6}$$

A three-level hierarchy forms the control framework of the robot: 1) High-level admittance controller controller 2) Mid-level optimizer 3) Low-level joint velocity controller which are explained as follows.

2.3.1 High-level Admittance Controller

The high-level controller outputs the desired body velocity, $V^h_{des} = (v^h_{des}, w^h_{des})^T$, of the frame $\{H\}$ in twist coordinates. The cooperative admittance control sets V^h_{des} proportional to the generalized wrench $F^h_h = (f^h, \tau^h)^T$ at the origin of the frame $\{H\}$ which is written in (2.7). The term $f^b \in \mathbb{R}^{1\times 3}$ and $\tau^b \in \mathbb{R}^{1\times 3}$ are the force and torques applied by the user hand to the surgical instrument handle after being transferred to the frame $\{H\}$. The superscript h indicates that the wrench is expressed in frame $\{H\}$.

$$V^h_{des} = \mathbf{D}F^h_h \tag{2.7}$$

In (2.7), D is a 6×6 diagonal matrix with elements $d_i,\ i = 1, ..., 6$ on the diagonal. This proportional assignment of desired velocity V^h_{des} to the wrench

F_h^h creates an intuitive motion of the robot end-effector and the user can easily move the instrument to target position by exerting a proper wrench F_h to the tool handle.

2.3.2 Mid-level Optimizer and Low-Level Controller

After finding the desired rigid body velocity $V_{des}^h \in \mathbb{R}^6$ of $\mathbf{F}_{bh}$ in the frame $\{H\}$, we need to first express this vector in the base coordinate frame. This is done using the adjoint transformation which is given in (2.8):

$$Ad_{\mathbf{F}_{bh}} = \begin{pmatrix} \mathbf{R}_{bh} & \hat{S}_{bh}\mathbf{R}_{bh} \\ 0_{3\times 3} & \mathbf{R}_{bh} \end{pmatrix} \tag{2.8}$$

Now the desired rigid body velocity of $\mathbf{F}_{bh}$ in the base frame $\{B\}$ can be computed as follows:

$$V_{des}^b = Ad_{\mathbf{F}_{bh}} V_{des}^h \tag{2.9}$$

Because the robot is a 5-DoF robot and V_{des}^b is in $\mathbb{R}^6$, desired velocity V_{des}^b cannot be exactly achieved. Instead, the following optimization is solved to find the optimized joint velocities ($\dot{q} \in \mathbb{R}^5$) of the robot:

$$\dot{q}_{des} = \min_{\dot{q}} \; |\mathbf{J}^b_{bh}\dot{q} - V^b_{des}| \tag{2.10}$$

with the inequality constraints of:

$$\dot{q}_L \leq \dot{q} \leq \dot{q}_U \;\; \text{and} \;\; q_L \leq q \leq q_U \tag{2.11}$$

In (2.11) the the terms $\dot{q}_L \in \mathbb{R}^5$ and $\dot{q}_U \in \mathbb{R}^5$ are the joint velocity limits and $q_L \in \mathbb{R}^5$ and $q_U \in \mathbb{R}^5$ are the bounds for joint angles. The joint position bounds are implemented using the limit switches and are not included in the mid-level optimizer procedure. The term $\mathbf{J}^b_{bh}$ in (2.10) is the spatial Jacobian and is related to body Jacobian $\mathbf{J}^h_{bh}$ defined in (2.4) using (2.12):

$$\mathbf{J}^b_{bh} = Ad_{\mathbf{F}_{bh}} \mathbf{J}^h_{bh} \tag{2.12}$$

After solving the optimization (2.10), $\dot{q}_{des}$ is sent to the low-level embedded robot motor controller (Galil 4088, Galil, 270 Technology Way, Rocklin, CA 95765) for joint velocities to be commanded to the actuators.

2.4 Sensorized Instrument

In order to measure sclera force components (f_{sx} and f_{sy}) and insertion depth (d) as shown in Fig. 2.2, a dual force-sensing instrument was used [117].

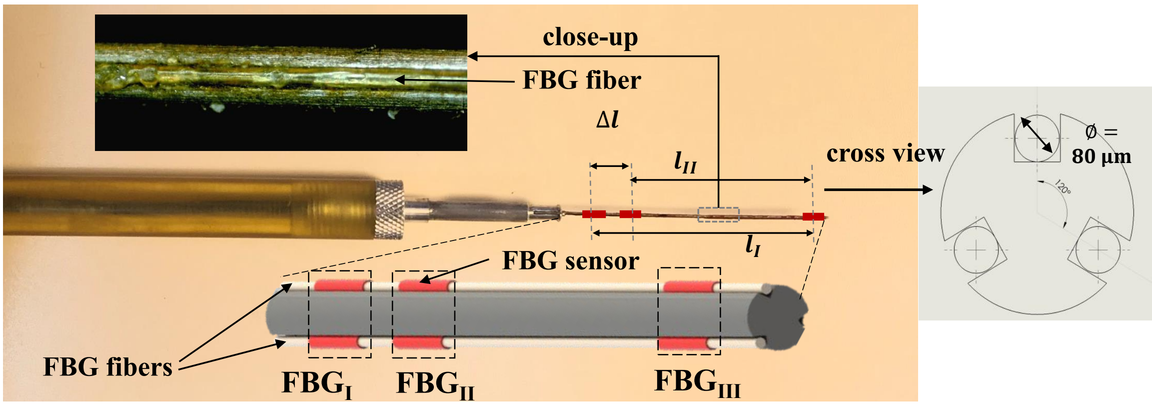

Figure 2.4: Force-sensing tool. The three FBG zones are marked with the short red lines. The lengths l_I and l_{II} indicate the distance from FBG_{I} and FBG_{II} to the tool tip. A close-up view of how the fibers are placed along the tool shaft and the related dimensions are also provided. The vector F_s shows the place where the sclera force is applied to the tool shaft.

The tool consists of three parts including the tool shaft (a stainless steel wire with diameter of 0.63 mm), the tool adapter, and the tool handle, which are shown in Fig. 2.4. In order to enable the tool to measure sclera forces and insertion depth, three optical fibers equipped with Fiber Bragg Grating (FBG) sensors (Technica S.A, Beijing, China) with diameter of 80 μm are placed in the v-shaped grooves along the tool shaft with a radial separation angle of $120°$ (Fig. 2.4). FBGs are very sensitive strain sensors capable of detecting strains less than 1 $\mu\epsilon$, based on the wavelength shifts of optical beams sent through the fibers. Furthermore, due to their light weight and bio-compatibility, FBGs are suitable for opthalmic surgery applications. As it can be seen in Fig. 2.4, each optical fiber contains three FBG active areas represented by the short red segments, summing up to 9 FBG sensors in total along the tool shaft. A calibration procedure is then conducted to obtain the calibration matrices $K_I \in \mathbb{R}^{2\times3}$ and $K_{II} \in \mathbb{R}^{2\times3}$, as instructed by [73]. These calibration matrices relate the moments $M_I \in \mathbb{R}^2$ and $M_{II} \in \mathbb{R}^2$—induced by the sclera force $F_s = [f_{sx} \quad f_{sy}]^T$ on the FBG sections I and II the FBG readings $\Delta S_I \in \mathbb{R}^3$ and $\Delta S_{II} \in \mathbb{R}^3$ (because there are 3 FBG sensors at each cross Section i, where $i = I$ and II), respectively. The sclera force can then be obtained as follows:

$$F_s = \frac{M_{II} - M_I}{\Delta l} = \frac{K_{II}\Delta S_{II} - K_I \Delta S_I}{\Delta l} \tag{2.13}$$

where Δl is the distance between the centers of FBG_I and FBG_{II}. After finding the sclera force components, the insertion depth can be found using either of equations in (2.14):

$$\mathbf{d} = l_{II} - \frac{||M_{II}||}{||F_s||} = l_I - \frac{||M_I||}{||F_s||} \tag{2.14}$$

where l_{II} and l_I are the distance between the tool tip and the FBG_{II} and FBG_I, respectively (Fig .2.4). It is noteworthy to mention that although FBG fibers are sensitive to temperature, the calibration procedure delineated in [73] makes the measurements robust against temperature variations.

As it can be observed in (2.14), the sclera force appears in the denominator. One drawback of this approach, therefore, is the insertion depth estimation instability when the sclera force is small and noisy. Additionally, when the tool shaft is not in contact with the sclera, no insertion depth measurement will be available. These are the present limitations associated with this method of measuring the insertion depth. Methods for improvement of insertion depth measurements are studied in chapter 3. Of note, using (2.13) and (2.14), the presented dual force sensing tool is able to measure sclera force components and insertion depth with an accuracy less than 1 mN and 0.5 mm, respectively [114].

2.5 Adaptive Control Methods

As it was mentioned in Section 2.2, due the unknown stiffness of the sclera tissue, which is a required parameter to control sclera forces using a velocity-controlled robot, an adaptive control method can be beneficial. The adaptive control method tries to intra-operatively learn the tissue stiffness along the x and y directions of the handle frame (λ_x and λ_y shown in Fig. 2.5) using adaptation laws.

The adaptive control method that is going to be used to control the sclera forces and insertion depth for the SHER builds upon the adaptive force control method developed by Roy et al. [118] for general 1-DoF velocity-controlled robots and extends it to the eye surgery domain. Considering Fig. 2.6, there are two basic assumptions for this method:

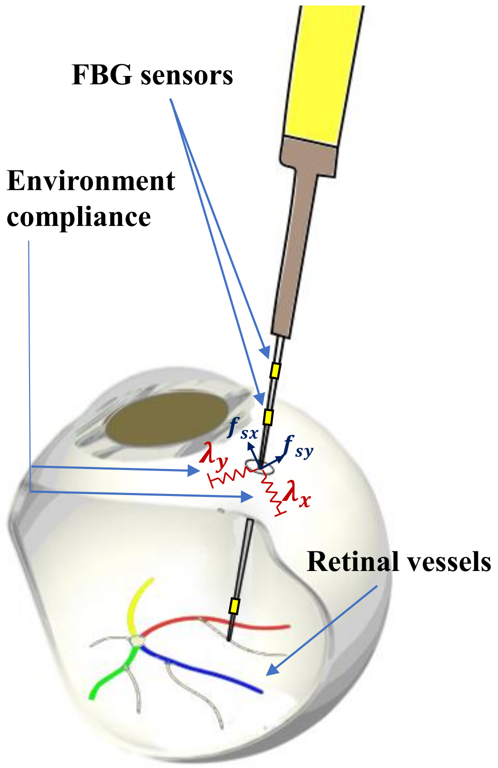

Figure 2.5: Close-up view of the schematic eyeball shows the sclera force components and the environment compliance λ_x and λ_y along the x and y directions of the handle frame. The colored phantom vessels are also visible in the eyeball.

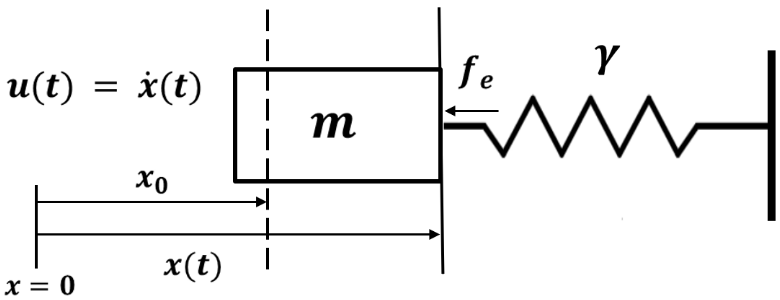

Figure 2.6: Schematic diagram for the adaptive force control of a 1-Dof velocity-controlled robot with mass m interacting with an environment with linear and unknown compliance γ.

1. The robot is in contact with an environment with unknown but linear stiffness/compliance (Fig. 2.6). In other words, the force displacement

model of the robot end-effector is assumed to conform to the linear equation of $f_e = \frac{1}{\gamma}(x - x_0)$ or $df_e = \frac{1}{\gamma}(dx)$ where f_e is the interaction force exerted to the robot by the flexible environment, γ is a constant representing the environment compliance, x is the position of the 1-DoF robot normal to the contact surface and x_0 is contact surface location at the equilibrium point.

2. The robot is a velocity-controlled robot, i.e. it has a built-in low-level velocity controller that makes the robot's actual velocity $\dot{x}$ track any bounded velocity setpoint $\dot{x}_d$.

The goal of the 1-D adaptive control is to design a control law which provides asymptotically exact outer loop force control by providing proper reference velocity trajectory $(\dot{x}_d)$ for the low-level velocity control. Consequently, the interaction force (f_e) would be able to track any desired reference force trajectory (f_d) which is C^2 bounded and has bounded derivatives, $\dot{f}_d$ and $\ddot{f}_d$. The control input and the adaptation law are provided in (2.15).

$$\begin{aligned} \dot{x}_d(t) &= \hat{\gamma}\dot{f}_d(t) - k_f \Delta f(t) \\ \dot{\hat{\gamma}} &= -\alpha \dot{f}_d(t) \Delta f(t) \end{aligned} \tag{2.15}$$

where the term $\Delta f \triangleq f_e - f_d$ is the force tracking error. The constants α and k_f are gains for adaptation law and the force tracking error, respectively. Since it was assumed that the compliance of the environment is unknown, an estimation of this parameter ($\hat{\gamma}$) is used in the control law above. The adaptation law defines the way $\hat{\gamma}$ changes over time. Using a Lyapunov function it is proved in [118] that the force tracking error Δf and the compliance estimation $\hat{\gamma}$ will remain bounded. Moreover, one can show that $\lim_{t\to\infty} \Delta f(t) = 0$ if the conditions given in (2.16) are satisfied [118].

$$\int |\Delta\dot{x}|^2 dx < \infty \quad and \quad \lim_{t\to\infty} \Delta\dot{x} = 0 \tag{2.16}$$

In (2.16), the term $\Delta\dot{x}$ is the velocity tracking error $\dot{x} - \dot{x}_d$ and based on the second assumption discussed earlier, it would converge to zero. Thus, based on (2.16) the adaptive control will make Δf go to zero.

2.5.1 Adaptive Sclera Force Control

The first assumption for the adaptive control in Section 2.5 states that the environmental force f_e should be linearly proportional to the position of the robot x in the coordinate frame where $\dot{x}_d(t)$ is going to be calculated (df_e, which is the differential of f_e should be proportional to dx, differential of x). Now assume that at each instant of robot motion we have an imaginary fixed frame $\{H'\}$ coincident with the handle frame $\{H\}$ (shown in Fig. 2.2). We assume that the infinitesimal variation of the sclera forces along the x and y directions of the handle frame $\{H\}$, df_{sx} and df_{sy}, are linearly proportional to the infinitesimal variation of the position of the frame $\{H\}$ origin along the x and y directions of $\{H'\}$, dx and dy. This assumption is realized because the tool shaft is like a cantilever beam, and therefore the infinitesimal variation of the force applied to the beam (which is now df_{sx} or df_{sy}) is proportional to the infinitesimal variation of the beam deflection (which is now dx and dy). Therefore. we can make use of the adaptive control law to produce desired velocities for the robot end-effector along the x or y axes of the handle frame ($V^h_{des}[1]$ or $V^h_{des}[2]$) such that f_{sx} and f_{sy} will follow desired trajectories f_{dx} and f_{dy}. Compared to (2.15), we are using either f_{sx} or f_{sy} to substitute f_e. As it was explained in (2.7), the velocity vector V^h_{des} is in $\mathbb{R}^6$. For the adaptive sclera force control, we are only modifying how the first two elements of V^h_{des} (namely $V^h_{des}[1]$ and $V^h_{des}[2]$, (where the 1 and 2 indices refer to the first and second elements of vector V^h_{des}) are generated such that the robot will be able to autonomously control the sclera forces. In other words, the robot will abide by the user's interaction forces for other elements of V^h_{des}. Thus, the users would not feel that the robot inhibits their manipulation. Based on (2.15), the equations for $V^h_{des}[1]$ and $V^h_{des}[2]$ will be as follows:

$$
\begin{aligned}
V^h_{des}[1] &= \hat{\lambda}_x \dot{f}_{dx} - k_x(f_{sx} - f_{dx}) \\
V^h_{des}[2] &= \hat{\lambda}_y \dot{f}_{dy} - k_y(f_{sy} - f_{dy})
\end{aligned}
\tag{2.17}
$$

where $\hat{\lambda}_x$ and $\hat{\lambda}_y$ are estimations for λ_x and λ_y (shown in Fig. 2.5). These estimations are updated using the following adaptations laws based on (2.15):

$$\begin{aligned}\dot{\hat{\lambda}}_x &= -\alpha_x \dot{f}_{dx}(f_{sx} - f_{dx}) \\ \dot{\hat{\lambda}}_y &= -\alpha_y \dot{f}_{dy}(f_{sy} - f_{dy})\end{aligned} \tag{2.18}$$

In (2.17) and (2.18) k_x, k_y, α_x, and α_y are constant gain values. The desired reference trajectories f_{dx} and f_{dy} in (2.17) and (2.18) should be defined in a way to ensure safe sclera force interactions. In other words, when the sclera interaction forces overstep a predefined threshold, the adaptive sclera force control should be triggered and the first two elements of V^h_{des} in (2.7) are generated according to (2.17) in order to make the sclera forces follow desired safe trajectories.

In the following we define two variations for triggering the adaptive sclera force control method including the adaptive component control (ACC) and the adaptive norm control (ANC).

- **Adaptive component control for sclera force (ACC)**

There are two sclera force components along the x and y directions of the handle frame $\{H\}$ (Fig. 2.2), respectively called f_{sx} and f_{sy}. The ACC method considers each component of sclera force independently. If the ith ($i = x$ or y) component exceeds the safe level U, the ACC$_i$ method reduces the f_{si} ($i = x$ or y)

based on a desired safe reference trajectory for sclera force f_{di} ($i = x$ or y). For the ACC control, the vector V^h_{des} is generated based on (2.19) as follows:

$$
\begin{aligned}
V^h_{des} = &\begin{bmatrix} (1-\delta_x)d_1 & 0 & \mathbf{0}_{2\times4} \\ 0 & (1-\delta_y)d_2 & \\ \mathbf{0}_{4\times2} & & diag(d_3, d_4, d_5, d_6) \end{bmatrix} F^h_h \\
&+ \begin{bmatrix} diag(\delta_x, \delta_y) & \mathbf{0}_{2\times4} \\ \mathbf{0}_{4\times2} & \mathbf{0}_{4\times4} \end{bmatrix} \begin{bmatrix} \hat{\lambda}_x \dot{f}_{dx} - k_x(f_{sx} - f_{dx}) \\ \hat{\lambda}_y \dot{f}_{dy} - k_y(f_{sy} - f_{dy}) \\ \mathbf{0_{4\times1}} \end{bmatrix}
\end{aligned}
\tag{2.19}
$$

The variable δ_i ($i = x$ or y) in (2.19) has a binary value (0 or 1). $\delta_i = 1$ indicates that ACC$_i$ is activated and if it is zero the ACC$_i$ is deactivated. As noted from (2.19), if δ_i is zero (meaning ACC$_i$ is deactivated) then the corresponding component of V^h_{des} for the axis i will be simply produced based on the cooperative admittance control law (2.7). The desired reference trajectories for f_{sx} is written in (2.20) which is a exponentially decreasing function of time.

$$
f_{dx} = \frac{U sgn(F_{sx})}{2}(e^{-(t-t_x)} + 1) \tag{2.20}
$$

For f_{sy} a similar scenario can be imagined.

Algorithm 1: ACC control method

```
Input: Sclera force components f_si, i = x,y.
Output: Acc_i activation, i = x,y.
initialization of λ̂_i, i = x,y;
if |f_si| > U then
    t_i = current time;
    δ_i = 1; (ACC_i triggered)
    while |F_sx| > 0.75U do
        δ_i = 1; (Keep ACC_i activated)
        Generate f_di based on (2.20);
    end
    δ_i = 0; (Switch to cooperative control for axis i);
end
```

$$f_{dy} = \frac{Usgn(f_{sy})}{2}(e^{-(t-t_y)} + 1) \tag{2.21}$$

In (2.20) and (2.21), t_x and t_y are the time when f_{sx} or f_{sy} exceeds the safe levels, respectively. The logic for activating and deactivating the ACC$_i$ is written in Algorithm 1. The adaptive sclera force control is sustained independently for each component f_{sx} and f_{sy} until they are reduced to 0.75 of their value at $t = t_i$ $i = x, y$. The reference functions used in (2.20) and (2.21) are descending exponential functions that reduce the norm of the corresponding component of sclera force. Also the reference functions maintain the continuity of the force signal. For instance, at $t = t_x$ the desired force f_{dx} based on (2.20) is equal to $Usgn(f_{sx})$, which is the value of f_{sx} when it exceeds the upper bound U.

It is noted that the descending reference trajectories used in 2.20 and 2.21

are found with trial and error and are not necessarily the best trajectories. Any other differentiable descending function can also be used.

- **Adaptive norm control for sclera force (ANC)**

The alternative to the ACC method controlling each component of sclera force independently, is the ANC algorithm in which both components of sclera force are reduced simultaneously. The control is activated when the 2-norm of sclera force vector ($||F_s|| = \sqrt{f_{sx}^2 + f_{sy}^2}$) reaches the limit U. The control law will then obey (2.22).

$$
\begin{aligned}
V_{des}^h = & \begin{bmatrix} (1-\delta)d_1 & 0 & \mathbf{0}_{2\times4} \\ 0 & (1-\delta)d_2 & \\ \mathbf{0}_{4\times2} & & diag(d_3, d_4, d_5, d_6) \end{bmatrix} F_h^h \\
& + \begin{bmatrix} diag(\delta, \delta) & \mathbf{0}_{2\times4} \\ \mathbf{0}_{4\times2} & \mathbf{0}_{4\times4} \end{bmatrix} \begin{bmatrix} \hat{\lambda}_x \dot{f}_{dx} - k_x(f_{sx} - f_{dx}) \\ \hat{\lambda}_y \dot{f}_{dy} - k_y(f_{sy} - f_{dy}) \\ \mathbf{0}_{4\times1} \end{bmatrix}
\end{aligned}
\tag{2.22}
$$

In (2.22) δ which has a binary value is the activation indicator for ANC method. If $\delta = 1$ it means that the ANC method is activated and if $\delta = 0$ (indicating the deactivation of ANC method) then (2.22) will be identical to (2.7). Theoretically, the ANC method is more restrictive than the ACC control method as it reduces both components together and it provides less freedom for users, but the benefit should be higher effort with regard to maintaining scleral forces into prescribed safe ranges. The desired reference trajectories for the ANC method which are decreasing exponential functions, are written in (2.23).

$$
\begin{aligned}
f_{dx} &= \frac{f_{sx}^0}{2}(e^{-(t-t_0)}+1) \\
f_{dy} &= \frac{f_{sy}^0}{2}(e^{-(t-t_0)}+1)
\end{aligned}
\tag{2.23}
$$

In (2.23), t_0 is the time when the magnitude of sclera force F_s exceeds the safe level U. The terms f_{sx}^0 and f_{sy}^0 are the values of f_{sx} and f_{sy} at $t = t_0$, respectively. The activation algorithm for the ANC method is provided in Algorithm 2.

Algorithm 2: ANC control method

Input: Sclera force components $f_{si},$ i = x,y.
Output: ANC activation,
initialization of $\hat{\lambda}_i,$ i = x,y;
if $||F_s|| > U$ **then**
  t_0 = current time;
  $\delta = 1$; (ACC$_i$ triggered)
  f_{sx}^0 = current f_{sx};
  f_{sy}^0 = current f_{sy};
  while *(*$|f_{sx}| > 0.75||f_{sx}^0||$ *or* $|f_{sy}| > 0.75|f_{sy}^0|$*)* **do**
    $\delta = 1$; (Keep ANC activated)
    Generate f_{dx} and f_{dy} based on (2.23);
  end
  $\delta = 0$; (Switch to cooperative control for axis i);
end

The adaptive sclera force control is sustained for both components f_{sx} and f_{sy} until both components are reduced to 0.75 of their value at $t = t_0$.

2.5.2 Adaptive Insertion Depth Control

In this application we will customize the adaptive control algorithm to control the insertion depth of the surgical tool by replacing the term f_e in (2.15) with the insertion depth d. In other words, any variable whose infinitesimal variation satisfies the first assumption in Section 2.5 can be used instead of f_e. Following the same explanation provided in Section 2.5.1, at each instant the infinitesimal variation of insertion depth d is proportional to the infinitesimal variation of the RCM point position along the z axis of the frame $\{H'\}$. Thus, we can produce desired velocities for the end-effector along the z axis of the handle frame such that now the insertion depth will track a desired and safe reference trajectory. The control can be triggered whenever the insertion depth exceeds certain limits which may lead to collision between the tool tip and the retina. The control law and the adaptation law for the insertion depth control are provided in (2.24):

$$\begin{aligned} V^h_{des}[3] &= \hat{\lambda}_z \dot{d}_d(t) - k_z \Delta d(t), \\ \dot{\hat{\lambda}}_z &= -\alpha_z \dot{d}_d(t) \Delta d(t), \end{aligned} \tag{2.24}$$

where $\Delta d = d(t) - d_d(t)$ is the insertion depth tracking error. α_z and k_z are constant gain values. The term d_d denotes the desired trajectory for d and $\dot{d}_d$ is the derivative of d_d. Similar to the sclera force control Section 2.5.1, a decreasing exponential desired trajectory is assumed for insertion depth. As

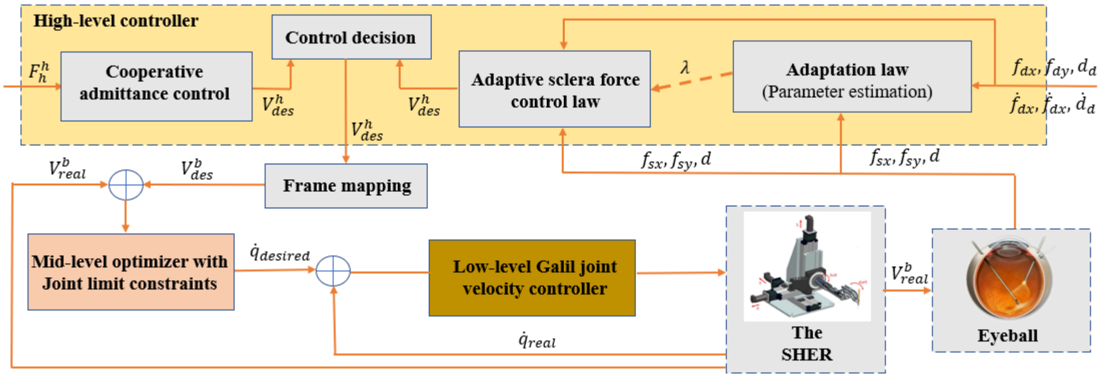

Figure 2.7: Block diagram for the closed-loop control system of the SHER. It shows the high-level (all controllers in the upper part, which is highlighted in yellow) controller, the mid-level optimizer and the low-level joint velocity controller.

soon as this control mode is activated the robot will autonomously reduce the insertion depth to safe ranges based on the following desired trajectory:

$$d_d(t) = \frac{U_d}{2}(e^{-2(t-t_z)} + 1) \tag{2.25}$$

where t_z is the time when the insertion depth exceeds the safe limit of U_d. At any necessary time any of the first three elements of the V_{des}^h can be switched to the adaptive control methods while other elements continue to be generated based on the general cooperative admittance control (2.7). Of note, the descending reference trajectory used in 2.25 is found with trial and error and is not necessarily the best trajectory. Any other differentiable descending function can also be used instead. It is noteworthy to say that the adaptive control methods will be placed in high-level controller methods of the SHER next to the admittance control method, which was described in Section 2.3.1. A block diagram showing the whole control framework of the SHER is depicted in Fig. 4.2. The high-level controller (highlighted in yellow in Fig. 4.2) consists of two modes including the cooperative admittance control and the adaptive sclera force control.

2.6 Validation

Several experiments and user studies were conducted to evaluate the control methods discussed in this chapter and to compare the safety-enhanced SHER system to freehand mock ophthalmic surgeries. In all of the conducted experiments, an eye phantom made from Silicon was used to model simple surgical tasks in eye surgery, which is shown in Fig. 2.8. The phantom was placed into a 3D-printed socket. To produce a realistic eye ball motion, the interface between the eye phantom and the eye socket was lubricated with mineral oil. Moreover, painted vessels were attached inside the eye ball on the posterior part as mock retinal vessels, Fig. 2.8. It is also noteworthy to say that for all of the adaptive sclera force implementation the constant parameters k_x and k_y in (2.17) were set to 0.2 and α_x and α_y in (2.18) were set to 5×10^{-5}. For adaptive insertion depth control method the constant parameter k_z and α_z in (2.24) were set to 10 and 10^{-4}, respectively. These values were obtained with trial and error.

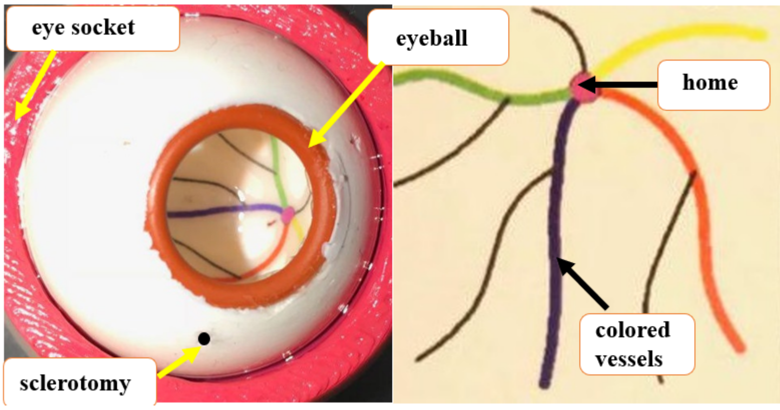

Figure 2.8: Close-up view of the eye phantom and the painted vessels on the retina.

In the following section, the preliminary experiments conduced in an engineering lab environment for evaluating the adaptive control methods are explained and the associated results are provided. Next, we will explain how further assessment of the adaptive sclera force control methods has been carried out during multi-user experiments with clinicians in an actual surgical room environment. The results for the multi-user study is provided in Section 2.6.2.

2.6.1 Preliminary Experiments

The experimental setup shown in Fig. 2.9 was used to conduct the preliminary experiments to evaluate the adaptive sclera force and insertion depth control methods. In the experimental setup the SHER was used as the robotic platform to perform eyeball manipulation. An FBG-equipped force-sensing tool

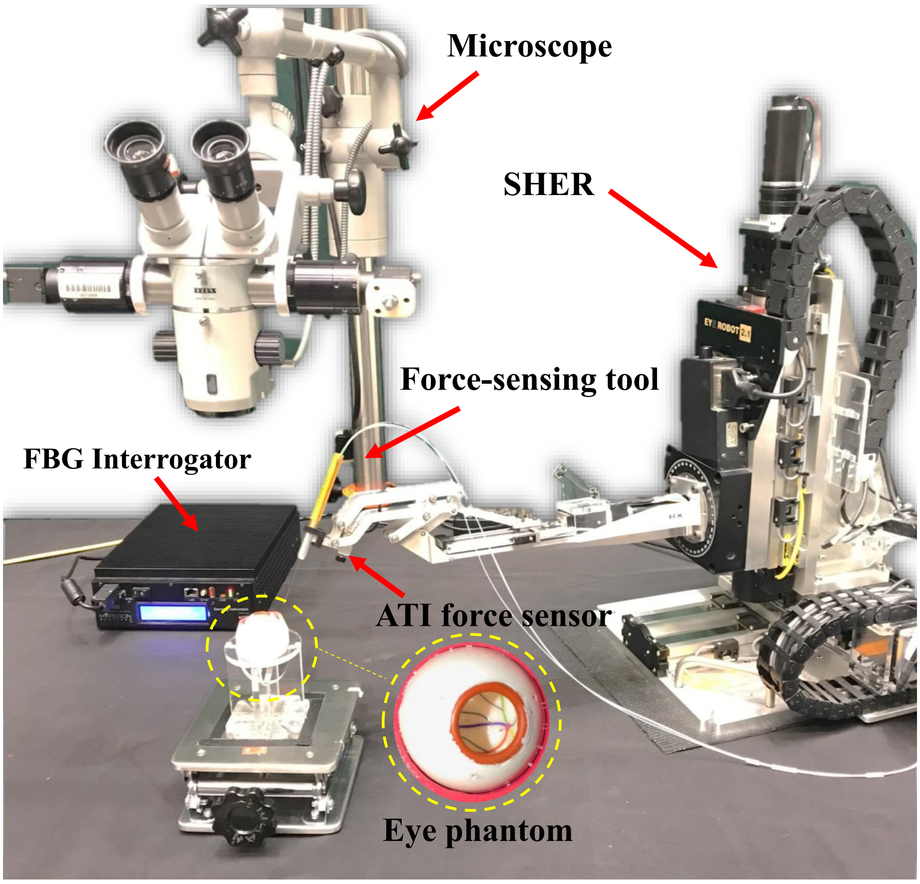

Figure 2.9: Experimental setup for conducting the preliminary experiments including the SHER, the FBG-equipped force-sensing tool, the FBG interrogator, the eye phantom, and the microscope.

was calibrated and attached to the robot to measure online sclera forces and insertion depth (as explained in Section 2.5). The FBG optical fibers were connected to an FBG interrogator (si155-Hyperion from Micron Optics Inc., Atlanta, GA) reading the FBG data in 1 kH. A Zeiss microscope provided direct visualization of the eye phantom and was placed on top of the eyeball. The user's force and torques applied to the handle F_h^h was measured by the 6-DoF ATI force/torque sensor attached under the robot wrist. The measurements for sclera forces, handle force and torque components and the time information were recorded using the software package for the SHER control developed using the C++ CISST-SAW libraries [119].

2.6.1.1 Results and Discussion for Preliminary Experiments

First, to show the performance and functionality of the adaptive force control that the controller can actually follow the desired trajectories for f_{sx} and f_{sy}, a sinus wave of $40\sin(2t)$ mN and $-40\sin(2t)$ mN were set for the f_{dx} and f_{dy}, respectively. Thus, the first two elements of V^h_{des} were produced based on the adaptive control and the remaining four elements of V^h_{des} were set to zero. In this experiment a single instrument was attached to the robot and inserted into the eyeball, without a user holding it. The results for this implementation are shown in Fig. 2.10.

Secondly, the ACC force control was utilized to maintain the sclera force within the safe bounds. Based on the data recorded from the behavior of an expert surgeon, an upper bound of 120 mN for sclera force was assigned as the safe limit [115]. We have kept this value as the upper bound for f_{sx} and f_{sy}. In order to have a safety margin, the sclera force control methods were activated in advance at 100 mN such that the robot would have enough time to prevent the sclera force from reaching 120 mN. Therefore the the parameter

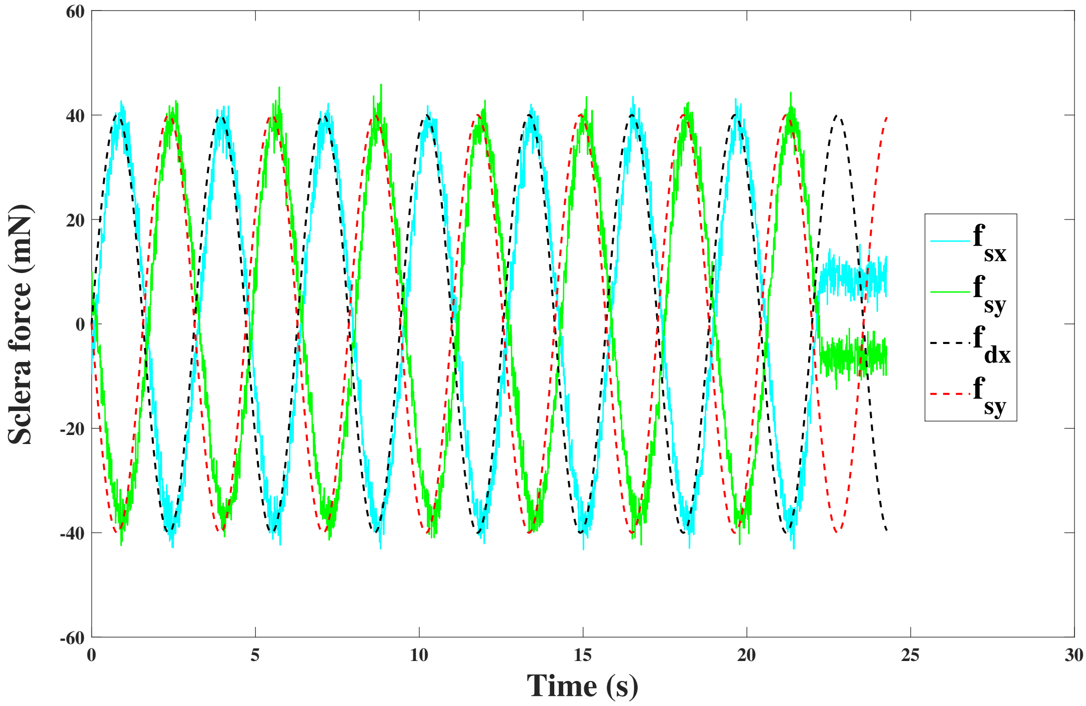

Figure 2.10: Implementation of the adaptive sclera force control for sinusoidal reference trajectories, $f_{dx} = 40sin(2t)$ mN and $f_{dy} = -40sin(2t)$ mN

U in (2.20) and (2.21) was set to 100 mN. To control the robot, a user held the force-sensing tool shaft (Fig. 2.3) and inserted it through the hole on the sclera of the eye phantom and manipulate the eyeball while viewing the procedure through the microscope. The user tried to follow the colored vessels (Fig. 2.8) with the force-sensing instrument tip. As it is depicted in Fig. 2.3 a secondary non-force-sensing instrument was provided to facilitate rotating and moving the eyeball. The results for this experiment are shown in Fig. 2.11.

Third, in order to check the adaptive insertion depth control, similar procedure was followed and the user tried to exceed the safe boundary for insertion depth to see how the robot reacts. For this part of the experiment the upper

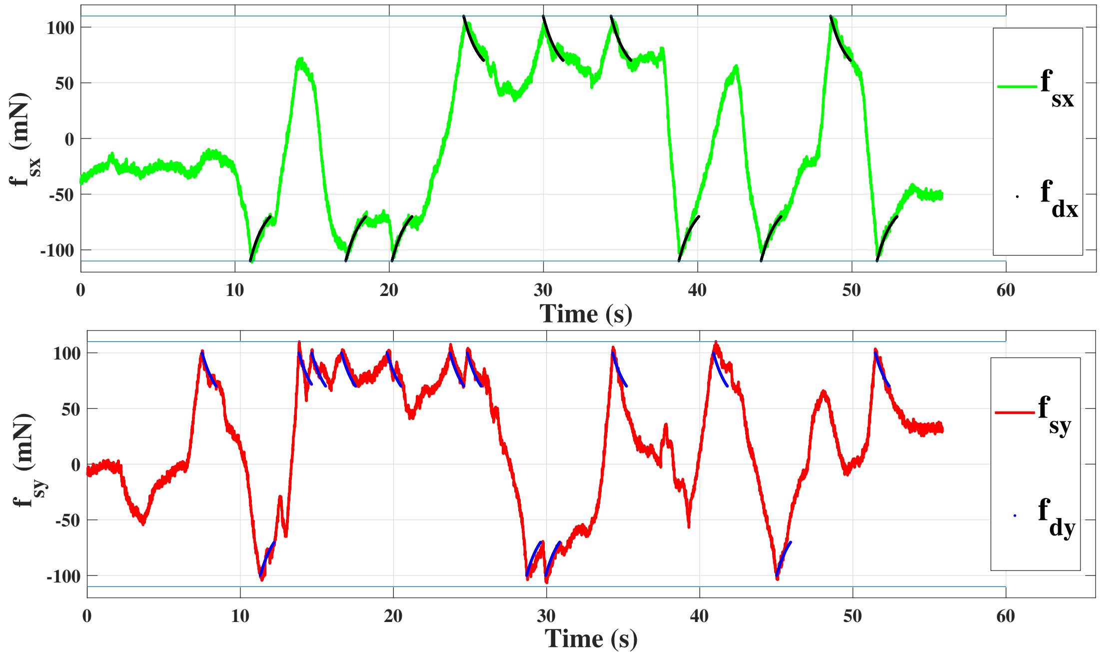

Figure 2.11: Variations of f_{sx} (top) and f_{sy} (bottom) for vessel following task, the discontinuous curves in each plot indicate the desired exponential f_{dx} and f_{dy} for the interval when the corresponding adaptive controller is activated (when $|f_{sx}|$ or $|f_{sy}|$ are between 100 and 70 mN). The horizontal lines of 120 mN and -120 mN are plotted in each figure.

safe limit for insertion depth (U_d in (2.25)) was set to 20 mm. This is because the diameter of the eye phantom is around 25 mm and thus a threshold of 20 has been set after which the adaptive control for the z direction of the handle frame will be activated to retract the tool and reduce the insertion depth to safe ranges. The control switched back to the normal admittance control of the robot after insertion depth is less than 17 mm. The results for this experiment are shown in Fig. 2.12.

Fig. 2.10 demonstrates that using the adaptive control the robot is able to follow the desired sinusoidal force for f_{sx} and f_{sy} with comparatively small

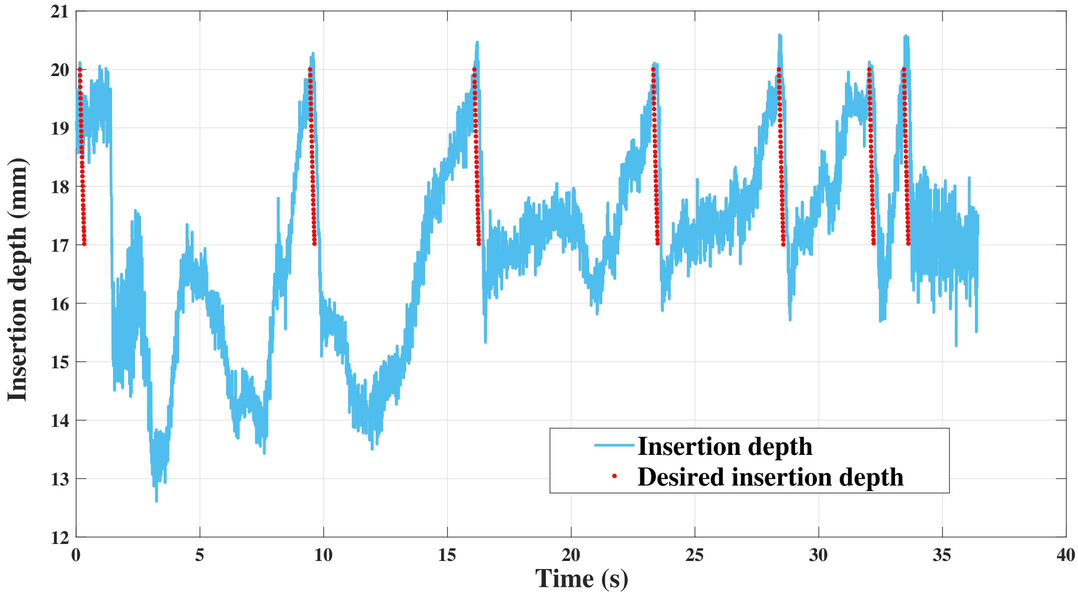

Figure 2.12: Illustration of insertion depth adaptive control when the insertion depth exceeds 20 mm. Adaptive control is active when $17 < d < 20$ mm.

amplitude of 40 mN with good accuracy. In the last part of Fig. 2.10 (from time $t = 23s$ to $t = 25s$), the desired trajectories are not followed because the adaptive control is stopped after $t = 23s$. Based on Figs. 2.11 and 2.12, it is observed that the robot is acting properly to bring down the sclera force components or the insertion depth through their desired exponential trajectories which are shown with interrupted discontinuous lines with short lengths (the period when the adaptive control is activated) in each figure. The reason for such short lengths is that using the adaptive controls the SHER requires only a very small autonomous motion (up to 2 mm) to return the sclera forces or insertion depth to safe limits. Therefore, the period of time the adaptive controls are active would be short.

The reason for choosing an exponential desired trajectory is that it has steep slope at the moment of safety violation for sclera force or insertion depth, so the robot will act fast enough at the start of the incident to prevent any harm. Moreover, the exponential function drops fast enough to reach to the safe levels.

It is also important to note that in the provided figures the real sclera force or the insertion depth may deviate slightly from their desired trajectories. The reason is that as mentioned before, when the robot is switched to adaptive control, the relevant values in V^h_{des} are computed based on the adaptive controller and all the other entities of V^h_{des} are still calculated based on (2.7). Thus, for example, for the rotational movements (last three elements of $\dot{X}^b_d$) the robot is always obeying the user's force, F^h_h. This rotational motion of the robot would affect the control variables most notably the scleral force causing a deviation from the desired trajectories. However, the adaptive controller tries to account for this and as it is observed the control variables continue to follow their desired trajectories with an acceptable accuracy.

2.6.2 Multi-user Clinicians Experiments

The goal of this study is to evaluate the ACC and ANC control methods for robot-assisted eye surgery during clinician use. After securing approval from the Johns Hopkins Institutional Review Board (IRB) with the protocol number HIRB00000943, we provided the opportunity for surgeon clinicians

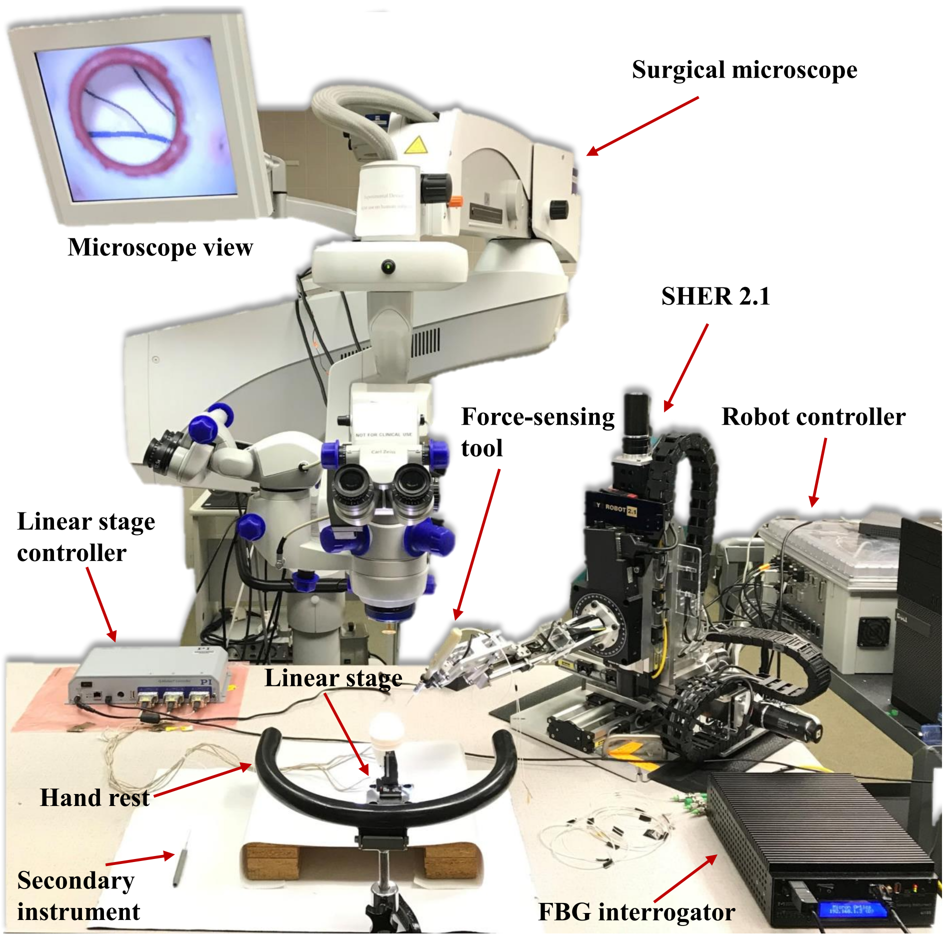

Figure 2.13: Robot-assisted retinal surgery experimental setup. It includes the SHER and its controller, surgical microscope, force-sensing tool. FBG interrogator, eye phantom, linear stage and its controller.

to participate in the experiments at the Wilmer Eye institute, Johns Hopkins Hospital, Baltimore, MD, USA. Ten clinicians (including retina residents and retina fellows) were enrolled in this study after obtaining written, informed consent.

The entire system for conducting the experiments was moved to an operating room in the Wilmer Eye Institute as depicted in Fig. 2.13. The experimental setup contains similar components to what was explained under 2.9. In addition, a piezo-actuated linear stage (Q-Motion Stages, PI Motion and Positioning, MA, USA) is used to simulate patient disturbances (e.g. from patient head motion etc.) during the experiments (Figs. 2.13 and 2.14-b). The reason for adding the disturbance simulators is that these are a main source of sclera force variations during robot-assisted surgery, therefore simulating these disturbances simulates the real life system requirements. This insures the sufficiency of the control methods implemented. The piezo-actuated linear stage and its motion controller are depicted in Fig. 2.13. We programmed the motion controller to generate random one-dimentional step motions at random times to simulate patient head disturbance. First, the stage starts moving after T_s seconds which has a uniform distribution of $U[5, 10]$ (s). $U[5, 10]$ (s) indicates uniform distribution between $t = 5$ and $t = 10$ (s). Then the stage generate a step motion M based on a uniform distribution $[-3, -1] \cup [\ 1,\ 3]$ (mm). After reaching the target position M, the stage waits there for a random time generated based on a uniform distribution $U[1, 3]$ (s) and then returns to its origin. The procedure continues while the user is performing the experiments.

During the experiments, the users were asked to perform "vessel following" which is a common task in vitreoretinal surgery. Users typically hold the force-sensing instrument in their dominant hand and a secondary tool in their non-dominant hand Fig. 2.14. For ease of manipulation, the secondary tool is provided but it does not have any force sensing capabilities. Of note, retinal surgery is typically performed bimanually. For each user the experiments consisted of three conditions including 1-ACC, 2-ANC and 3- freehand. Latin square was used to create random condition sequence of colored vessels for each user. During all experiments the linear stage provided random lateral motions to the eyeball as explained above.

Each experimental condition involved ten trials of following four colored retinal vessels inside a phantom eyeball (Fig. 2.14-c). In each trial the sequence of colors to follow was a random permutation of the four colors. No identical sequence of four colors was presented to the user.

First, the entire system and the components were explained to each user (No user was considered an expert robot user). After having at least two minutes of training and then demonstrating basic familiarity with the robot and the force-sensing tool, each participant went through the following steps for each trial of the experiment:

- Start the experiments by inserting the force-sensing tool and the secondary tool into the eyeball.
- Keep the force-sensing instrument tip, which is held by the dominant hand close to the home position (Fig. 2.14-c) until a random sequence of four colors is read to the user by the instructor.

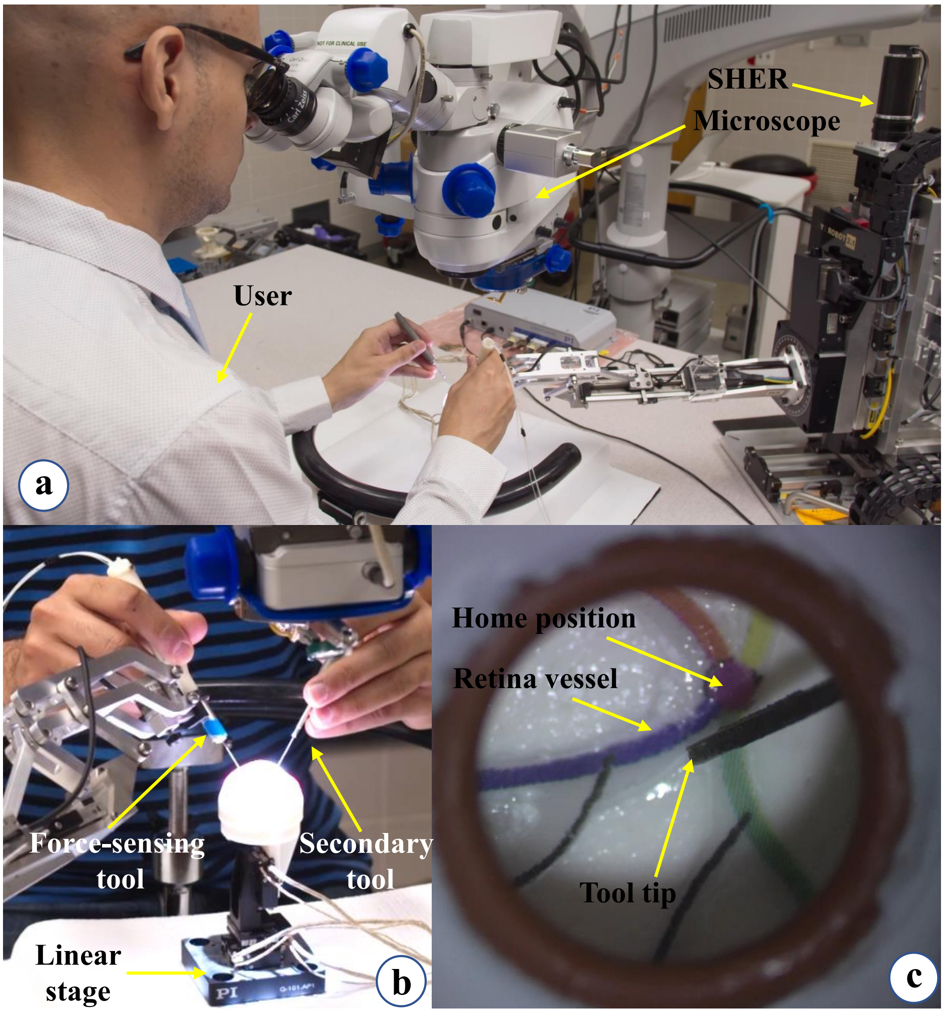

Figure 2.14: User study illustration. (a) The user is looking into the microscope and following the retinal vessels with the force-sensing tool tip. (b) This view shows how the user inserts the force-sensing and the secondary tools into the eyeball which is attached to the linear stage. (c) Microscope view showing the painted retinal vessels.

- Follow the sequence of four retinal vessels with the tip of the force-sensing instrument.
- Perform the ANC, ACC and the freehand groups, repeating for ten trials in each group.

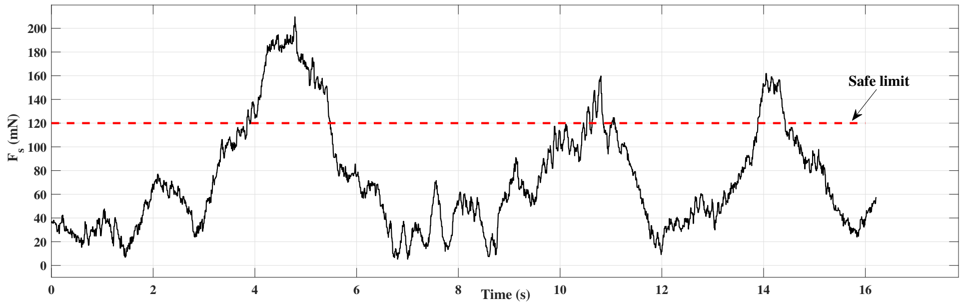

Figure 2.15: Plot for sclera force in freehand experiment for one of the users.

At the end of data collection, the users were asked to subjectively rate, on a scale of 1 (very bad) to 5 (very well), how well each operation mode assisted with task performance. A questionnaire similar to NASA TLX was provided to the users to fill out regarding this part.

2.6.2.1 Results and Discussion for Multi-user Experiments

For each of the users, all of the experiment data including sclera forces, insertion depth, robot position and velocity, time information and etc. were recorded during the freehand, ACC and ANC experiments. The thresholds for activating the adaptive sclera force control methods are similar to what was explained in Section 2.6.1. The activation force for adaptive controls (U) is flexible and can be set to any other value if the safety limit should be changed.

A time window of sclera forces for freehand, ACC and the ANC experiments as a sample for one of the users are plotted in Figs. 2.15, 2.16 and 2.17, respectively. Fig. 2.15 depicts the magnitude of sclera forces for the freehand

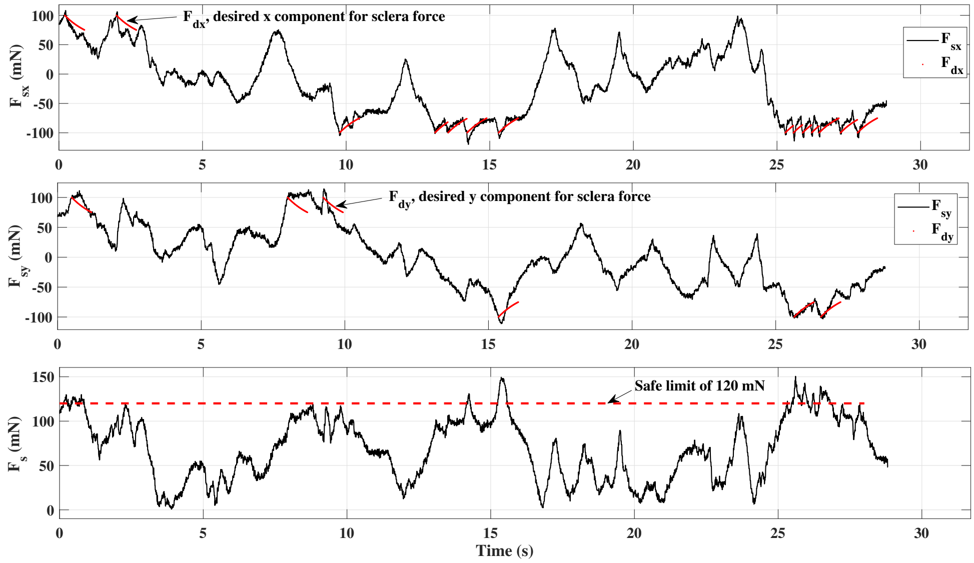

Figure 2.16: Plot for sclera force in ACC experiment for one of the users.

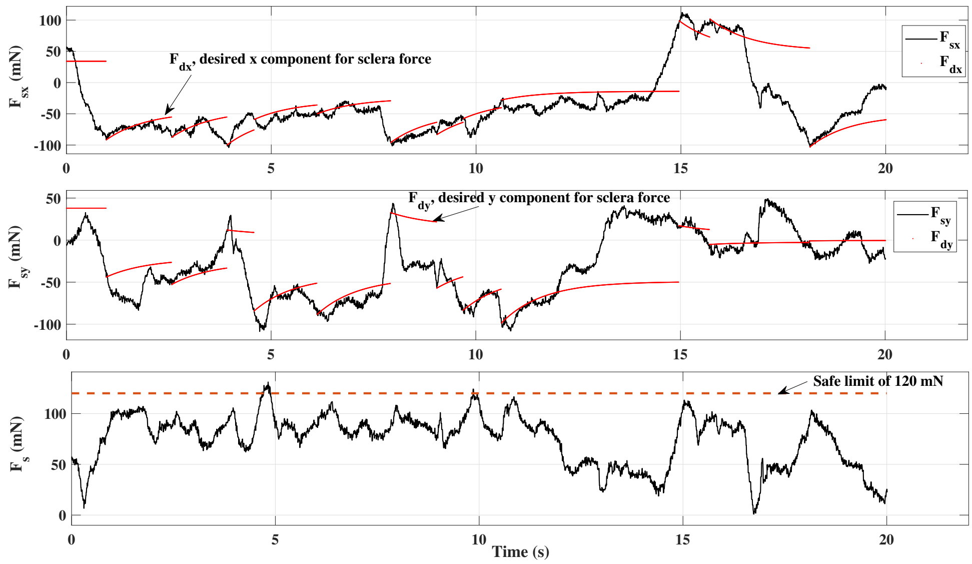

Figure 2.17: Plot for sclera force in ANC experiment for one of the users.

experiment for one of the users. This figure indicates that the clinician occasionally oversteps the 120 mN limit. The red short lines in the F_{sx} and F_{sy} plots for Figs. 2.16 and 2.17 indicate the reference safe trajectory attributed to each component of sclera force (f_{dx} or f_{dy}) for the period when the ACC or

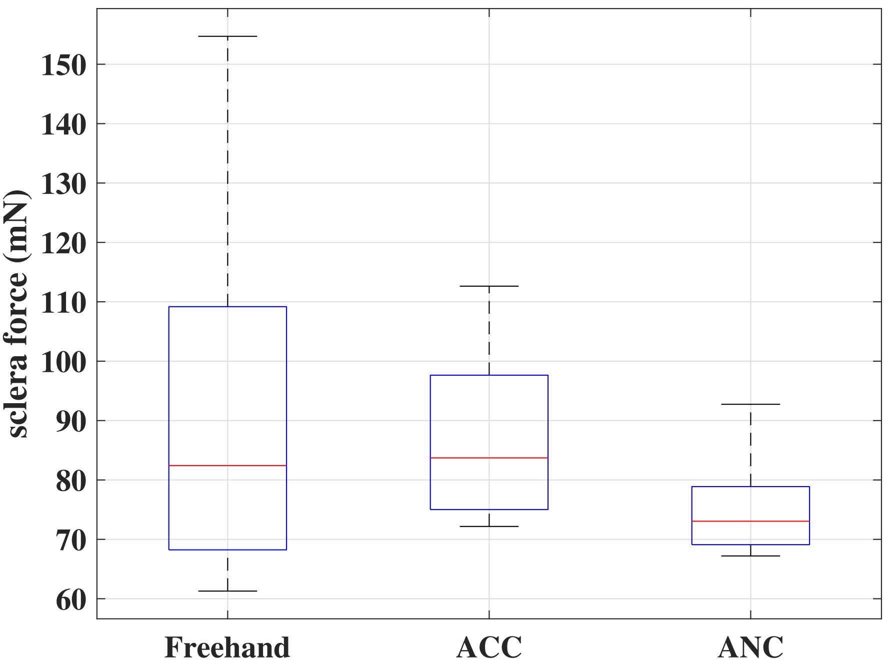

Figure 2.18: Boxplots of sclera forces for all clinicians for the freehand, ACC and the ANC experiments.

ANC controls are activated. The third subplots in Figs. 2.16 and 2.17 show the magnitude of sclera forces for ACC and ANC, respectively. As it is observed, although the ACC method is able to generally maintain the forces in a safe range, a few events of exceeding the safe level are recorded. The ANC method reduces the number of high force events (greater than 120 mN) as compared to the ACC method. In other words, as it can be seen the ANC method is able to better keep the F_s under the 120 mN limit. It is noted that the sclera force components sometimes do not perfectly follow the desired trajectories which are plotted in red. Such force disturbances are often attributed to the secondary tool use. The secondary tool (Fig. 2.14-b) can move the eyeball, therefore, im-

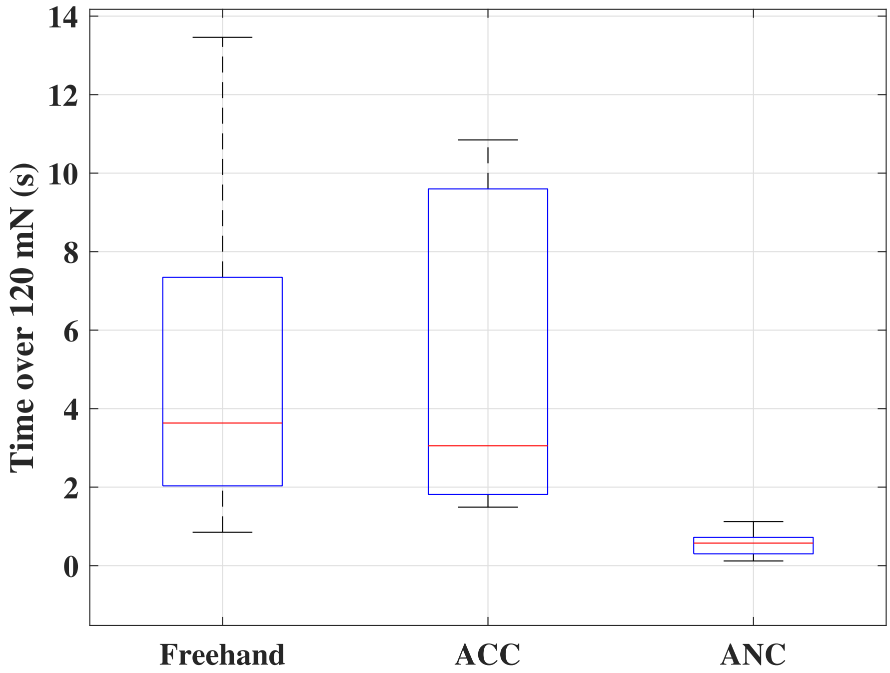

Figure 2.19: Boxplots of time spent on forces more than 120 mN for all clinicians for the freehand, ACC and the ANC experiments.

plying scleral forces on the force-sensing tool. Although this source of disturbance is countered by the robot in real time to provide safe force maintenance, the robot is not perfectly able to keep the sclera forces on desired trajectories. It does however still limit the high force events to the sclera as it can be seen in Figs. 2.16 and 2.17.

The time spent at forces over 120 mN, the experiments total time, and the average sclera force are calculated for all clinicians and represented in boxplotes in Figs. 2.18-2.20. Fig. 2.19 shows that the ANC method significantly reduces the time spent at sclera forces greater than the 120 mN limit, although the ACC method also maintains the sclera forces as safe as the freehand case.

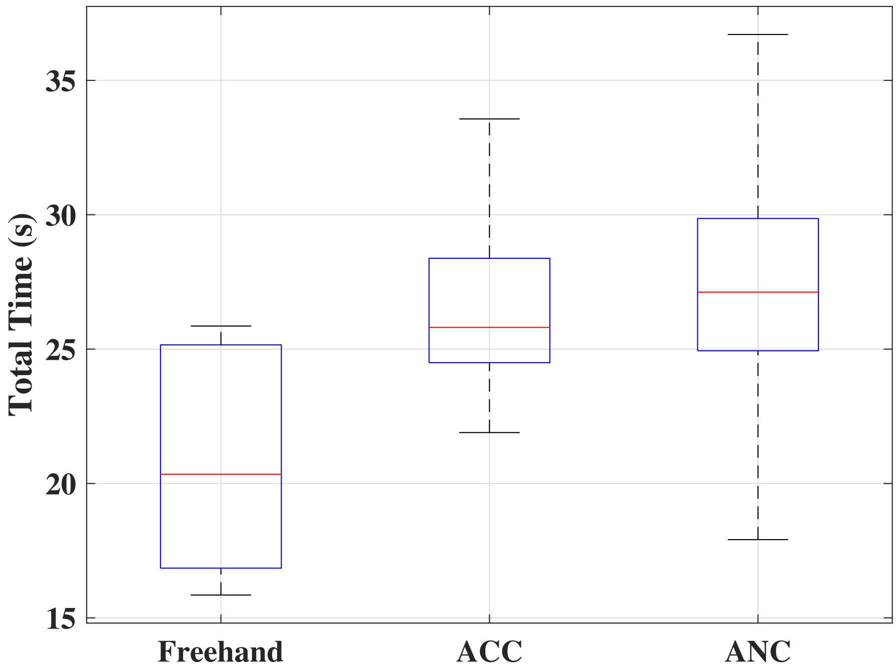

s

Figure 2.20: Boxplots of total time for all clinicians for the freehand, ACC and the ANC experiments.

Improvements in force reduction for safe tool manipulation resulting from both the ACC and ANC methods are countered by increases in the total time to complete the experiment, as it is seen in Fig. 2.20. Fig. 2.18 indicates that in the freehand case, the average of sclera forces for some clinicians can go as high as 150 mN. However, both the ANC and ACC methods limit the average sclera forces for all users to a lower and more consistent force level. The reason for this is that both control methods allow the robot to counter the source of scleral force increase (e.g. surgeon inadvertently increases the force, the rotational force from the secondary instrument increases the force) and to always keep the force in limits.

Table 2.1: Average results for all users over all experiments. The value in the parenthesis indicates the standard deviation.

	Total Time (s)	Total time above 120 mN (s)	Time percentage spent over 120 (mN)	Average sclera force (mN)
Freehand	21.0 (2.4)	5.0 (2.4)	24%	92.3 (53.4)
ACC	26.6 (3.2)	5.0 (2.3)	19%	87.4 (32.0)
ANC	27.4 (3.4)	0.6 (0.4)	2%	75.2 (24.3)

Table 2.1 provides the average results for all users. The fourth column (time percentage spent over 120 mN) is the division of the corresponding average values of the third column (total time above 120 mN (s)) to the second column (total Time (s)). As it can be seen the ANC method is able to keep the unsafe time percentage as low as 2%.

Table 2.2 compares the results of Table 2.1 and provides the corresponding p-values. Two-sample t-test was used to compute the p-values in Table 2.2. The null hypothesis in the t-tests is that the means of tested control methods for the associated parameter (sclera force, total time, time over 120 mN) are the same. Small p-values (< 0.05) rejects the null hypothesis. For example, we can see from Table 2.2 that the p-value for comparing the freehand-ANC unsafe times (time over 120 mN) is 0.005. This indicates that the reduction of average unsafe time from 5 (s) to 0.6 (s) from freehand to ANC as indicated in Table 2.1 is statistically significant. In [42], the authors have conducted a user study to compare vitreoretinal robot-assisted and manual surgeries. Their results indicate that the robot-assisted case is significantly slower than the

Table 2.2: p-values for the results provided in Table 2.1.

Sclera Force	Freehand	ACC	ANC
Freehand	-	0.67	0.13
ACC	0.67	-	0.03
ANC	0.13	0.03	-
Total Time	Freehand	ACC	ANC
Freehand	-	0.004	0.005
ACC	0.004	-	0.7
ANC	0.005	0.7	-
Time over 120	Freehand	ACC	ANC
Freehand	-	0.97	0.005
ACC	0.97	-	0.002
ANC	0.005	0.002	-

manual surgery for both novices and experienced surgeons. The total time results represented in Table 2.1, is consistent with the earlier results reported in [42]. As we can see, the average total time for the freehand experiment is less than the ACC and ANC conditions. The p-values provided in Table 2.2 indicates that this increase in the experiment total time when moving from freehand to robot-assisted is statistically significant.

The NASA TLX questionnaire results are summarized in the spider plot shown in Fig. 2.21. Within the questionnaire the quality of six parameters of user performance (meaning the quality of performing surgical tasks and technical maneuvers related to the surgical procedures), physical demand, comfort, ease of targeting the tool tip, nature of the block from the robot, frustration for

Table 2.3: p-values for the questionnaire results provided in Fig. 2.21.

P-values	Freehand vs ACC	Freehand vs ANC	ACC vs ANC
Performance	0.1892	0.0637	0.8297
Physical demand	0.0111	0.0172	0.8619
Comfort	0.0401	0.0094	0.6669
Ease of targeting	0.0033	0.0013	0.6652
Block from robot	-	-	0.8086
Frustration	0.2295	0.1964	1

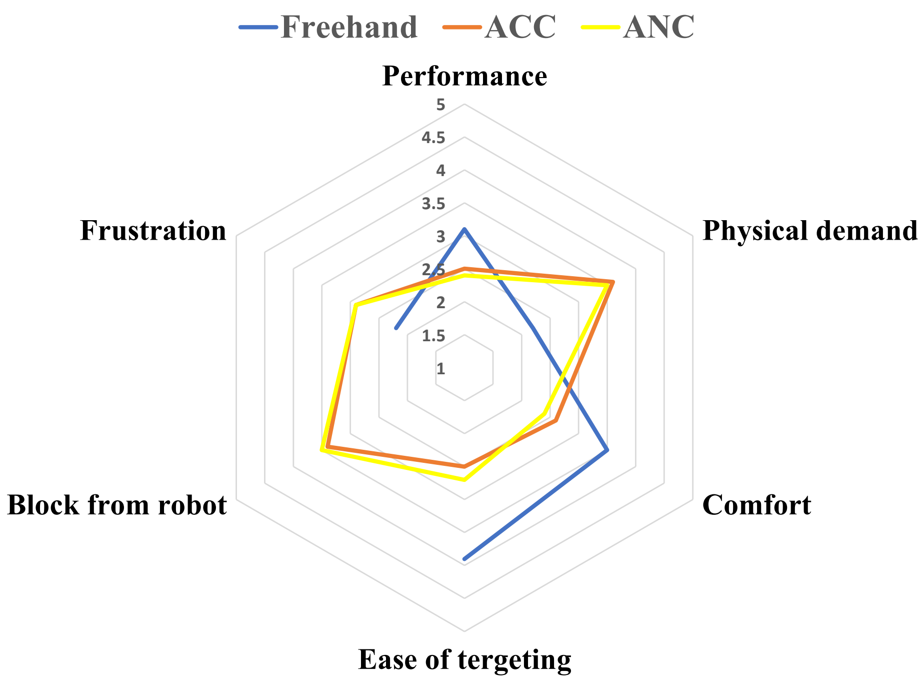

Figure 2.21: Questionnaire results scaled from 1(very bad) to 5(very good).

each of the freehand, ANC and ACC methods were requested of the users. The corresponding p-values for the questionnaire results are shown in Table 2.3 to see if the questionnaire results are statistically significant. As it is shown the results for ACC and ANC methods are closely overlapping indicating that they showed little user preference for one or the other. This is further supported by looking at the large p-values obtained when comparing the questionnaire results for the ACC and ANC methods as shown in the last column of Table 2.3.

For the freehand case which is plotted blue in Fig. 2.21, the parameter “block from robo” does not have any meaning so it is left blank. From Table 2.3 and Fig. 2.21, we can see that for the parameters of “physical demand”, “comfort” and “ease of targeting the tool”, the freehand case is preferred by the users and this result is statistically significant. The reason is that the users felt the robot was hindering their manipulation whenever the ANC or the ACC controls were activated.

The clinicians reported that they had to apply larger forces to move the robot toward their desired location as compared to the freehand procedure. At these early phases of learning most users wanted less resistance from the robot. This was the dominant complaint of early robot users. Based on equations (2.19) and 2.22, we can see neither of the control methods interfere with the rotational velocities of the end-effector which are the last three elements of the vector V^h_{des}. When the instrument is inside of the eye, a user experienced with the robot utilizes primarily the rotational velocities of the end-effector, i.e. they apply torque to the instrument handle (e.g. similar to a spherical joint motion), to reach different locations inside of the eyeball. In other words, because only the first two elements of V_{des}^h are used for ACC and ANC activation, if the user has mastered the use of rotational velocities for surgery, the amount of interference from the robot with the surgeon's maneuvers, when the ACC or the ANC controls are triggered, will be minimally felt. This method of manipulating the robot may be a matter of learning curve. It was mentioned by one of the users who performed the ANC experiments after ACC (had enough training with the robot before starting ANC) and commented that the ANC method seemed easier than ACC. As stated in Section 2.5.1, the ANC is more preventive and is supposed to allow less comfort for the user. We attribute this preference of ANC over ACC to be the result of learning curve. Regarding this issue, another clinician commented that it would be desirable if they had an ongoing discretion as to when switch between the safety controls (ANC or ACC) and the robot regular motion during the surgery.

Although the ANC and ACC significantly contribute to sclera force safety in a robot-assisted surgery, the users feel more comfortable performing the surgery freehand. As elaborated above, this can be related to learning curve as the users did not have any experience with a robot-assisted eye surgery before. The clinicians may feel more comfortable using the robot integrated with safety-enhancing controls if they receive enough training.

2.7 Conclusion

In this chapter therefore a 1-dimensional adaptive control method was customized for 3-dimensional control of sclera force components and tool insertion depth and then implemented on the velocity-controlled robotic platform SHER. The control method build upon the normal admittance control of the robot and presumably does not interfere with the surgeons surgical maneuvers. The control methods enable the robot to perform autonomous motions to make the sclera force and/or insertion depth of the tool tip to follow pre-defined desired and safe trajectories when they exceed safe bounds. Several experiments were then conducted to evaluate how these three applications may contribute to safe robot-assisted retinal surgery.

In preliminary experiments it was shown that when the adaptive control method is activated, the robot will be able to follow desired safe trajectories for sclera forces and insertion depth. Later two variants of ACC and ANC were evaluated through multi-user clinician studies. The evaluation was carried out by enrolling ten robot-novice ophthalmology clinicians in simulated robot-assisted eye surgeries while the control methods were implemented on the SHER. Based on the results and statistical analysis, we conclude that the ACC and the ANC methods are able to maintain sclera forces within safe boundaries, potentially enhancing safety for retinal surgery patients undergoing robot assisted procedures. It is noted that for robot-novice users the test procedure was more comfortable to be performed freehand, and took longer when using the robot assistance. This was true for both the ACC and ANC control methods. It is possible that significant training may allow users to increase their acceptance of the control methods during retinal surgery. This is potentially important as both control methods successfully reduced the application of forces to the eye.

A future direction of this work is to modify and refine the control methods and the corresponding reference trajectories to enhance surgeon acceptance and comfort while limiting the application of unsafe forces to the eye. It is possible that robot control is most strategically utilized only during selected portions of a given procedure. A user study with clinicians sufficiently trained with the robot compared to inexperienced users is also a potential next area of study.

2.8 Publications

Journal Publications:

1. **Ali Ebrahimi**, Niravkumar Patel, Muller G. Urias, Russell H Taylor, Peter Gehlbach, and Iulian Iordachita *"Adaptive Control Improves Sclera Force Safety in Robot-Assisted Eye Surgery: A Clinical Study"*, in IEEE Transactions on Biomedical Engineering (TBME), vol. 68, no. 11, pp. 3356-3365, Nov. 2021. **(Featured Article)**

Conference Publications:

1. **Ali Ebrahimi**, Niravkumar Patel, Muller G. Urias, Russell H Taylor, Peter Gehlbach, and Iulian Iordachita *"Adaptive Control Improves Sclera Force Safety in Robot-Assisted*

Eye Surgery: A Clinical Study", in IEEE Transactions on Biomedical Engineering, vol. 68, no. 11, pp. 3356-3365, Nov. 2021.

2. **Ali Ebrahimi**, Marina Roizenblatt, Niravkumar Patel, Peter Gehlbach, and Iulian Iordachita, *"Auditory Feedback Effectiveness for Enabling Safe Sclera Force in Robot-Assisted Vitreoretinal Surgery: a Multi-User Study"*, In 2020 IEEE/RSJ International Conference on Intelligent Robots and Systems (IROS) (pp. 3274-3280). IEEE.
3. **Ali Ebrahimi**, Niravkumar Patel, Changyan He, Peter Gehlbach, Marin Kobilarov, and Iulian Iordachita, *"Adaptive Control of Sclera Force and Insertion Depth for Safe Robot-Assisted Retinal Surgery"*, In 2019 International Conference on Robotics and Automation (ICRA), pp. 9073-9079. IEEE, 2019. **(Best Paper Award in Medical Robotics)**
4. **Ali Ebrahimi**, Farshid Alambeigi, Ingrid E. Zimmer-Galler, Peter Gehlbach, Russell H. Taylor, and Iulian Iordachita, *"Toward Improving Patient Safety and Surgeon Comfort in a Synergic Robot-assisted Eye Surgery: A Comparative Study"*, In 2019 IEEE/RSJ International Conference on Intelligent Robots and Systems, IROS 2019, pp. 7075-7082.
5. **Ali Ebrahimi**, Changyan He, Niravkumar Patel, Marin Kobilarov, Peter Gehlbach, and Iulian Iordachita, *"Sclera Force Control in Robot-assisted Eye Surgery: Adaptive Force Control vs. Auditory Feedback"*, In 2019 International Symposium on Medical Robotics (ISMR), pp. 1-7. IEEE, 2019.
6. **Ali Ebrahimi**, Muller Urias, Niravkumar Patel, Changyan He, Russell H. Taylor, Peter Gehlbach, and Iulian Iordachita. *"Towards securing the sclera against patient involuntary head movement in robotic retinal surgery"*, In 28th IEEE International Conference on Robot and Human Interactive Communication (RO-MAN), pp. 1-6. IEEE, 2019.
7. **Ali Ebrahimi**, Changyan He, Marina Roizenblatt, Niravkumar Patel, Shahriar Sefati, Peter Gehlbach, and Iulian Iordachita, *"Real-time Sclera Force Feedback for Enabling Safe Robot-Assisted Vitreoretinal Surgery"*, In 2018 40th Annual International Conference of the IEEE Engineering in Medicine and Biology Society (EMBC), pp. 3650-3655. IEEE, 2018.

2.9 Publications Contribution

In the publications lists in Section 2.8, the co-authors contributed as follows: Niravkumar Patel helped in the experimental setup development and software implementation and debugging related to the control methods.

Changyan He helped with development of FBG-equipped surgical instrument and the experimental setup.

Farshid Alameigi helped with advising on different sections of the paper and data analysis.

Muller Urias prepared the clinical protocols and lead the the experiments with clinicians at Wilmer Eye Institute.

Marina Roizenblatt helped with the clinical aspects of the work and contributed to the experiment's data analysis and statistical tests.

Chapter 3

State Estimation and Sensor Fusion for Deformable Needle Tip Localization in Robotic Eye Surgery

3.1 Background and Motivation

Among the requirements for reliable assistance from robots during robot-assisted ophthalmic procedures is the need to provide precise measurements of system states e.g. tool-to-tissue interaction forces, tool tip position, and tool insertion depth. Providing this and other sensing information using existing technology would contribute towards development and implementation of autonomous robotic procedures [92], e.g. automatic light probe holding application [93], automated laser photocoagulation [94], retinal vessel cannulation [41], and autonomous surgical tool navigation [95], among other applications. Furthermore, the improvement of sensing capability may directly result in improved performance of control algorithms which rely on those measured variables. Among safety concerns during robot-assisted eye surgeries are the instrument tip position and insertion depth. These signal should be measured accurately as any inadvertent contact between the instrument tip and retinal tissue can result in devastating and permanent eye injury.

The safety concern regarding the tool tip position is further exacerbated when considering the fact that ophthalmic surgical tools are small gauge, flexible and they experience large deflections during the surgery [97]. Such deflections (mainly due to excessive sclera forces), do not generally create problems during manual surgery as experienced surgeons are accustomed to accommodating them during the course of surgery. However, this would hinder the development of semi-autonomous robot-assisted procedures, as the robot does not have continuously correct information regarding needle tip position. The visual modality (e.g. stereoscopic microscope), which is usually present during ophthalmic procedures, has been typically used as a suitable source for monitoring the tip position and implementing vision-based navigation [90, 98, 111, 112,120]. As a recent example, Becker et al. [98] used stereo vision to create virtual fixtures to improve needle tip positioning and control of a piezo-actuated handheld surgical device called Micron [65]. However, the used vision-based algorithm has the following limitations. First, it is difficult to always have the vision system see the tool tip since the only part that vision system can look through is the cornea and the tool tip might not be always visible through the small cornea circle. Secondly, due to the motion of instrument in various depths inside the eye, keeping the vision system to stay focused on the instrument tip during the surgery is difficult and demands specific microscopes. Optical Coherence Tomography (OCT)-based insertion depth and $3D$ position estimations of a needle tip under retina, have also been recently proposed by Cheon et al. [102] and Zhou et al. [103], respectively. In [103], authors assumed that the used needle does not experience large deformations during the procedure and relied on the tool $3D$ rigid model for their calculations. However, surgical instruments utilized in the eye surgery have typically large length to diameter ratio (e.g., less than 25 Gauge, $\phi = 0.5$ mm) and, therefore, are prone to bending with excess sclera forces specially during a robot-assisted manipulation [96].

In Chapter 2, it was shown how FBG sensors are used to measure instrument insertion depth. By inspecting (2.14) which is the equation used for obtaining an FBG-based estimation for insertion depth, we can realize if F_s measurement is accompanied by noise which is inevitable in sensors, then this noise will affect the insertion depth accuracy significantly specially when F_s is small. This happens because F_s appears in the denominator of the second equation in (2.14) where d is calculated. Particularly when the sclera force is zero (no contact between the tool shaft and the sclera) then the FBG-based measurements for d will be completely wrong. This, in turn, prompts us to improve the measurements for insertion depth before using them in any control strategy to have a better performance.

In this chapter, we use a state-estimating Kalman filtering (KF) to simultaneously improve the tool tip position and insertion depth estimates, which used to be purely obtained by robot forward kinematics (FWK) and direct sensor measurements, respectively. To improve tool tip localization, in addition to robot FWK, we also use sclera force measurements along with beam theory to account for tool deflection. For insertion depth, the robot FWK is combined with FBG sensor measurements for the cases where sensor measurements are not reliable enough. The improved tool tip position and insertion depth measurements are validated using a stereo camera system through static and dynamic experiments.

3.2 Contribution

In contrast to the vision and OCT-based methods, and to address the mentioned limitations, this chapter reports formulating of a novel framework for simultaneously improving the estimations of the $3D$ tip position and insertion depth of a generic deformable surgical instrument during robot-assisted eye surgery. Using an FBG-equipped surgical instrument, the vision-independent force-based framework boosts robot sensing capabilities which are crucial for safety enhancement during robot-assisted ophthalmic surgery. The contributions of this chapter are as follows:

1. Develop a state space framework for tool-tip position and insertion depth estimations in robot-assisted eye surgery for a generic FBG-equipped deformable instrument. This innovative formulation is broadly suitable for various filtering and estimation algorithm implementations.
2. Use the developed state space models to obtain a vision-independent force-based stochastic Kalman Filter (KF) approach to improve the estimations.
3. Implement the developed method on the SHER to obtain simultaneous estimations of depth and deflection of a deformable instrument, potentially in the absence of visualization techniques.

4. Evaluate the proposed estimations through different phantom experiments inspired by real surgical scenarios and compare the estimations with the results obtained by rigid-body kinematics and stereo-vision algorithms.

3.3 State Space Models

In this section, two state space models for the evolution of instrument tip position and instrument insertion depth are developed. Each state space model has two equations, where one of them is based on the robot FWK and the other one is based on sensor measurements. A schematic of the deflected instrument inserted into the eyeball is shown in Fig. 3.1. In this figure, point S is the sclerotomy point, which is a fixed point on the eyeball.

The tip coordinate frame $\{E\}$ with the origin G is attached at the tip of the imaginary not-deflected instrument. The unit coordinate axis of frame $\{E\}$ are $[X^e, Y^e, Z^e]$. This coordinate frame is rigid to the robot end-effector.

3.3.1 State Space Model for Insertion Depth

Considering the sclera entry point (called sclerotomy point S which is a fixed point on the eyeball), the tool tip P, and insertion depth d in Fig. 3.1, we can

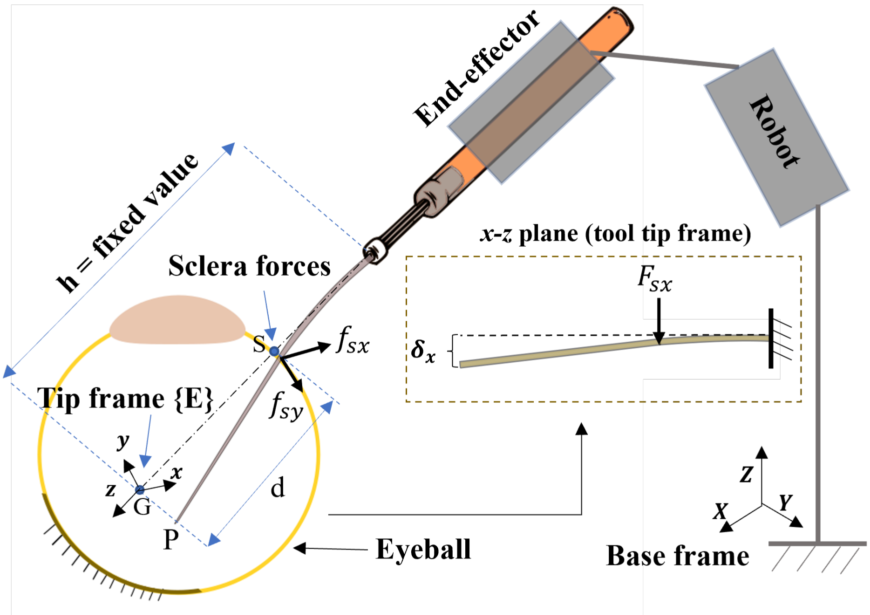

Figure 3.1: Schematic model for a deflected surgical tool inside the eyeball during a robot-assisted retinal surgery showing the sclera forces (f_{sx} and f_{sy} both perpendicular to the tool shaft), tool insertion depth (d), the tool tip (P), tool tip frame and the base frame. The dashed box shows the tool projection on the x-z plane of the tool frame.

write the following equation for the velocity of point G:

$$V_G = V_S + \frac{d}{dt}(dZ^e) \tag{3.1}$$

where V_S is the velocity of point S. If $\vec{\omega}_E$ denotes the angular velocity of the end-effector (and the tip frame) then we can rewrite (3.1) as follows:

$$V_G = V_S + \dot{d}Z^e + \vec{\omega}_E \times dZ^e \tag{3.2}$$

where $\dot{d}$ is the time derivative of the insertion depth d. The cross product term $\vec{\omega}_E \times Z^e$ in (3.2) is perpendicular to Z^e ($(\vec{\omega}_E \times Z^e).Z^e = 0$). Now, if we multiply both sides of (3.2) by Z^e using dot product and assuming V_S is negligible we will have:

$$V_G.Z^e = \dot{d}Z^e.Z^e = \dot{d} \tag{3.3}$$

Using the Jacobian of the robot we can write $V_G = \mathbf{J}_{tip}\dot{\theta}$ where $\dot{\theta} \in \mathbb{R}^5$ is the vector of robot joint velocities. If we discretize (3.3) and integrate a noise uncertainty to it, we will have the FWK-based equation for the insertion depth state space model. If we add the FBG measurements for insertion depth to this discretized equation, then we can have the following linear discrete-time time-invariant (LTI) state space equation for the insertion depth evolution:

$$\begin{aligned} d_k &= d_{k-1} + [\mathbf{J}_{tip}\dot{\theta}]_{k-1}.Z^e_{k-1}(t_k - t_{k-1}) + w^d_k \\ y^d_k &= d_k + v^d_k \end{aligned} \tag{3.4}$$

where the subscript $k \in \mathbb{Z}^+$ denotes the k^{th} time step. Z^e_{k-1} is the unit vector along the z direction of frame $\{E\}$ at time step $k-1$, which is multiplied to $[\mathbf{J}_{tip}\dot{\theta}]_{k-1}$ using dot product. The real-time FBG measurement for insertion depth is denoted by y^d_k. w^d_k and v^d_k denote the Gaussian noises for insertion depth model and FBG measurements at time step k, respectively. $t_k - t_{k-1}$ indicates the time difference between time steps $k-1$ and k. The entire scalar expression $[\mathbf{J}_{tip}\dot{\theta}]_{k-1}.Z^e_{k-1}(t_k - t_{k-1})$ can be considered as the input U^d_{k-1} of the state space model in (3.4).

3.3.2 State Space Model for Tool Tip Position

We have been able to measure the sclera forces by calibrating the FBG sensors and used them in different control strategies [113, 117]. In this part, we aim at improving the tool tip localization, using the existing FBG sensors and the robot FWK information, without any additional equipment.

Considering the tool shaft deflection in the x-z plane of the tip frame (Fig. 3.1), we can find the deflection of the tool tip in the same plane using the beam theory equations as follows [121]:

$$\delta_x = f_{sx}(\frac{(h-d)^3}{3EI} + \frac{(h-d)^2}{2EI}d) \tag{3.5}$$

where h and d are the length of the cantilever beam and the insertion depth of the tool shaft, respectively, as shown in Fig. 3.1. E and I denote the tool modulus of elasticity and the tool second moment of area, respectively. The expression relating δ_x to f_{sx} is denoted by β_x, resulting in $\delta_x = f_{sx}\beta_x$ where β_x is defined as follows:

$$\beta_x = \frac{(h-d)^3}{3EI} + \frac{(h-d)^2}{2EI}d \tag{3.6}$$

A similar projection and calculation can be considered for the tool tip deflection in the y-z plane of the tip frame, δ_y. It is noted that δ_x and δ_y represent the tool tip position in the robot tip frame.

If we denote the tool tip position in the robot base frame at step time k by $P_k \in \mathbb{R}^3$, then in the absence of deflection P_{k-1} and P_k can be related using the following equation which is obtained by discretizing the robot FWK:

$$P_k = P_{k-1} + [\mathbf{J}_{tip}\dot{\theta}]_{k-1}\Delta t \tag{3.7}$$

where Δt is $t_k - t_{k-1}$. So far, two sources of information for the tool tip position are present: 1) the robot FWK based on (3.7), and 2) the tool tip position estimation based on the sclera forces obtained from the FBG in (3.5). The former is always available but does not take into account the tool deflection. The latter does consider the tool deflection, however, it requires a consistent contact between the tool shaft and the eyeball, which is not always the case in a typical retinal surgery practice. Therefore, combining these two sources of information using KF will be a viable strategy to obtain a more accurate tool tip localization.

If we can assume that the z coordinate variation of the tip position in the tip frame is negligible, we can define the tool tip deflection vector in the tip frame as $\Omega = [\delta_x, \delta_y, 0]^T$. The tool tip position in the base coordinate frame (P) can be related to the vector Ω using (3.8):

$$\Omega = \mathbf{R}_{be}^T P - \mathbf{R}_{be}^T S_{be} \tag{3.8}$$

where the matrix $\mathbf{R}_{be} \in SO3$ and vector $S_{be} \in \mathbb{R}^3$ are the rotational and translational parts of the homogeneous transformation between the base frame and the tip frame. If we plug the force-deflection relationship (3.5) in (3.8) for the elements δ_x and δ_y Ω, we can write the following matrix equation between the FBG-based sclera force readings and the tool tip position:

$$\underbrace{\begin{pmatrix} f_{sx} \\ f_{sy} \\ 0 \end{pmatrix}}_{F_s} = \underbrace{\begin{pmatrix} \beta_x^{-1} & 0 & 0 \\ 0 & \beta_y^{-1} & 0 \\ 0 & 0 & \beta_z^{-1} \end{pmatrix}}_{\Gamma} (\mathbf{R}_{be}^T P - \mathbf{R}_{be}^T S_{be}) \tag{3.9}$$

β_z^{-1} can be any non-zero value. The reason is that by having a non-zero value for β_z^{-1} we can enforce the realistic assumption that the third element of $R^T\mathbf{P} - R^T S$, which would be the third element of Ω is zero. Additionally, enforcing this assumption in the sensor measurements equation makes the system observable, which is a necessary requirement for KF to work properly. Using the terms F and Γ, which are defined in (3.9), we can rewrite (3.9) in the following form:

$$F_s + \Gamma R^T S = \Gamma R^T \mathbf{P} \tag{3.10}$$

Now if we denote the left hand side of (3.10) with Y^P, using (3.7) and (3.10) and adding proper Gaussian noise terms to them, the final state space equations for tool tip position written in step time format will be as follows:

$$\begin{aligned} P_k &= P_{k-1} + [\mathbf{J}_{tip}\dot{\theta}]_{k-1}(t_k - t_{k-1}) + W^P_{k-1} \\ Y^P_k &= \underbrace{[\Gamma \mathbf{R}^T_{be}]_k}_{\mathbf{H}_k} P_k + V^P_k \end{aligned} \tag{3.11}$$

In (3.11), W^P_k and $V^P_k \in \mathbb{R}^3$ denote the Gaussian noises for tool tip model and sensor measurements at time step k, respectively. In (3.11), the first equation is the discretized version of FWK accounting for the contribution of the robot motion to the variations of the tip position. The second equation in (3.11) is the sensor measurement for instrument deflection caused by sclera forces based on (3.10). It is noted that (3.11) is a linear but time-varying state space model because the matrix $\mathbf{H}_k$ is time-dependent.

3.4 Kalman Filtering for Insertion Depth and Tool Tip Position Estimation

KF is one the most popular and fundamental stochastic-based parameter estimation tools for analyzing and solving a wide class of optimal estimation problems [122]. Loosely speaking, KF is a minimum variance unbiased estimator that provides a recursive method of estimating the state of a linear dynamical system in the presence of noise by simultaneously maintaining estimates of both the mean and the error covariance matrix $(E[X], \mathbf{M})$ of the state vector ($X_k \in \mathbb{R}^n$) at time step k [123]. One of the primary applications of KF is when a known but imprecise state-space model representing an evolving dynamics for state variables X_k and noisy sensor measurements ($Y_k \in \mathbb{R}^m$) are available. KF is advantageous when one wants to combine these two sources of information to improve the accuracy of the system state variables. A further requirement for KF is having estimations for the system noise covariance matrices. Our problem matches well with the assumptions of KF as it was shown in previous sections.

The mean and covariance estimations of X after propagation (prediction) from step $k-1$ to step k are denoted by ($\hat{X}_{k|k-1}, \hat{\mathbf{M}}_{k|k-1}$), and the mean and covariance after a sensor measurement update (correction) at step k are denoted by ($\hat{X}_{k|k}, \hat{\mathbf{M}}_{k|k}$). We denote the covariance matrix for w^d, v^d, W^P and V^P in (3.4) and (3.11) with q^d, n^d, $\mathbf{Q}^P$ and $\mathbf{N}^P$. The KF process including the prediction and correction steps for insertion depth state equation in (3.4) are defined as follows:

Prediction for d:

$$\begin{aligned}
&\hat{d}_{k|k-1} = \hat{d}_{k-1|k-1} + [\mathbf{J}_{tip}\dot{Q}]_{k-1}.\vec{z}_{k-1}(t_k - t_{k-1}) \\
&\hat{m}^d_{k|k-1} = \hat{m}^d_{k-1|k-1} + q^d_{k-1}
\end{aligned} \tag{3.12}$$

Correction for d:

$$\begin{aligned}
&\hat{m}^d_{k|k} = \hat{m}^d_{k|k-1} - \hat{m}^d_{k|k-1}(\hat{m}^d_{k|k-1} + n^d_k)^{-1}\hat{m}^d_{k|k-1} \\
&k^d_k = \hat{m}^d_{k|k}(n^d_k)^{-1} \\
&\hat{d}_{k|k} = \hat{d}_{k|k-1} + k^d_k(y^d_k - \hat{d}_{k|k-1})
\end{aligned} \tag{3.13}$$

The output of KF estimation for insertion depth ($\hat{d}_{k|k}$ in (3.13)) is an improved estimation for the instrument insertion depth at each step k. This value is required for computing Γ that is used in (3.9) and (3.11). In other words, the output of KF for insertion depth will be used in the KF prediction and correction equations for tool tip position at each step time k. Using (3.11), the KF process for tool tip position will be as follows:

Prediction for P:

$$\begin{aligned}
&\hat{P}_{k|k-1} = \hat{P}_{k-1|k-1} + [\mathbf{J}_{tip}\dot{Q}]_{k-1}(t_k - t_{k-1}) \\
&\hat{\mathbf{M}}^P_{k|k-1} = \hat{\mathbf{M}}^P_{k-1|k-1} + \mathbf{Q}^P_{k-1}
\end{aligned} \tag{3.14}$$

Correction for P:

$$\begin{aligned}
\hat{\mathbf{M}}^P_{k|k} &= \hat{\mathbf{M}}^P_{k|k-1} \\
&\quad - \hat{\mathbf{M}}^P_{k|k-1}\mathbf{H}^T_k(H_k\hat{\mathbf{M}}^P_{k|k-1}\mathbf{H}^T_k + N^P_k)^{-1}\mathbf{H}_k\hat{\mathbf{M}}^P_{k|k-1} \\
\mathbf{K}^P_k &= \hat{\mathbf{M}}^P_{k|k}\mathbf{H}^T_k(\mathbf{N}^P_k)^{-1} \\
\hat{P}_{k|k} &= \hat{P}_{k|k-1} + \mathbf{K}^P_k(Y^P_k - \mathbf{H}_k\hat{P}_{k|k-1})
\end{aligned} \tag{3.15}$$

where $\hat{P}_{k|k}$ is the improved estimation for deflected instrument tip position. A block diagram of the entire estimation framework is represented in Fig. 3.2

3.5 Validation

In order to perform the validation experiments for the KF estimations for the tool tip position and the insertion depth, a stereo camera system and the robot FWK have been used, respectively. The setup for the validation experiments is shown in Fig. 3.3 and are explained in the following sections.

3.5.1 Validation for Insertion Depth

In order to validate the KF output for the insertion depth, a phantom was made out of rubber with a small hole in it, mimicking a tool insertion spot on sclera during a real surgery (Fig. 3.3-c). The phantom was fixed in space and

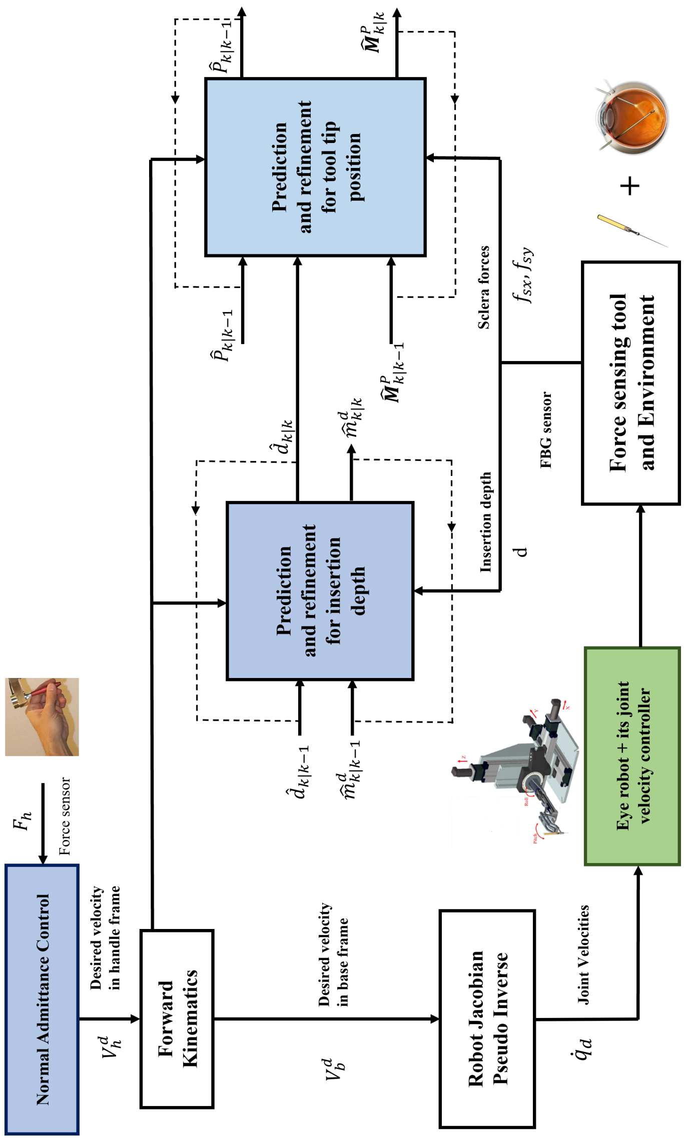

Figure 3.2: Block diagram for the closed-loop system showing the SHER normal impedance control and the KF estimations for tool tip position and insertion depth

the robot was then moved to a configuration such that the tool tip was touching the small hole on the rubber. Using the robot FWK, the position of this space-fixed point was obtained and recorded in the robot base frame, denoted by Tip_E

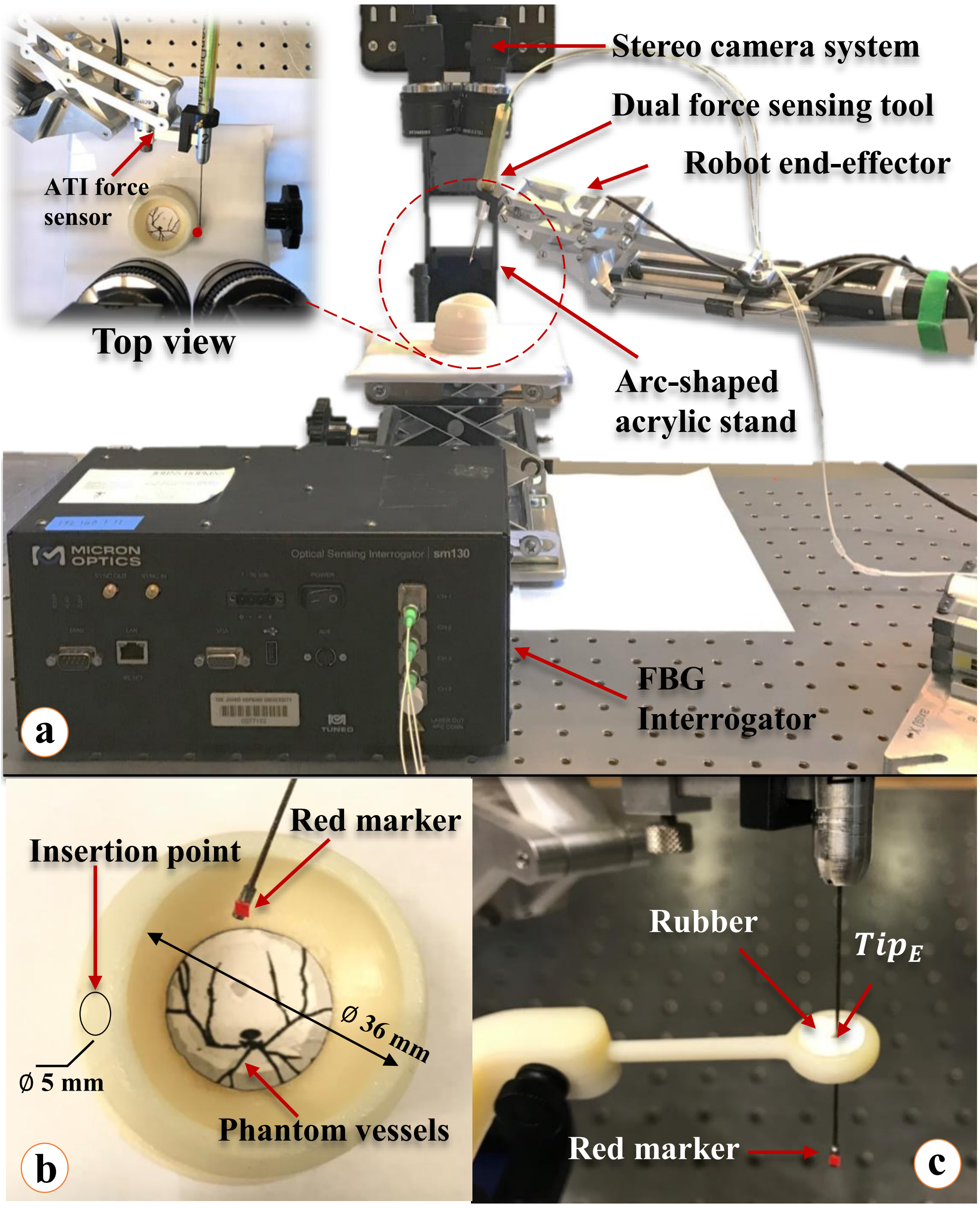

Figure 3.3: Experimental setup. (a) Hardware components including the force-sensing tool, SHER, FBG interrogator, Stereo camera system, Eye socket. (b) A close-up view of the tool tip and the vessels on the eye socket for the case study. (c) The rubber with a hole used for the validation experiments for insertion depth.

(Fig. 3.3-c). The tool was then inserted into the rubber phantom and at each sample time the distance between the location of the point G in Fig. 3.1 (which can be obtained via FWK) and the recorded point Tip_E was calculated and considered as the ground truth for the insertion depth. The KF output for the insertion depth estimation and the FBG-based insertion depth measurements were then compared to the ground truth for validation. It is noted that the insertion depth (d) is defined as the length of the tool inside the eyeball along the imaginary straight (not deflected) tool as shown in Fig 3.1.

3.5.2 Validation for Tool Tip Position

To validate the KF estimations for the tip position of the needle, a stereo camera setup with the resolution of 1024×768 was used to track a red marker attached to the tip of the needle (Fig. 3.3). The stereo camera pair was calibrated using the stereo Camera Calibration Toolbox in MATLAB (MathWorks, Natick, MA) with an overall mean error of 0.4 pixels. For each stereo image pair, the $2D$ pixel location of the marker center was found by applying a color segmentation algorithm. The thresholds for the segmentation were determined experimentally using an interactive Python GUI. The intrinsic and extrinsic parameters from the calibration procedure were then used in a custom-written Python code to find the corresponding markers within the two color-segmented images and obtain the $3D$ location of the marker in space by triangulation [124]. An erosion morphological operation, followed up with a dilation were applied to the segmented images to remove potential noise in the color segmentation algorithm. Of note, the 0.4 pixel error during the calibration process results in $0.2\ mm$ mean $3D$ position accuracy error when triangulating and measuring the distance between two markers with known pre-determined spacial locations on a custom-designed validation jig. Each of the cameras in the stereo camera system has its own coordinate frame. However, after triangulation the position of the red marker will be reported with respect to one of the camera frames.

Because the outputs of the KF for the tool tip position are reported in the robot base frame, in order to compare the ground truth (camera measurements for the red marker position) with the KF outputs, a frame registration step should be performed to obtain the homogeneous transformation that relates these two frames, which is defined in (3.16).

$$\mathbf{F}_{bc} = \begin{pmatrix} \mathbf{R}_{bc} & S_{bc} \\ \mathbf{0}_{1\times 3} & 1 \end{pmatrix} \tag{3.16}$$

where the subscript and superscript b and c correspond to the base frame of the robot and the camera frame, respectively. To find the matrices $\mathbf{R}_{bc}$ and S_{bc}, the robot is moved (without deflecting the tool) by a user to different locations around the desired workspace and the tool tip position is recorded both in the camera frame and the robot base frame. Since the robot and the stereo camera system have different data collection frequencies ($200\ Hz$ for the robot and

$15\ Hz$ for the camera system), the same-time data are extracted by synchronising the time stamps of the two systems.

After stacking the $3D$ points for the tool tip measurements in the robot base frame and the camera frame in two $N \times 3$ matrices B and C, where N is the number of synchronised data samples, the following mean values are calculated:

$$\bar{B} = \frac{1}{N}\sum_{i=1}^{N} B_i \quad \text{and} \quad \bar{C} = \frac{1}{N}\sum_{i=1}^{N} C_i \tag{3.17}$$

where B_i and C_i are the ith rows of matrices B and C, respectively. Then, the cross-covariance matrix Σ_{BC} is calculated in (3.18).

$$\Sigma_{BC} = \frac{1}{N}\sum_{i=1}^{N} (B_i - \bar{B})^T (C_i - \bar{C}) \tag{3.18}$$

Next, using (3.18), we form the following 4×4 matrix $Q(\Sigma_{BC})$ [125]:

$$Q(\Sigma_{BC}) = \begin{pmatrix} trace(\Sigma_{BC}) & \Delta^T \\ \Delta & \Sigma_{BC} + \Sigma_{BC}^T - tr(\Sigma_{BC})\mathbb{I}_3 \end{pmatrix} \tag{3.19}$$

where $\mathbb{I}_3$ is the 3×3 identity matrix and the column vector $\Delta = [H_{23} \quad H_{31} \quad H_{12}]^T$ is obtained from $H_{ij} = (\Sigma_{BC} - \Sigma_{BC}^T)_{ij}$.

As shown in [125], the unit eigenvector corresponding to the maximum eigenvalue of $Q(\Sigma_{BC})$ returns an optimal quaternion vector $\vec{q} = [q_0 \quad q_1 \quad q_2 \quad q_3]$, where $q_0 \geq 0$ and $q_0^2 + q_1^2 + q_2^2 + q_3^2 = 1$. Using this quaternion vector, the corresponding optimal value for 3×3 rotation matrix $\mathbf{R}_{bc}$ can be calculated using quaternion to rotation matrix transformations.

$$\mathbf{R}_{bc} = \begin{pmatrix} q_0^2+q_1^2-q_2^2-q_3^2 & 2(q_1q_2-q_0q_3) & 2(q_1q_3+q_0q_2) \\ 2(q_1q_2+q_0q_3) & q_0^2+q_2^2-q_1^2-q_3^2 & 2(q_2q_3-q_0q_1) \\ 2(q_1q_3-q_0q_2) & 2(q_2q_3+q_0q_1) & q_0^2+q_2^2-q_1^2-q_3^2 \end{pmatrix} \tag{3.20}$$

After finding $\mathbf{R}_{bc}$, the vector S_{bc}, therefore, can be obtained using (3.21).

$$S_{bc} = \bar{B}^T - \mathbf{R}_{bc}\bar{C}^T \tag{3.21}$$

Eventually, using (3.16) the homogeneous transformation $\mathbf{F}_{bc}$ can be obtained. This matrix will be used to bring the $3D$ coordinates of the red marker described in the camera frame to the robot base frame.

3.6 Experiment Components and Preparation

The experimental setup is depicted in Fig. 3.3. A dual force sensing tool is attached to the SHER to measure the sclera force components f_{sx} and f_{sy}, as well as the insertion depth d. The instructions given in Section 3.5.1, were followed to conduct the insertion depth validation experiments.

For tool tip position two sets of experiments were conducted including static and dynamic experiments. During static experiments, manual deflections were applied to a stationary instrument shaft while the robot was motionless. Then, the KF estimation for tool tip position was obtained and compared to that of the robot FWK and the stereo camera observation, which is the ground truth.

During dynamic experiments, in order to better evaluate the performance of the developed method in a realistic situation, a retinal vein following task as part of an RVC was mimicked. An eye socket with diameter of $36\ mm$ was 3D-printed and a hole with diameter of $5\ mm$ was created at one side of the eye socket simulating the insertion point for the tool (Fig. 3.3-b). The dual-force sensing tool was then attached to the SHER and moved by a user to the eye socket through the $5\ mm$ hole. The hole was intentionally made larger than the tool diameter to create a range of motion for the tool similar to an actual surgery. In addition, a larger hole enables possibility of performing larger maneuvers by the user, as well as the ability to study various types of contact with the hole edges from different angles and orientations. Although the eye phantom is stationary, the large $5-mm$ hole allows a simulation of eye motion as the tool can be inserted at various angles and orientations as if the insertion point is moving in space. As it can be seen from Fig. 3.3-b, retinal vessels were printed and attached to the posterior of the eye socket phantom. The phantom vessels exhibit similar distribution and arrangement compared to real retinal vessels since they were reconstructed from a real retina image. After inserting the tool through the hole into the eye socket, the user followed the black vessels on the phantom. In this case study, the tool was bent from different locations on the tool shaft in different planes. In addition, in this experiment the tool deflection and robot motion occurred simultaneously.

Two Point Grey cameras were used for the stereo camera system, which were attached to an arch-shaped laser-cut acrylic sheet, clamped to the experiment table (Fig. 3.3). The cameras were placed at approximately 30 cm above the working area of the robot tool tip. Sufficient illumination was provided to make the red marker clear enough for both cameras. During the experiments the robot was moved by the operator in a way such that the tool tip was always visible by both cameras. The images of the stereo camera system were recorded by custom ROS packages (Robot Operating System, a collection of software frameworks for robot software development packages [126]). The images were then used in the Python code mentioned in section 3.5.2 for triangulation and extraction of the tool tip position in the camera frame.

3.6.1 Instrument Mechanical Properties

As it is observed in (3.5), to calculate δ_x (or δ_y) in each sample time, the parameters h, d and EI are required to be determined for the tool shaft. Using the CAD model of the tool, the parameter h was measured to be 60 mm. The parameter d is updated in each loop using the KF output for insertion depth provided in (3.13). The parameter EI is found using the same calibration data that was used to identify the matrices K_I and K_{II} for tool calibration explained in Section 2.5 without performing any additional experiments. As instructed by He et al. [73] and mentioned in Section 2.5, the calibration procedure consists of applying various sclera forces at different points along the tool shaft. In this process, three variables are recorded: 1) the tool shaft deflection at the point where the sclera force is applied, Ω, 2) the distance between the tool tip and the point of application of sclera force, d, and 3) the sclera force (which are obtained from another sensor during the calibration experiments). We know that the deflection of the tool shaft at the point of slcera force exertion is $||\Omega|| = \frac{||F_s||(h-d)^3}{3EI}$. If we plot the value of $||F_s||(h-\mathbf{d})^3$ on the y axis and the value of $||\Omega||$ on the x axis for all data samples recorded during the calibration process, the slope of the line that fits through this point cloud will provide the coefficient $3EI$. In our experiments, this coefficient was obtained to be $3.39 \times 10^6\ mN.mm^2$. The results for identifying $3EI$ for the instrument are plotted in Fig. 3.4.

3.6.2 Robot to Camera Registration

After performing the registration as described in Section 3.5.2 and finding the matrix $\mathbf{F}_{bc}$ in (3.20) and (3.21), a validation experiment similar to what is delineated during the registration process (in Section 3.5.2) was performed.

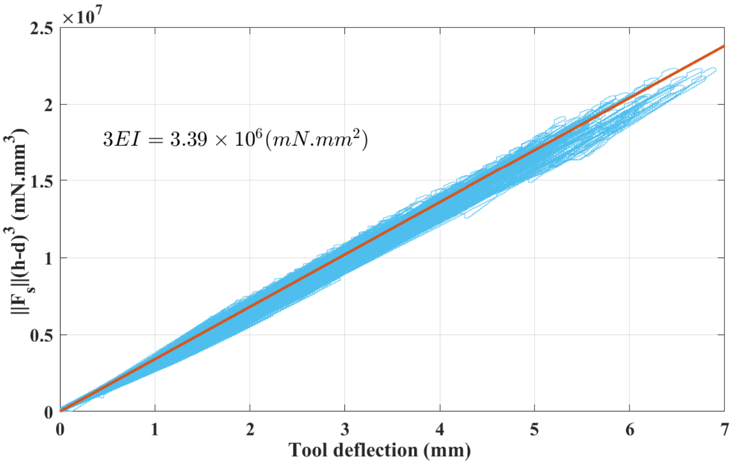

Figure 3.4: The point cloud obtained during the calibration process of the dual force sensing tool. The red line shows the optimal line passed through the point cloud and the slope of this line is an estimation for $3EI$.

This validation data set containing the tool tip position in the camera frame ($C_i' \in \mathbb{R}^3$) and the robot base frame ($B_i' \in \mathbb{R}^3$) , where $i = 1, ..., n$ and n is the number of data points collected during the validation experiment, were then used to calculate the registration error. The ith element of the error vector E is defined as follows:

$$E_i = ||B_i' - (\mathbf{R}_{bc} C_i' + S_b^c)|| \tag{3.22}$$

where $\mathbf{R}_{bc}$ and S_b^c can be found using (3.16). The registration error (the mean value of the vector E) was calculated to be 0.67 mm.

3.6.3 Covariance Matrices for Kalman Filtering

The noise covariance matrices for sensor measurements and models for insertion depth and tool tip position state space models were defined above equation (3.12), and were chosen with trial and error. We assumed the covariance for the insertion depth measurement noise is a function of the sclera force, F_s, since for low sclera forces we cannot rely on the FBG measurements for computing the insertion depth, as discussed in Section 3.1. However, for larger sclera forces, we can obtain reliable FBG measurements for estimating the insertion depth. For this reason, the covariance matrix n^d (which is a scalar here) is chosen the large number of 10^6 when $||F_s|| < 50\ mN$, while for $||F_s|| \geq 50\ mN$ it is set to 0.005. The scalar covariance matrix q^d is set to the fixed value of 0.0025. The $50\ mN$ cutoff was chosen experimentally for best performance. Similarly, the covariance matrix for the measurement noise, $\mathbf{N}^P$ in (3.11), is assigned to diag$(10, 10, 0)$ when $||F_s|| < 50\ mN$, since the F_s measurements are not reliable enough to be used for tip position estimation. The element $(3, 3)$ of the $\mathbf{N}^P$ is set to zero, since in Section 3.3.2 we assumed that the tool deflection does not change the tip position along the tool shaft. Thus, whether or not there exists small or large $||F_s||$, the measurement equations should always give zero value for the tip displacement along the tool shaft. For $||F_s|| \geq 50\ mN$, this matrix is set to diag$(0.002, 0.002, 0)$. The covariance matrix $\mathbf{Q}^P$ is set to the fixed value of diag$(0.01, 0.01, 0.01)$, as well. It is noted that no correlation between different directions of tip position estimation is assumed within the covariance matrices.

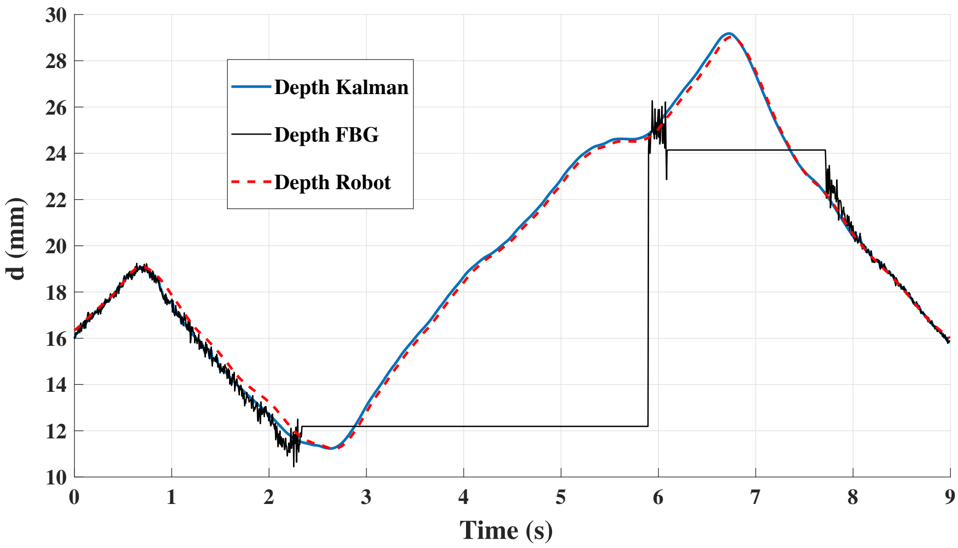

Figure 3.5: Results for the validation experiments for KF for insertion depth. The red dashed curve indicates the gound truth which was measured using the FWK.

3.7 Experiments Results

In this section the results for the validation experiments for insertion depth as well as the static and dynamic experiments for tool tip position estimation are provided.

3.7.1 Validation Results for Insertion Depth

The validation experiment for the insertion depth was performed as explained in Section 3.5.1 and the results are plotted in Fig. 3.5. As mentioned in Section 3.5.1, the ground truth for this case are obtained from robot FWK. The errors between the ground truth and both KF outputs (d) and FBG mea-

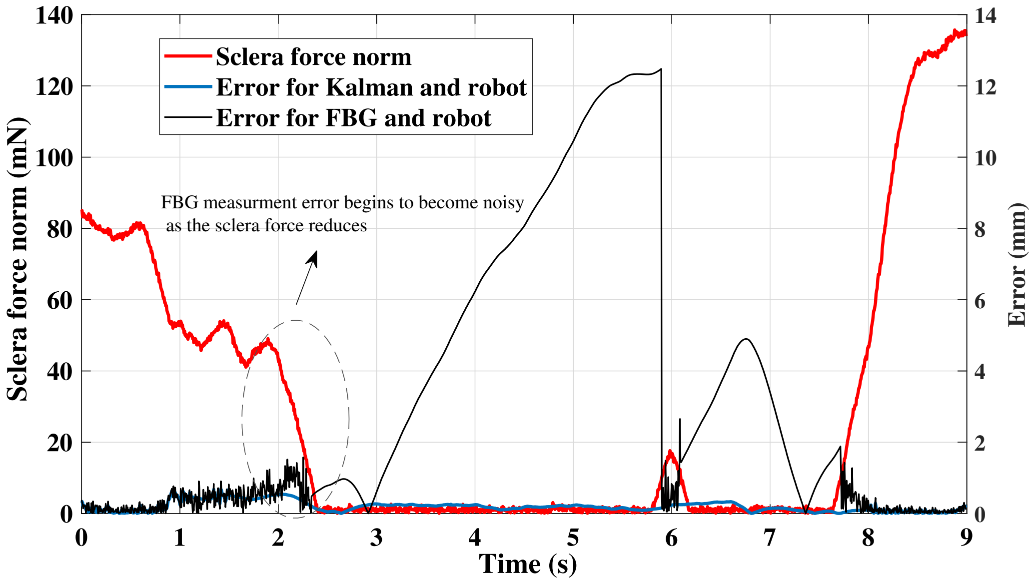

Figure 3.6: Error variations for insertion depth validation experiment. Left y axis: Sclera force norm, $||F_s||$. Right y axis: The error between the KF output and the ground truth (robot) is plotted with blue. The error between the FBG measurements for insertion depth and the ground truth (robot) is plotted with black.

surements for insertion depth y^d are plotted in Fig. 3.6. In the same figure, the sclera force norm ($||F_s|| = \sqrt{f_{sx}^2 + f_{sy}^2}$) is also plotted for the same experiment. In Fig. 3.6 the left y axis is associated with $||F_s||$ and the right y axis is associated with the errors mentioned.

The average error between Kalman output and the ground truth for the time interval of Fig. 3.6 was calculated $0.20\ mm$. The same average error for FBG measurements ($\mathbf{Y}^d$) and the ground truth was $3.14\ mm$.

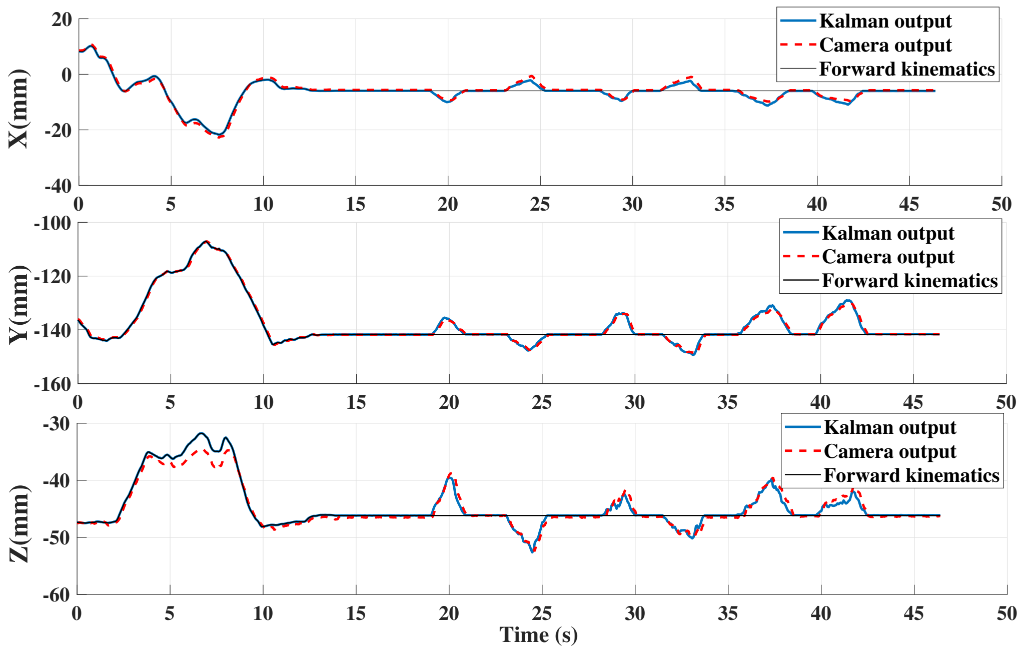

Figure 3.7: Results for the tool tip position validation experiment. The X, Y, Z positions if the tool tip are plotted in the robot base frame.

3.7.2 Validation Results for Tool Tip Position - Static

In this experiment, the location of the red marker was recorded with the stereo camera system and transformed to the robot base frame using (3.16). Meanwhile, the tool tip position values obtained from the KF algorithm and also from the FWK were recorded. The results for this experiment are plotted in Fig. 3.7, showing the tool tip position coordinates in the robot base frame. Similar results for the tool tip estimations are represented in Fig. 3.8, where the errors between the KF output and the robot FWK compared to the ground truth from the stereo camera system are shown. The sclera force norm $||F_s||$ for

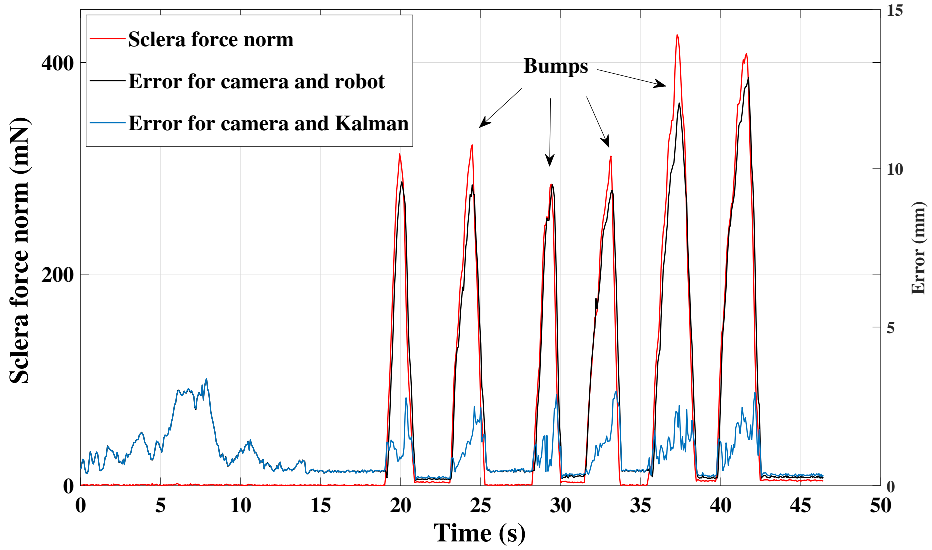

Figure 3.8: Error variations for tool tip position validation experiment. Left y axis: Sclera force norm, $||F_s||$. Right y axis: The error between the KF output and the ground truth (camera) is plotted with blue. The error between the robot FWK and the ground truth (camera) is plotted with black.

the tip position experiment is also plotted in Fig. 3.8.

3.7.3 Validation Results for Tool Tip Position - Dynamic

For the dynamic experiments, the results for tool tip position estimations obtained from the KF, the stereo camera system, and the robot FWK when the user was following the vessels are also plotted in Fig. 3.9. The results for the tool insertion depth are plotted in Fig. 3.10.

The error plot and the sclera forces are shown in Fig. 3.11. The average errors for all three experiments conducted in sections 3.7.1 to 3.7.3 are repre-

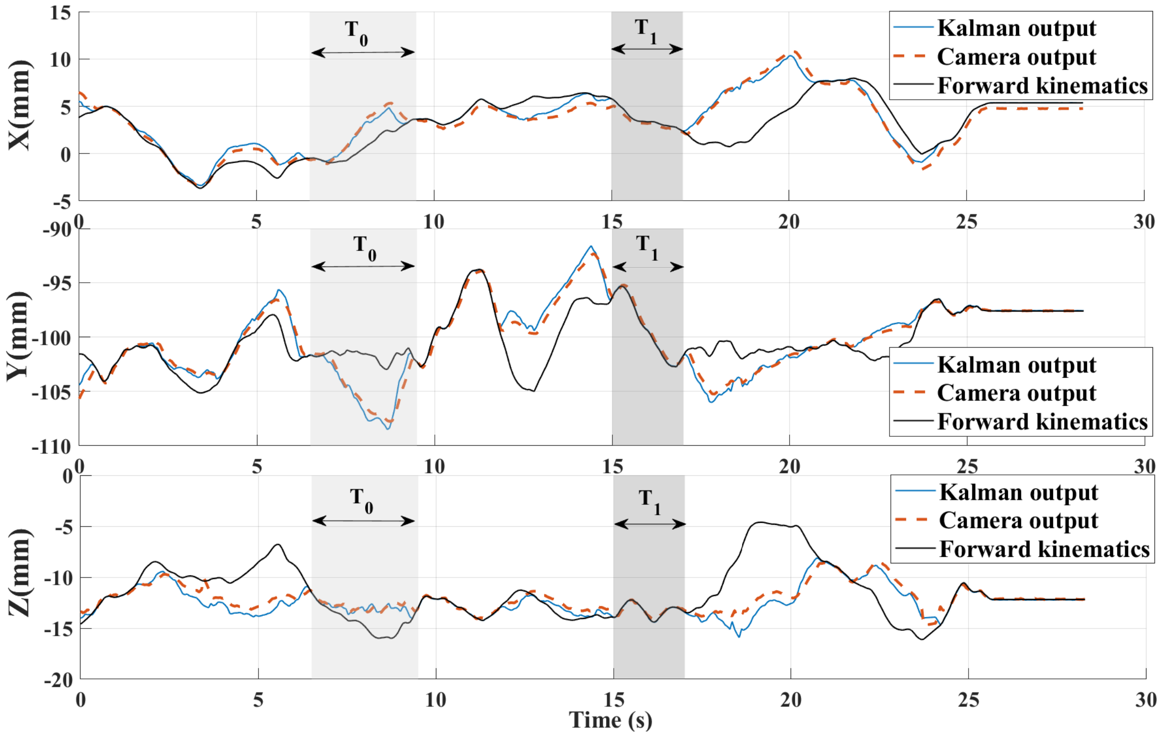

Figure 3.9: Results for the tool tip position during the dynamic experiment. The X, Y, Z positions if the tool tip are plotted in the robot base frame.

sented in Table 3.1. The errors for the insertion depth are scalar values and thus are simply averaged. However, because the errors for tool tip position are 3×1 vectors, the average of the vectors $2 - norm$ are reported in Table 3.1. In this Table, T_0 corresponds to time intervals when there is a significant mismatch (larger than $0.1\ mm$) between the KF output and the associated sensor measurements (FBG for insertion depth and robot FWK for tool tip position). The time interval T_1 includes any time other than T_0 intervals during each experiment. Clearly, T_0 intervals are of higher importance for analysis. While T_0 and T_1 intervals span the entire time axis, only a single sample of them is represented in Figs. 3.9-3.11.

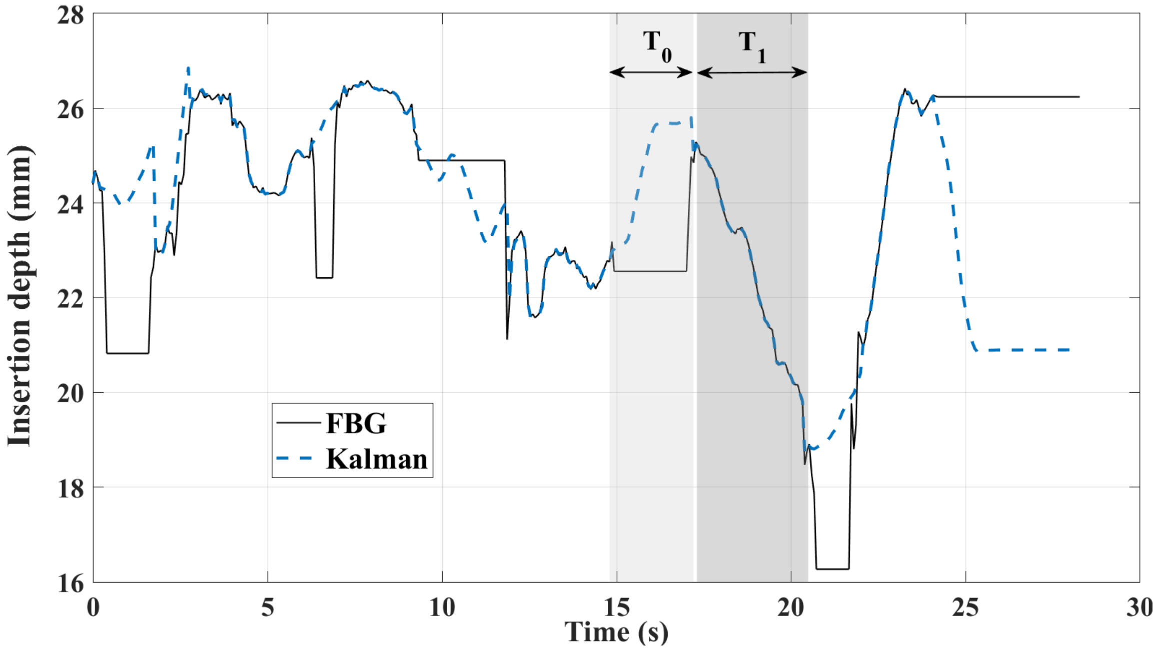

Figure 3.10: Insertion depth variations in the dynamic experiment.

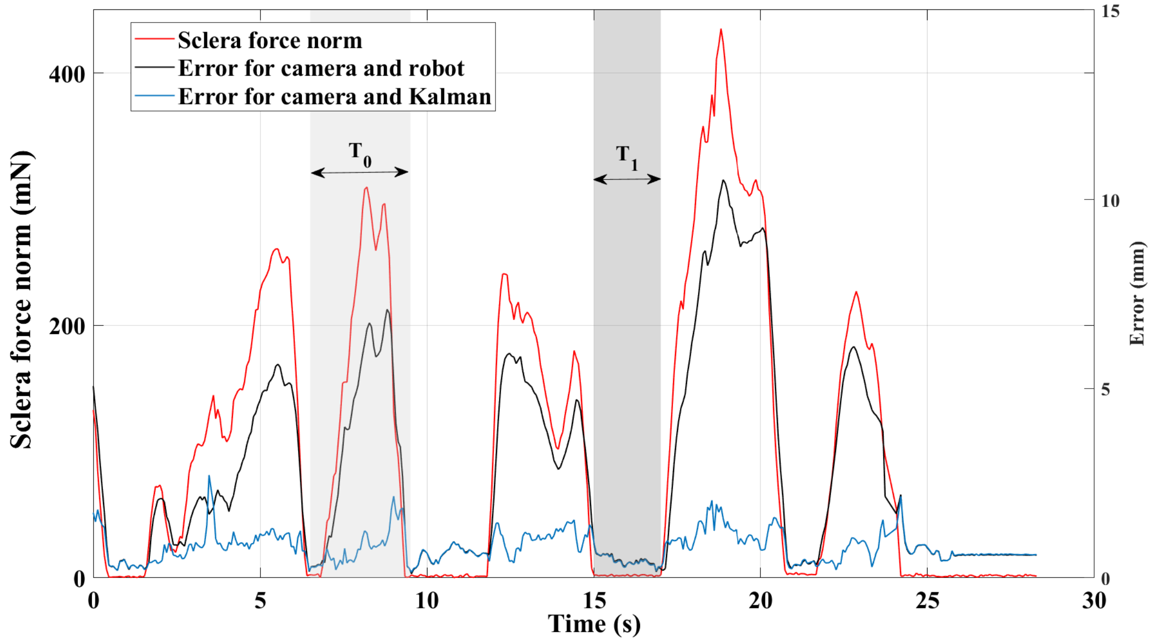

Figure 3.11: Error variations for the dynamic experiment. Sclera forces (left y axis) and the KF and FWK errors for tool tip position (right y axis).

Table 3.1: Errors for the validation experiments and the case study.

Experiment	Signal	Total Error (mm)	Error over T_0 (mm)	Error over T_1 (mm)
Insertion depth experiments	Kalman output	0.20	0.21	0.17
	FBG measurement	3.14	4.26	0.18
Tip position experiments	Kalman output	0.81	1.53	0.57
	Forward Kinematics	2.30	6.42	0.59
Case study	Kalman output	0.78	1.01	0.44
	Forward Kinematics	2.76	4.38	0.43

3.8 Discussion and Conclusion

To address the limitations that we encountered in Chapter 2 for FBG-based insertion depth measurements and to further extend robot sensing capabilities of the system states, in this chapter we have presented a novel method to simultaneously improve the tool tip position and insertion depth measurements during robot-assisted retinal surgery. The measurements were based solely on the existing FBG sensors and the robot kinematics which were combined using KF. As it can be seen from Fig. 3.5, the FBG sensors are not able to provide reliable insertion depth measurements and as soon as sclera forces approach zero the FBG measurement for insertion depth does not change and becomes a fixed line. In addition, by investigating Fig. 3.6 and also comparing it to Fig. 3.5, it can be observed that the error for FBG-based insertion depth measurements becomes larger and noisier when then sclera force is diminishing (for instance when sclera force is less than $40\ mN$ around $t = 2\ s$ in Fig. 3.6). This justifies why the covariance value for w^d was chosen as a large number when the sclera force is less than $50\ mN$. However, the KF is able to precisely keep track of the insertion depth. In Table 3.1, the mean value of insertion depth estimation error over the T_0 intervals of Fig. 3.5 are reported as $0.21\ mm$ and $4.26\ mm$ for the KF and FBG-only approaches, respectively, thus, indicating a significant improvement in insertion depth measurements using KF. In the case study, Table 3.1 shows that the tool tip position estimation error has been improved to $1.01\ mm$. Although this accuracy is less than tens of microns and hundreds of microns precision using OCT-based and vision-based methods as reported in [103] and [98], our approach lacks the limitations of [103] and [98] as described in detail in Section 3.1.

There are six bumps visible in Figs. 3.7 and 3.8 indicating the tool deflections that were manually imposed on the tool shaft. Fig. 3.8 shows large errors (up to $13\ mm$ around $t = 42\ s$) in the FWK estimations when tool deflection occurs. Fig. 3.7 indicates that the KF estimations are able to follow the camera output when deflections (bumps) occur. Table 3.1 indicates that during T_0 time intervals in Fig. 3.8, the average error for the KF and FWK approaches are $1.53\ mm$ and $6.42\ mm$, respectively, demonstrating a 76% improvement in tool tip position estimation using KF.

In the case study experiment, the user followed the phantom vessels with the tool tip. For better clarification, a sample of T_0 and T_1 intervals are shaded in Figs. 3.10, 3.9 and 3.11. Comparing the shaded T_0 and T_1 intervals in Figs. 3.10, we can realize that in T_0 intervals the FBG measurements are not reliable, and they return constant unchanging values similar to what was explained in Fig. 3.5, while the KF estimations are reflecting the changes correctly. In Figs. 3.9 and 3.11 a similar behavior occurs during the T_0 interval for the tool tip positioning estimation. In the shaded T_0 interval, the FWK is not able to provide a good estimation of the tool tip position because the tool is deflected. However, the KF results in correct values even in areas where tool deflection is present. This observation is further supported by comparing the average tool tip position estimation errors for the KF and FWK during the case study experiment. The average error is reduced from $4.38\ mm$ to $1.01\ mm$, which again indicated a 77% improvement for the tool tip position estimation.

In conclusion, this chapter introduced a force-based estimation method that can improve simultaneous insertion depth and tool tip position estimations in robot-assisted retinal surgery. Of note, such information is valuable and critical for safety enhancement and more accurate feedback in semi-autonomous robot-assisted tasks in eye surgery. The introduced method showed significant improvements in the associated estimations for insertion depth and tool tip position.

3.9 Publications

Journal Publications:

- **Ali Ebrahimi**, Farshid Alambeigi, Shahriar Sefati, Niravkumar Patel, Changyan He, Peter Gehlbach, and Iulian Iordachita, *"Stochastic Force-based Insertion Depth and Tip Position Estimations of Flexible FBG-Equipped Instruments in Robotic Retinal Surgery"*, in IEEE/ASME Transactions on Mechatronics (TMECH), vol. 26, no. 3, pp. 1512-1523, June 2021.

Conference Publications:

- **Ali Ebrahimi**, Muller Urias, Niravkumar Patel, Peter Gehlbach, Farshid Alambeigi, and Iulian Iordachita, *"FBG-based Kalman Filtering and Control of Tool Insertion Depth For Safe Robot-assisted Vitrectomy"*, In 2020 International Symposium on Medical Robotics (ISMR) (pp. 146-151). IEEE.

3.10 Publications Contribution

In the publications lists in Section 3.9, the co-authors contributed as follows:

Niravkumar Patel helped in the experimental setup development and software implementation and debugging related to the control methods.

Changyan He helped with development of FBG-equipped surgical instrument and the experimental setup.

Farshid Alameigi helped with advising on different sections of the paper and data analysis.

Muller Urias helped with conducting mock vitrectomy experiments and advised on the clinical aspects of the work.

Shahriar Sefati developed the stereo camera system and calibrated it for conducting the experiments.

Chapter 4

Registration and Calibration Independent Algorithm for Deformable Needle Tip Localization in Robotic Eye Surgery

4.1 Background and Motivation

In Chapter 3, a force-based framework for simultaneous improvement of insertion depth measurement and deflected needle tip position estimation was developed and evaluated. Although this approach does not have the restrictions of vision-based methods, which were pointed out in Section 3.1, it requires that the mechanical properties (e.g. stiffness) of surgical instruments be identified through pre-operative calibration experiments (Section 3.6.1). Such pre-operative property identification is prone to inaccuracies as the properties may change during the course of surgery. In addition, the pre-operative calibration procedures are time-consuming and if required for every single instrument used in the surgery. Consequently, such parameters could be determined by online identification methods (e.g. adaptive parameter estimation). Such methods have been previously employed for other applications such as parameter identification for force control during needle insertion [127–130].

Another limitation of pure vision-based methods for instrument tip localization is the fact that a pre-operative frame registration between the robot base frame and the visual modality (e.g. stereo microscope, OCT) frame is required. All of the vision-based studies for instrument tip localization mentioned in Section 3.1, such as the OCT-based methods [100–103] as well as studies dependent on stereoscopic microscope [90, 98, 111, 112, 120], rely on the camera-to-robot frame transformation. Repeated intra-operative registrations is required if microscope movement occurs. This often happens during a typical ophthalmic surgical procedure as the surgeons need to adjust the microscope height to obtain the desired view inside of the eye.

To address the challenges of estimating the deflected instrument tip position during robot-assisted eye surgery, we have devised a novel framework that combines force- and vision-based methods in an efficient way. The developed method is independent of any pre-operative instrument calibration (Section 3.6.1) or registration between the robot arm and the visual modality coordinate frames. By this method, it is possible to estimate the deflected instrument tip position without any pre-operative information about the needle stiffness or the camera-to-robot frame transformation.

4.2 Contribution

This chapter reports how we have built upon the KF-based framework for estimation of tool tip position, which was developed in Chapter 3 to obtain a novel registration and calibration independent method for instrument tip position localization.

In this framework, we estimate and update the surgical instrument stiffness (the parameter $3EI$ required in (3.5)) intra-operatively using an adaptive identification algorithm. A Lyapunov-based proof is provided to demonstrate that the adaptive stiffness estimation exponentially converges to its true value. As an alternative to the adaptive approach, we also develop a least squares version of the identification algorithm, which does not require a continuous update of the instrument stiffness. The developed algorithms use the stereoscopic camera for online instrument stiffness estimation. Although this online estimation of the instrument stiffness is vision-based, which may seem to require the registration between the camera and the robot frame, the online identification algorithm has been rendered independent of it (registration-independent).

This stiffness estimation is then combined with the state-space model for instrument tip position evolution, previously developed in Chapter 3, to estimate the deflected instrument tip position through a KF-based approach. Therefore, the contributions of this chapter are as follows:

1. Develop a least squares and an adaptive based framework for online estimations of instrument shaft stiffness using FWK, FBG measurements for sclera force and insertion depth, and a visual modality (e.g. stereoscopic camera) as input information.

2. Make the stiffness estimation formulation independent of the registration between the visual modality and the robot base frame.

3. Simultaneous registration-independent stiffness estimation and a KF-based vision-independent improvement of the tip position estimation of

the instrument when undergoing deflections.

The entire framework is then evaluated using the SHER and a FBG-equipped instrument during similar experimental conditions explained in Chapter 3. Of note, the method can potentially function despite intermittent loss of the visual modality, e.g. when the instrument tip is hidden by eye anatomy. The reason is that we can utilize the prior estimations of instrument stiffness (when it was visible in the camera) during brief periods of loss of visibility.

4.3 Online Identification of Instrument Stiffness

A schematic of the system is provided in Fig. 4.1. There are three coordinate frames of interest in the following formulations as depicted in Fig. 4.1:

1. Robot base frame $\{B\}$ which is fixed with coordinate axis $[X^b, Y^b, Z^b]$.
2. Robot tip frame $\{E\}$ which is attached at the tip of the imaginary not-deflected instrument and is moving in the space with coordinate axis $[X^e, Y^e, Z^e]$.
3. Camera frame $\{C\}$ which is fixed with coordinate axis $[X^c, Y^c, Z^c]$.

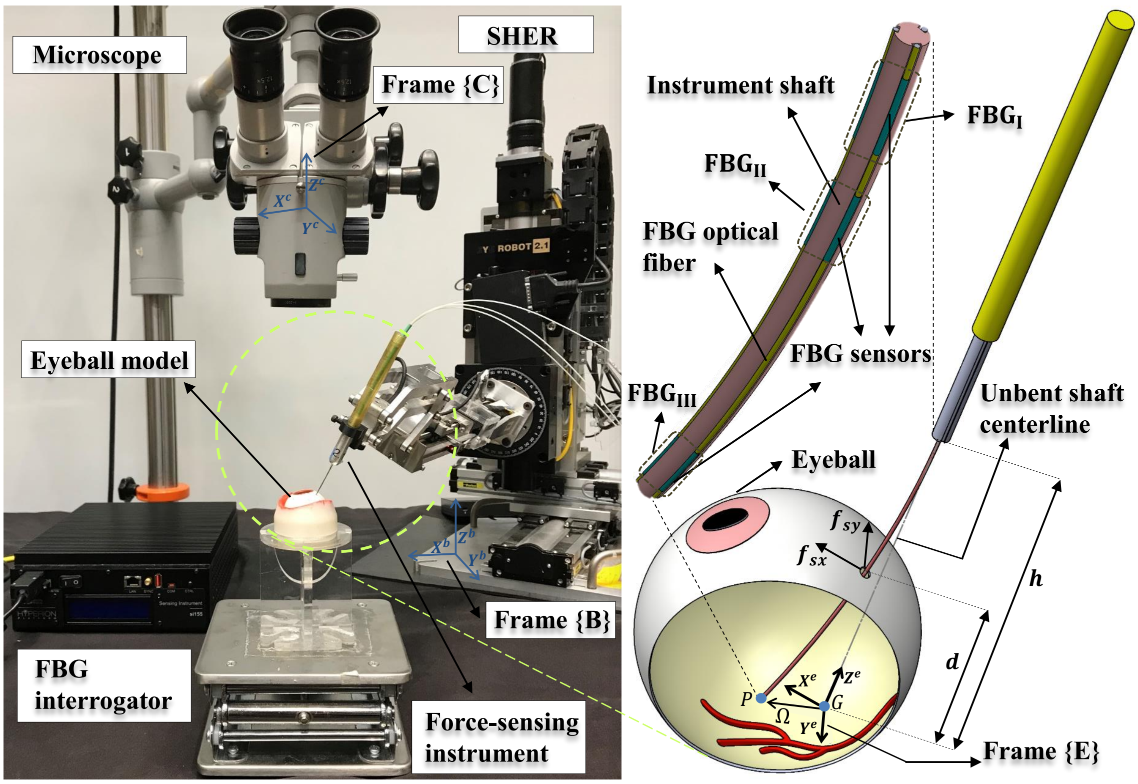

Figure 4.1: Eye phantom manipulation with the SHER – the surgeon grabs the force-sensing tool which is attached to the robot to manipulate the eye phantom.

As it was also discussed in Chapter 3, the surgical instrument shown in Fig. 4.1 is often bent when it is in contact with the sclera tissue during surgery, which was modeled as a cantilever beam in (3.5). The instrument tip deflection vector denoted by Ω, which is shown in Fig. 4.1, has δ_x and δ_y components along X^e and Y^e, respectively (provided in (3.5)). We assume that the instrument tip movement along Z^t is negligible when it undergoes deflection, hence the z coordinate of the tool tip is always zero in frame $\{E\}$. Due to the low amount of friction between the tool shaft and sclera, we assume that the sclera force component along Z_e is also zero. Therefore, the vectors of tool tip position and the sclera force in frame $\{E\}$ can be written as follows:

$$\begin{aligned} \Omega &= [\delta_x, \delta_y, 0]^T \\ F_s &= [f_{sx}, f_{sy}, 0]^T \end{aligned} \tag{4.1}$$

In order to continue the formulation for online identification for instrument stiffness, we are going to rewrite (3.9). As it was mentioned under (3.9), β_z could be chosen arbitrarily due to the assumptions we made for the sclera forces and deflection along the z direction of frame $\{E\}$. Without loss of generality, we can assume β_z is equal to β_x and β_y, which is $\frac{(h-d)^3}{3EI} + \frac{(h-d)^2}{2EI}d$ based on (3.6). Based on (3.6), β_i was the variable relating the ith component of sclera force to its corresponding deflection. If we call this common value β then the matrix Γ in (3.9) will be reduced to scalar β^{-1}. Now (3.9) can be written in the simpler following format:

$$\Omega = \mathbf{R}_{be}^T(P - S_{be}) = \beta F_s \tag{4.2}$$

where P is the instrument tip position in frame $\{B\}$, and $\mathbf{R}_{be}$ and S_{be} are the rotational and translational componetns of the frame transformations between frames $\{B\}$ and $\{E\}$. Using this notation, the state space model for tool tip position which was given in (3.11), can be written as follows where the matrix

Γ is substituted with scalar $\frac{1}{\beta}$.

$$\begin{aligned} P_k &= P_{k-1} + [\mathbf{J}_{tip}\dot{Q}]_{k-1}(t_k - t_{k-1}) + W^P_{k-1} \\ Y^P_k &= \underbrace{[\frac{1}{\beta}\mathbf{R}^T_{be}]_k}_{\mathbf{H}_k} P_k + V^P_k \end{aligned} \tag{4.3}$$

Furthermore, we identified the combination of mechanical properties ($3EI$) of the instrument in Section 3.6.1 using offline data. In this chapter θ denotes the inverse of this stiffness quantity, $\theta = \frac{1}{3EI}$. Using this definition, the scalar β can be written as following:

$$\beta = \theta(h-d)^3 + 1.5\theta(h-d)^2 d \tag{4.4}$$

where h is the length of the needle and d is the instrument insertion depth as shown in Fig. 4.1. If we plug (4.4) into (4.2) and factor θ out and call the rest of variables U, we can obtain the following vector equation:

$$\Omega = \theta \underbrace{(F_s(h-d)^3 + 1.5F_s(h-d)^2 d)}_{U(t)} = \theta U(t) \tag{4.5}$$

The big parenthesis term in the right-hand side of (4.5) is an explicit function of time, because d is the output of the KF estimation in (3.13), the components of sclera force vector F_s are directly measured by the FBG sensors in real time, and other parameters are constant. We, therefore, can denote this term with $U(t) \in \mathbb{R}^3$. Taking the 2-norm of both sides of (4.5) yields:

$$||\Omega||_2 = \theta ||U(t)||_2 \tag{4.6}$$

The calibration procedure performed in 3.6.1 is time-consuming and should be carried out for each instrument prior to the surgery. To mitigate these problems, we now intend to integrate two online estimation methods for θ into the KF framework developed in Section 3.4: 1) least squares identification and 2) adaptive identification. Both stiffness estimation methods are vision-based, which is appropriate for an eye surgery procedure because in a typical ophthalmic procedure visualization of the instrument tip is usually available and critical to completing the procedure safely. This removes the need for any preoperative calibration to determine θ prior to the surgery.

4.3.1 Least Squares Identification

The $3D$ coordinate of the tip position of an imaginary straight (not-deflected) instrument is represented by $G \in \mathbb{R}^3$ (Fig .4.1). Based on Fig. 4.1, one can write the following equations for Ω:

$$\begin{aligned} \Omega_b &= P_b - G_b = (\mathbf{R}_{bc} P_c + S_{bc}) - G_b \\ ||\Omega||_2 &= ||(\mathbf{R}_{bc} P_c + S_{bc}) - G_b||_2 \end{aligned} \tag{4.7}$$

where the subscripts for P, G, and Ω indicate the coordinate frame in which they are written (b for frame $\{B\}$ and c for frame $\{C\}$). In (4.7), $\mathbf{R}_{bc}$ and S_{bc} are the rotation and translation components of the homogeneous transformation between frames $\{B\}$ and $\{C\}$ which is:

$$\mathbf{F}_{bc} = \begin{pmatrix} \mathbf{R}_{bc} & S_{bc} \\ \mathbf{0}_{1\times 3} & 1 \end{pmatrix} \tag{4.8}$$

The experimental process of finding $\mathbf{R}_{bc}$ and S_{bc} were elaborated in Section 3.5.2. In (4.7), P_b is not directly measurable, and the only source for the direct measurement of P is the stereo camera system (P_c) using an image segmentation approach. Using the robot FWK, we can always have the coordinate vector G in frame $\{B\}$, which is denoted by G_b in (4.7). Thus, the second equation in (4.7) that contains known values can be used to collect samples for $||\Omega||_2$ which will be required in online stiffness identification process.

After collecting m corresponding samples of $||\Omega||_2$ based on (4.7) and $||U||_2$ based on (4.5) intraoperatively during the surgery, we can construct vectors of the collected samples as follows:

$$\begin{aligned} \Gamma &= [||\Omega_1||_2, ..., ||\Omega_m||_2]^T \\ \Upsilon &= [||U_1||_2, ..., ||U_m||_2]^T \end{aligned} \tag{4.9}$$

Using these vectors, we can obtain the least squares estimation of θ , called

$\hat{\theta}_{lsq}$:

$$\hat{\theta}_{lsq} = \min_{\theta} ||\Gamma - \theta\Upsilon||_2 = (\Upsilon^T\Upsilon)^{-1}\Upsilon^T\Gamma \tag{4.10}$$

Once found, $\hat{\theta}_{lsq}$ can be used in β in (4.4) which is then used in the state-space model (4.3) for further KF calculations. During a surgery, the least squares identification can be done in the first few seconds of the surgery while the needle tip position is visible in the microscope view. Then, it can be used when the tool tip is not visualized.

4.3.2 Adaptive Identification

The instrument is not a perfect cantilever beam and slightly different values of $\hat{\theta}_{lsq}$ may be obtained depending on what section of the needle is used for the least squares data collection. This motivates the use of an adaptive identification method where the parameter θ is continuously updated during the surgery based on the section of the needle shaft that is in contact with the sclera entry point. Considering (4.6), we use the following estimate model for θ:

$$||\hat{\Omega}(t)||_2 = \hat{\theta}(t)||U(t)||_2 \tag{4.11}$$

where $\hat{\theta}$ is the estimate for θ and $||\hat{\Omega}(t)||_2$ is the estimated magnitude for tool tip deflection. As indicated in (4.11), $||\hat{\Omega}||_2$, $\hat{\theta}$ and $||U||_2$ are functions of time, but for notation simplicity we drop t in the following calculations. We use the following adaptation law for updating $\hat{\theta}$, which is basically a differential equation that governs the evolution of $\hat{\theta}$:

$$\dot{\hat{\theta}} = -\gamma ||U||_2(||\hat{\Omega}||_2 - ||\Omega||_2) = -\gamma ||U||_2 \Delta ||\Omega||_2 \tag{4.12}$$

where γ is a positive constant, $\Delta ||\Omega||_2$ is the difference between the estimated and actual values for the magnitude of the instrument tip deflection, and $\dot{\hat{\theta}}$ is the time derivative of $\hat{\theta}$. Substituting $||\hat{\Omega}||_2$ in (4.12) using (4.11):

$$\dot{\hat{\theta}} = -\gamma ||U||_2(\hat{\theta}||U||_2 - ||\Omega||_2) \tag{4.13}$$

which can be rewritten using (4.6) as follows:

$$\dot{\hat{\theta}} = -\gamma ||U||_2(\hat{\theta}||U||_2 - \theta ||U||_2) = -\gamma ||U||_2^2 \Delta\theta \tag{4.14}$$

where $\Delta\theta = \hat{\theta} - \theta$ is the error for adaptive estimation of θ.

- **Proposition:** The adaptation law (4.14) makes the adaptive estimation $\hat{\theta}$ bounded. Furthermore, if $\exists\ \epsilon > 0$ and $T > 0$ such that $\forall\, t$, the vector $U(t)$ satisfies the following equation:

$$\int_t^{t+T} ||U(\tau)||_2^2 d\tau \geq \epsilon T \tag{4.15}$$

then and the adaptive estimation error $\Delta\theta$ exponentially converges to zero. $||U||_2$ is said to be persistently excited when it satisfies (4.15).

Proof: To show that $\hat{\theta}$ is bounded, we use the following Lyapunov function:

$$V = \frac{1}{2}\Delta\theta^2 \tag{4.16}$$

Taking the derivative of both sides of (4.16) with respect to t we get:

$$\dot{V} = \Delta\dot{\theta}\Delta\theta = \dot{\hat{\theta}}\Delta\theta \tag{4.17}$$

Because we assume θ is approximately constant along the needle shaft ($\dot{\theta} \simeq 0$), $\Delta\dot{\theta} = \dot{\hat{\theta}} - \dot{\theta} = \dot{\hat{\theta}}$ as it is written in (4.17). Substituting $\dot{\hat{\theta}}$ from (4.14) in (4.17):

$$\dot{V} = -\gamma||U||_2^2\Delta\theta^2 \leq 0 \tag{4.18}$$

meaning that $\dot{V}$ is semi negative definite. This indicates that V is a descending function, i.e. $V(t) \leq V(0)$. On the other hand based on (4.16), V is semi positive definite, that is $0 \leq V(t) = \frac{1}{2}\Delta\theta^2 \leq V(0)$. This indicates that $0 \leq |\Delta\theta(t)| \leq \sqrt{2V(0)}$ meaning that $|\Delta\theta|$ is a bounded function of time. Because $|\Delta\theta| = |\hat{\theta} - \theta|$ and θ is approximately a fixed value, this results in the boundedness of $\hat{\theta}$.

To show that $\Delta\theta$ has exponential convergence to zero we use (4.15). Because (4.15) is valid for all values of t, if we substitute t in (4.15) with $t+(i-1)T$ where

i is a positive integer we find that $\forall\, i$:

$$\int_{t+(i-1)T}^{t+iT} ||U(\tau)||_2^2 d\tau \geq \epsilon T \tag{4.19}$$

Summing both sides of (4.19) from 1 to n we get:

$$\sum_{i=1}^{n} \int_{t+(i-1)T}^{t+iT} ||U(\tau)||_2^2 d\tau \geq n\epsilon T \tag{4.20}$$

if we perform the above summation we will obtain $\forall\, n \in \mathbb{Z}^+$:

$$\int_{t}^{t+nT} ||U(\tau)||_2^2 d\tau \geq n\epsilon T \tag{4.21}$$

which for $t = 0$ becomes:

$$\int_{0}^{nT} ||U(\tau)||_2^2 d\tau \geq n\epsilon T \tag{4.22}$$

Because $\Delta\dot{\theta} = \dot{\hat{\theta}}$, we can rewrite (4.14) as follows:

$$\Delta\dot{\theta} = -\gamma ||U||_2^2 \Delta\theta \tag{4.23}$$

The solution to the above differential equation is:

$$|\Delta\theta(t)| = |\Delta\theta(0)| exp(-\int_0^t \gamma ||U(\tau)||_2^2 d\tau) \tag{4.24}$$

where $\Delta\theta(0)$ is the estimation error at $t = 0$. Without loss of generality we can assume $nT \leq t \leq (n+1)T$. Using the inequality, (4.24) can be rewritten as follows:

$$|\Delta\theta(t)| \leq |\Delta\theta(0)|exp(-\int_0^{nT} \gamma||U(\tau)||_2^2 d\tau) \tag{4.25}$$

If we use (4.22), the above inequality can be written as:

$$|\Delta\theta(t)| \leq |\Delta\theta(0)|exp(-\gamma n\epsilon T) \tag{4.26}$$

In order to make the inequality (4.26) independent of n we add and subtract T and rewrite (4.26) as follows:

$$\begin{aligned} |\Delta\theta(t)| \leq & |\Delta\theta(0)|exp(-\gamma(n\epsilon T + T - T)) = \\ & |\Delta\theta(0)|exp(\gamma T)exp(-\gamma\epsilon(n+1)T) \leq \\ & |\Delta\theta(0)|exp(\gamma T)exp(-\gamma\epsilon t) \end{aligned} \tag{4.27}$$

where the last inequality in (4.27) is because $t \leq (n+1)T$. The right-hand side of (4.27) can be written as follows:

$$|\Delta\theta(t)| \leq \underbrace{|\Delta\theta(0)|exp(\gamma T)}_{S} exp(-\overbrace{\gamma\epsilon}^{b} t) \tag{4.28}$$

Because S and b are positive constants, we have shown that $\forall t$ $|\Delta\theta(t)| \leq$

$Sexp(-bt)$ which is equivalent to the exponential convergence of $\Delta\theta(t)$ and as $t \to \infty$, $\Delta\theta(t)$ exponentially converges to zero.

The physical interpretation of (4.15), which is called persistent excitation of $||U||_2$, is that $||U||_2$ should not decay to zero. Based on (4.5), $||U||_2$ is $||F(h-d)^3 + 1.5F(h-d)^2 d||_2$. Considering d is a positive constant which is always less than h ($d \geq 0$ and $h - d \geq 0$), this signal is excited whenever F_s is not zero, i.e. when the tool is deflected. In other words, we expect the estimate $\hat{\theta}$ to converge to the local stiffness of the instrument at the point of contact as soon as the sclera forces are exerted on the instrument shaft and the instrument is deflected.

4.4 Registration Independent Framework

In order to measure $||\Omega||_2$ based on (4.7), which is needed for both least squares and adaptive identification methods, the components of the rigid body transformation $\mathbf{F}_{bc}$ are required. This is a big issue for the online estimation methods, because this transformation should be obtained prior to the surgery and not vary during the surgery, i.e. the camera should not move relative to the robot. This was one of the limitations associated with all of the vision-based approaches for tool tip localization as delineated in Section 4.1.

Although it is less difficult to obtain $\mathbf{F}_{bc}$ prior to the surgery than to calibrate each surgical instrument to find their associated θ_{off}, it would be much more convenient to make the online estimations independent of $\mathbf{F}_{bc}$. This problem is further exacerbated by noting that during ophthalmic surgery the surgeon often moves the microscope to maintain the operative field or to focus, which requires finding $\mathbf{F}_{bc}$ after each movement (even if small) of the surgical microscope.

Because both online identification methods rely on the scalar equation (4.6) which contains $||\Omega||_2$, the idea would be to attain another scalar equation similar to (4.6) but independent of any component of $\mathbf{F}_{bc}$. Then this new scalar equation can be used for the least squares or the adaptive approach similar to how (4.6) was used. The general idea behind the developed RI algorithm is to find θ by looking at the changes of the deflection vector Ω in different sample times rather than its absolute value. In other words, although calculating the absolute value of Ω is dependent on $\mathbf{F}_{be}$, the differences between consecutive values of Ω can be made independent of $\mathbf{F}_{be}$. This can be obtained by rewriting (4.5) in an iterative fashion. The new scalar equation demonstrates the relationship between θ, the changes of the tip position in the camera frame (independent of $\mathbf{F}_{bc}$), and the variations of sclera forces. Therefore, to develop the RI formulation we try to manipulate (4.5) prior to directly taking the norm of (4.5) which leads to (4.6). Of note, (4.5) is a vector equation that can be expressed in any coordinate frame. We first rewrite this equation in the frame $\{E\}$. The advantage of selecting this coordinate frame is that the imaginary undeflected tool tip position will have zero coordinate components ($G_e = [0,0,0]^T$) in the frame $\{E\}$.

$$\Omega_e = \theta U_e \tag{4.29}$$

Considering the points P and G, the left-hand side of (4.29) can be written as follows:

$$\Omega_e = P_e - G_e = \mathbf{R}_{ec} P_c + S_{ec} - G_e = \mathbf{R}_{ec} P_c + S_{ec} \tag{4.30}$$

where G_e is dropped because it is a zero vector. In (4.30), $\mathbf{R}_{ec}$ and S_{ec} are the rotation and translation components of the frame transformation $\mathbf{F}_{ec}$. In order to exploit the known transformation between the frames $\{E\}$ and $\{B\}$ ($\mathbf{F}_{be}$) provided by the FWK, we express $\mathbf{F}_{ec}$ as $\mathbf{F}_{eb}\mathbf{F}_{bc}$

$$\begin{aligned} \mathbf{F}_{ec} =& \mathbf{F}_{eb}\mathbf{F}_{bc} = \begin{pmatrix} \mathbf{R}_{eb} & S_{eb} \\ \mathbf{0}_{1\times 3} & 1 \end{pmatrix} \begin{pmatrix} \mathbf{R}_{bc} & S_{bc} \\ \mathbf{0}_{1\times 3} & 1 \end{pmatrix} = \\ & \begin{pmatrix} \mathbf{R}_{eb}\mathbf{R}_{bc} & \mathbf{R}_{eb} S_{bc} + S_{eb} \\ \mathbf{0}_{1\times 3} & 1 \end{pmatrix} = \begin{pmatrix} \mathbf{R}_{ec} & S_{ec} \\ \mathbf{0}_{1\times 3} & 1 \end{pmatrix} \end{aligned} \tag{4.31}$$

Based on (4.31), we can obtain the following results:

$$\begin{aligned} \mathbf{R}_{ec} &= \mathbf{R}_{eb}\mathbf{R}_{bc} \\ S_{ec} &= \mathbf{R}_{eb}S_{bc} + S_{eb} \end{aligned} \tag{4.32}$$

where $\mathbf{R}_{eb} = \mathbf{R}_{be}^T$ and $S_{eb} = -\mathbf{R}_{be}^T S_{be}$. Substituting $\mathbf{R}_{ec}$ and S_{ec} in (4.30) from (4.32) one can write:

$$\mathbf{R}_{eb}\mathbf{R}_{bc}P_c + \mathbf{R}_{eb}S_{bc} + S_{eb} = \theta U_e \tag{4.33}$$

If we write (4.33) in an iterative way for two different sample times i and j we get:

$$\begin{aligned} \mathbf{R}_{eb_i}\mathbf{R}_{bc}P_{c_i} + \mathbf{R}_{eb_i}S_{bc} + S_{eb_i} &= \theta U_{e_i} \\ \mathbf{R}_{eb_j}\mathbf{R}_{bc}P_{c_j} + \mathbf{R}_{eb_j}S_{bc} + S_{eb_j} &= \theta U_{e_j} \end{aligned} \tag{4.34}$$

We multiply the first equation in (4.34) by $\mathbf{R}_{eb_i}^T$ and the second equation by $\mathbf{R}_{eb_j}^T$ both of which are known matrices from the robot FWK. Also considering that rotation matrices are orthogonal, i.e. $\mathbf{R}_{eb_i}^T\mathbf{R}_{eb_i} = I$ and $\mathbf{R}_{eb_j}^T\mathbf{R}_{eb_j} = I$ we get:

$$\begin{aligned} \mathbf{R}_{bc}P_{c_i} + S_{bc} + \mathbf{R}_{eb_i}^T S_{eb_i} &= \theta\mathbf{R}_{eb_i}^T U_{e_i} \\ \mathbf{R}_{bc}P_{c_j} + S_{bc} + \mathbf{R}_{eb_j}^T S_{eb_j} &= \theta\mathbf{R}_{eb_j}^T U_{e_j} \end{aligned} \tag{4.35}$$

Now if we subtract the second equation from the first one in (4.35), the unknown term S_{bc} disappears:

$$\mathbf{R}_{bc}(P_{c_j} - P_{c_i}) + \mathbf{R}_{eb_j}^T S_{eb_j} - \mathbf{R}_{eb_i}^T S_{eb_i} = \theta(\mathbf{R}_{eb_j}^T U_{e_j} - \mathbf{R}_{eb_i}^T U_{e_i}) \tag{4.36}$$

In order to omit $\mathbf{R}_{bc}$ in (4.36), we write it as follows:

$$\mathbf{R}_{bc}(P_{c_j} - P_{c_i}) = \theta(\mathbf{R}_{eb_j}^T U_{e_j} - \mathbf{R}_{eb_i}^T U_{e_i}) - (\mathbf{R}_{eb_j}^T S_{eb_j} - \mathbf{R}_{eb_i}^T S_{eb_i}) \tag{4.37}$$

Because rotation matrices preserve the norm, we can write the following equation for $\mathbf{R}_{bc}$:

$$||\mathbf{R}_{bc}(P_{c_j} - P_{c_i})||_2 = ||(P_{c_j} - P_{c_i})||_2 \tag{4.38}$$

If we use (4.38) and take the 2-norm of both sides of (4.37), $\mathbf{R}_{bc}$ vanishes, and we can write:

$$\begin{aligned} &||(P_{c_j} - P_{c_i})||_2 = \\ &||\theta \underbrace{(\mathbf{R}_{eb_j}^T U_{e_j} - \mathbf{R}_{eb_i}^T U_{e_i})}_{V_1} - \underbrace{(\mathbf{R}_{eb_j}^T S_{eb_j} - \mathbf{R}_{eb_i}^T S_{eb_i})}_{V_2} ||_2 \end{aligned} \tag{4.39}$$

Squaring both sides of (4.39), we get:

$$\theta^2 ||V_1||_2^2 - 2\theta V_1^T V_2 + ||V_2||_2^2 - ||(P_{c_j} - P_{c_i})||_2^2 = 0 \tag{4.40}$$

The above equation is a second order equation in θ which is independent of any component of $\mathbf{F}_{bc}$. We can solve for θ as follows:

$$\theta = \frac{V_1^T V_2 \pm \sqrt{(V_1^T V_2)^2 - ||V_1||_2^2(||V_2||_2^2 - ||(P_{c_j} - P_{c_i})||_2^2)}}{||V_1||_2^2} \tag{4.41}$$

It is noted that among the two solutions of (4.41), the second one (minus sign in $\pm$) will be ruled out because if $||(P_{c_j} - P_{c_i})||_2$ is larger than $||V_2||_2$, then the radicand will be larger than $(V_1^T V_2)^2$ leading to negative values of θ. For this reason, the positive sign in $\pm$ is selected for the RI methods. In (4.41), if we denote the numerator A and the denominator B, we can write the following scalar equation which can be used instead of (4.6) to identify θ using the least squares or the adaptive method.

$$B\theta = A \tag{4.42}$$

In (4.42), A and B are known signals and the advantage of using (4.42) over (4.6) is that it is independent of the components of the transformation $\mathbf{F}_{bc}$ (registration between the camera and the robot base frame). It is noted that for B in (4.42) to satisfy the persistent excitation condition for the adaptive identification method, $||V_1||_2$ should be non-zero. This means that U_{e_i} should be different from U_{e_j}. By looking at the definition of U in (4.5), this condition indicates that the sclera forces and insertion depth should not remain constant over a time interval to have the convergence of θ. A block diagram representing how the framework works and what signals are required for each part, is provided in Fig. 4.2.

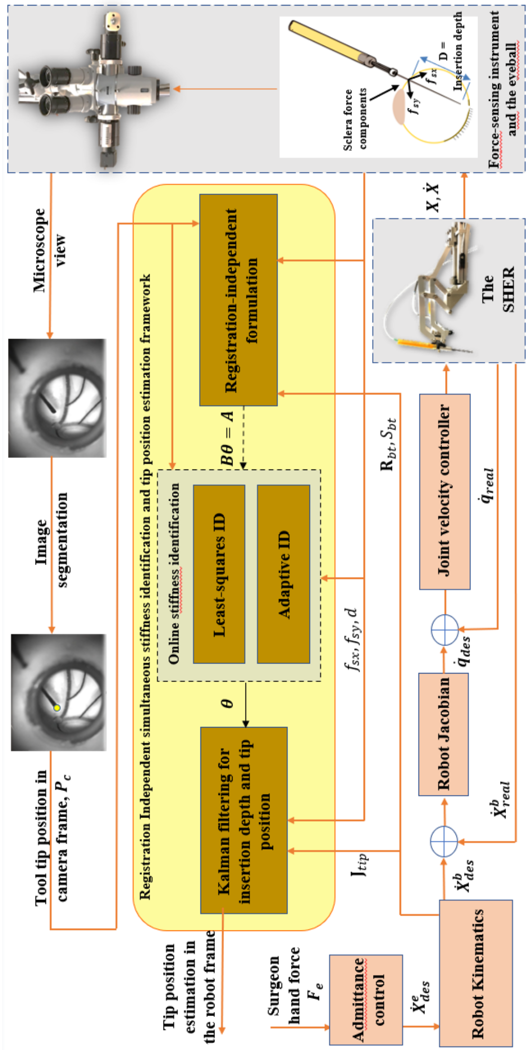

Figure 4.2: Block diagram for the instrument tip position estimation. The yellow highlighted part represents the combination of registration-independent online stiffness identification with the KF framework. The outer part shows how the robot FWK and the visual modality information are communicated with the tip position estimation framework. The signals $\dot{X}^e_{des}$ and $\dot{X}^b_{des}$ are the desired velocity of the robot end-effector expressed in frames $\{E\}$ and $\{B\}$, respectively. $\dot{X}^b_{real}$ denotes the real velocity of the robot end-effector in frame $\{B\}$. Variables $\dot{q}_{des}$ and $\dot{q}_{real}$ indicate the desired and real joint velocities of the robot.

4.5 Experimental Procedure

We conducted two sets of experiments (static and dynamic) similar to those explained in Section 3.6 in order to evaluate the combination of online estimations of θ and KF for tool tip position estimation and to assess the performance of the registration-independent approach. In each experiment set (static or dynamic), both of the adaptive identification AD and the least squares identification LSQ approaches as well as their registration independent (RI) version, respectively RIAD (registration independent adaptive) and RILSQ (registration independent least squares), were investigated. In all experiments the KF estimation for tool tip position with online and offline estimations of θ were obtained and compared to that of the robot FWK and the stereo camera observation, which is the ground truth.

4.6 Results

For the force-sensing instrument used in these experiments, the offline preoperative estimation of the instrument stiffness, θ_{off} was obtained in Section 3.6.1. Based on Fig. 3.4 the value for $\theta_{off}^{-1} = 3EI$ was $3.39 \times 10^6 mN.mm^2$.

Next, the results for the static and dynamic experiments for KF-based instrument tip position localization combined with each of the four online stiffness estimation methods, namely AD, LSQ, RIAD, RILSQ are presented.

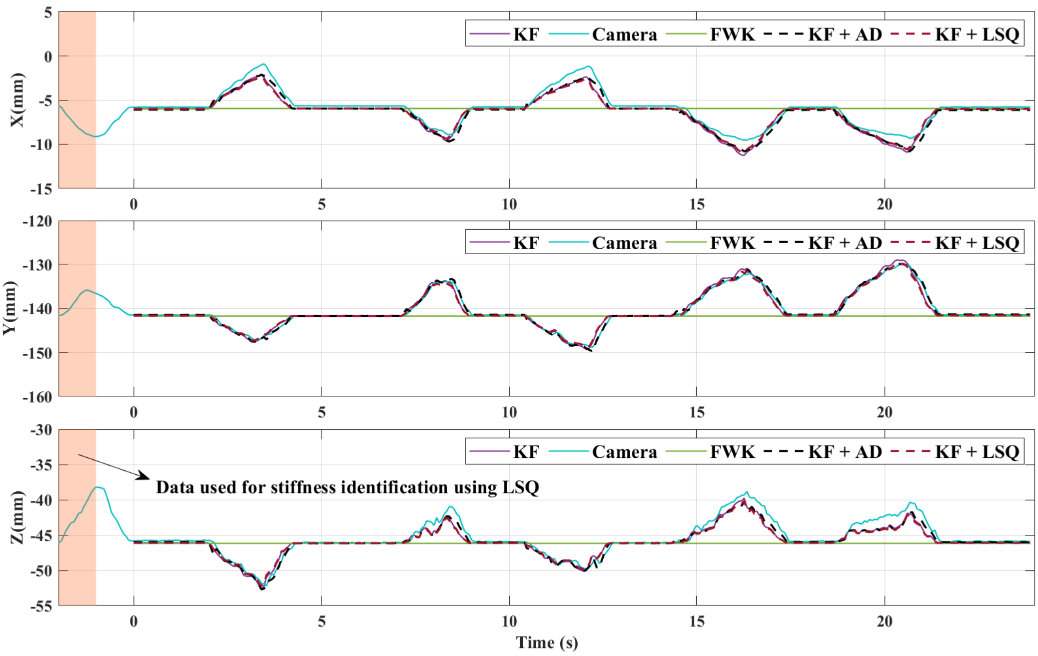

Figure 4.3: Tool tip coordinate positions in frame $\{B\}$ during static experiments for AD and LSQ identification methods. The KF curve indicates the tool tip position estimation obtained using θ_{off}. The highlighted part shows the data used for LSQ stiffness identification from $t = -2$ (s) to $t = -1$ (s).

The tool tip position in frame $\{B\}$ during the static experiment for KF combined with AD and LSQ identification methods are plotted in Fig. 4.3. In the same plot, the results for KF (with offline stiffness estimation), the camera (ground truth), and the robot FWK estimations (G_b) for tip position are plotted. For the same experiment, the online estimations of the AD method for $3EI$ for three different values of adaptive gain are plotted in Fig. 4.4. In addition, the offline estimation of $3EI$, i.e. θ_{off}^{-1} is also plotted with a red dashed line in Fig. 4.4. In order to find the estimation for $\hat{\theta}_{lsq}$ using the LSQ method, one second of preliminary data ($t = -2$ (s) to $t = -1$ (s)) before the static experiments were used (Fig. 4.3). After applying (4.10) on this data, we obtained

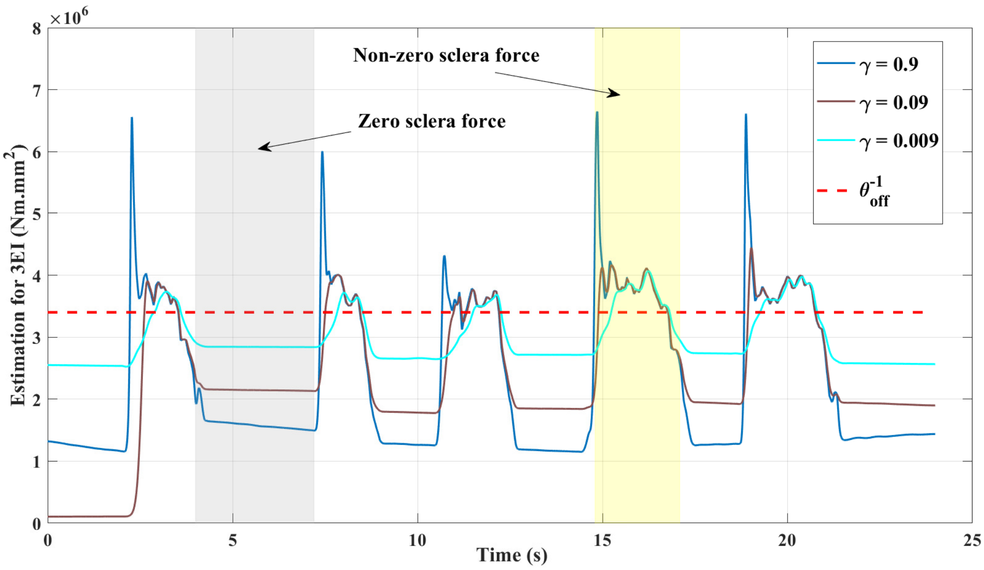

Figure 4.4: Results for the AD instrument stiffness identification during static experiments for different coefficients of the adaptive gain. The yellow-highlighted part indicates a parameter converging area and the grey-highlighted part shows a non-converging area.

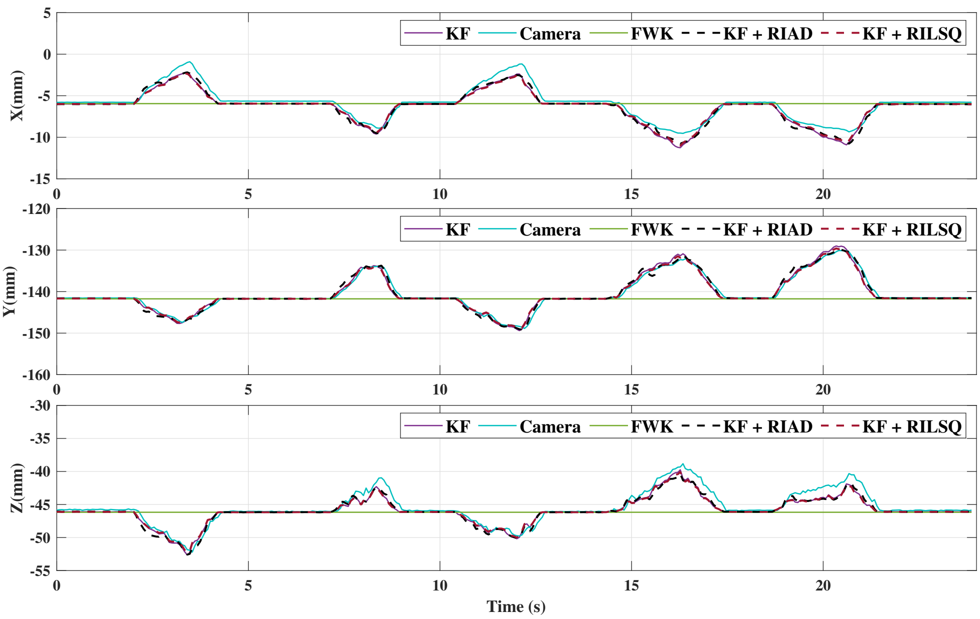

Figure 4.5: Tool tip position in frame $\{B\}$ during static experiments for RIAD and RILSQ identification methods. The KF curve indicates the tool tip position estimation obtained using θ_{off}.

$3.85 \times 10^6\, mN \cdot mm^2$ for the LSQ-based estimation of $3EI$, i.e. $\hat{\theta}_{lsq}^{-1}$. This estimation was used in the KF calculations for KF+LSQ plot in Fig. 4.3.

Similar plots for the RIAD and RILSQ approaches are shown in Figs. 4.5

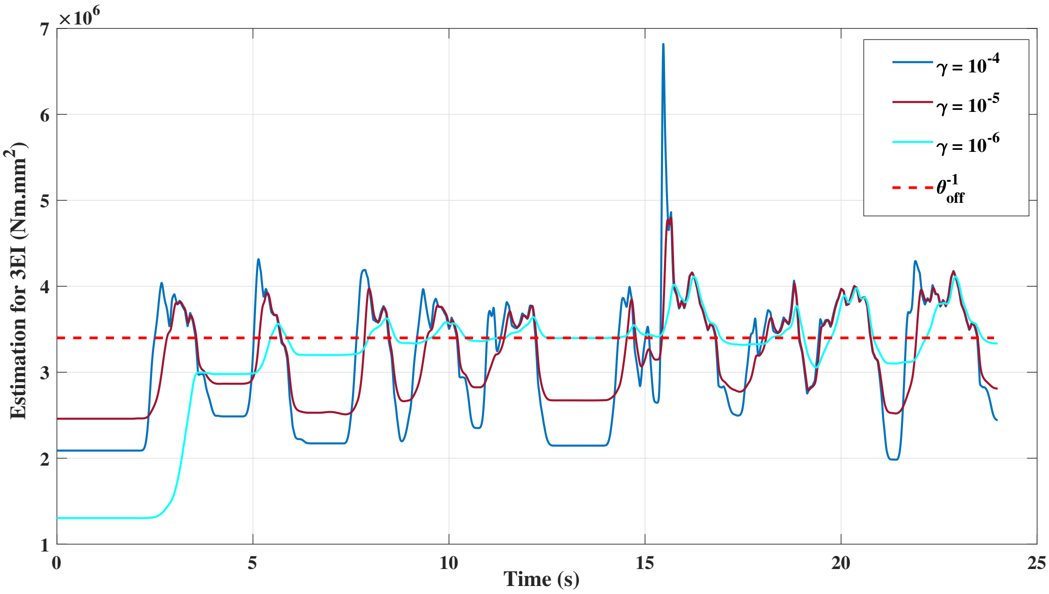

Figure 4.6: Results for the RIAD instrument stiffness identification during static experiments for different coefficients of the adaptive gain.

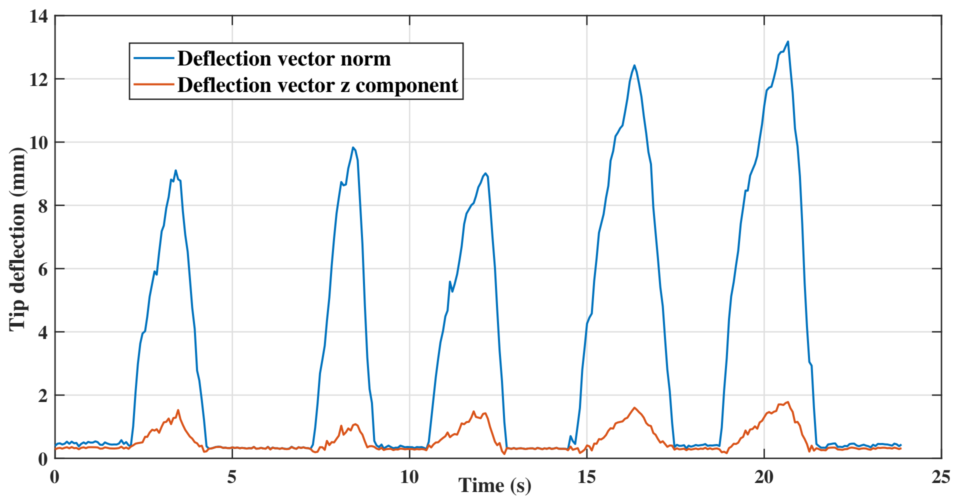

Figure 4.7: Results for magnitude and z component of the deflection vector Ω during the static experiments.

and 4.6. It is noted that for the RIAD method the time gap between i and j samples was set to 0.5 (s). For the same time interval of the preliminary data ($t = -2\ (s)$ to $t = -1\ (s)$) for identifying $\hat{\theta}_{lsq}$ using the RILSQ approach, we obtained $3.77 \times 10^6\ mN \cdot mm^2$ estimation for $3EI$. This estimation was used in the KF calculations for KF+RILSQ plot in Fig. 4.5. In order to assess our assumption for having zero value for the third element of vector Ω, we have plotted the magnitude of Ω and its Z^e component in Fig. 4.7.

The results of the dynamic experiments are plotted in Figs. 4.8-4.11. Figs. 4.8 and 4.9 represent the tip position in frame $\{B\}$ and the adaptive stiffness identification for the instrument stiffness, respectively. In Fig. 4.9 the offline

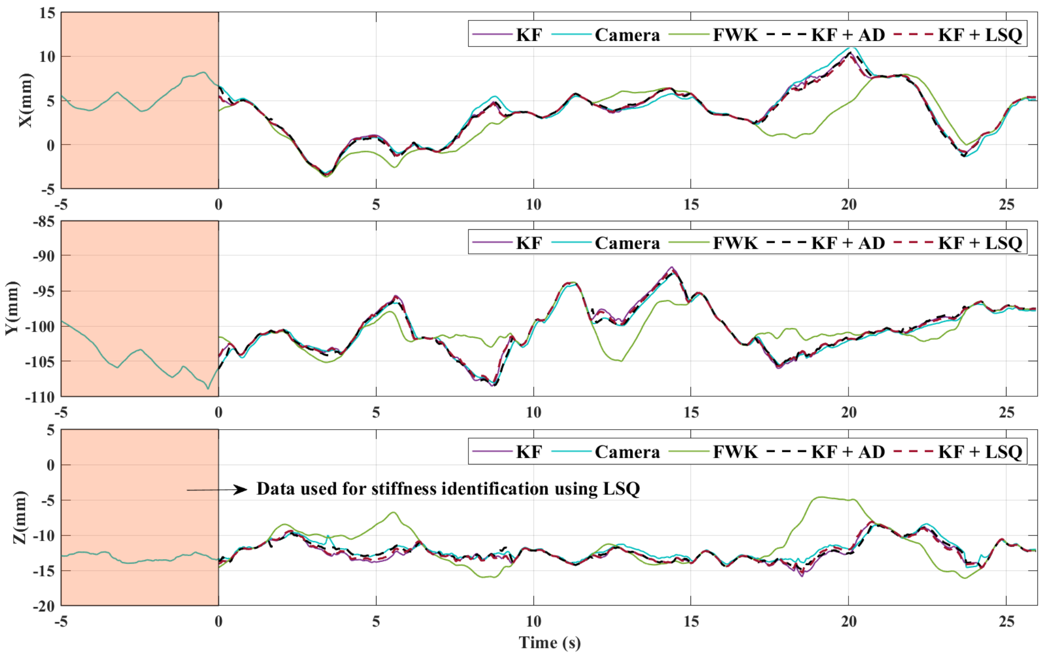

Figure 4.8: Tool tip coordinate positions in frame $\{B\}$ during dynamic experiments for AD and LSQ identification methods. The KF curve indicates the tool tip position estimation obtained using θ_{off}. The highlighted part shows the data used for LSQ stiffness identification from $t = -5$ (s) to $t = 0$ (s).

estimation for $3EI$ is plotted with a red dashed line for easier comparison. Similar plots for the RIAD and RILSQ implemented on the dynamic manipulation of the eyeball are plotted in Figs. 4.10 and 4.11. In order to implement the LSQ and RILSQ identification methods for the dynamic experiment, we used the data during 5 seconds prior to starting the experiment, which is highlighted in Fig. 4.9. After applying the associated algorithms, we found the values of $3.88 \times 10^6\, mN \cdot mm^2$ and $3.83 \times 10^6\, mN \cdot mm^2$ for $3EI$, respectively. These values were later used in the KF estimations for LSQ and RILSQ methods. The magnitude of the tool tip force during the dynamic experiment is plotted in Fig. 4.12. This force indicates any contact between the instrument tip and the posterior of the eyeball phantom interior.

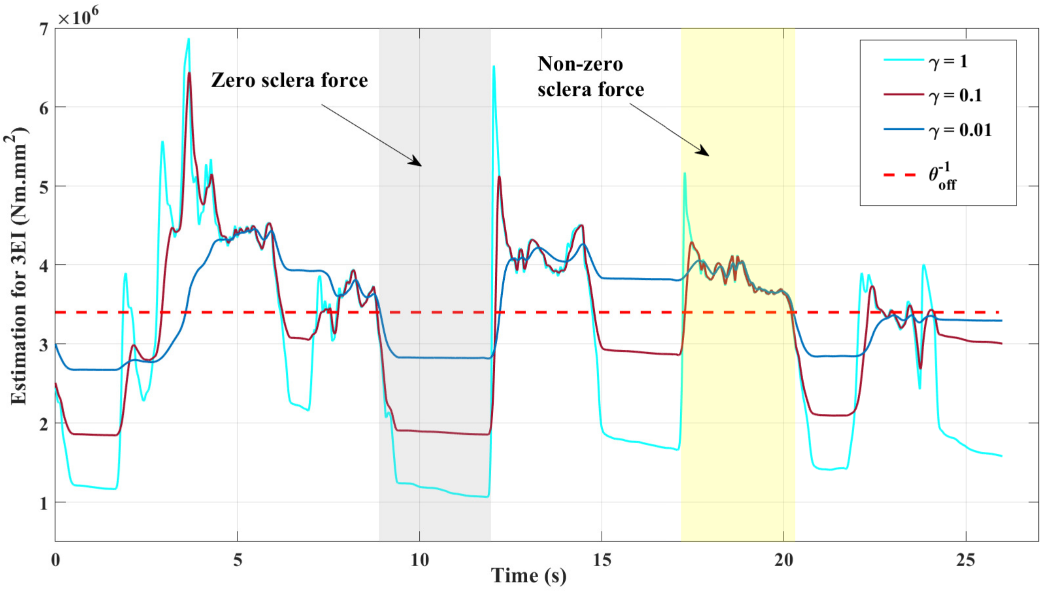

Figure 4.9: Online estimations for $\hat{\theta}^{-1}$ using AD approach during dynamic experiments. The estimations for three values of the adaptation coefficient γ are plotted.

In order to evaluate the RI algorithm during the camera movement and invisible tool tip intervals, we have conducted an additional validation experiment. Using the available data that we collected during the static experiments (Fig . 4.3), we synthesized a new set of data based on the following assumptions:

1. From $t = 0$ (s) to $t = 5$ (s), the tool tip is visible in the camera images.

2. From $t = 5$ (s) to $t = 10$ (s), the tool tip is invisible.

3. At $t = 10$ (s) the camera is moved 10 mm up vertically and remains there to the end of the experiment.

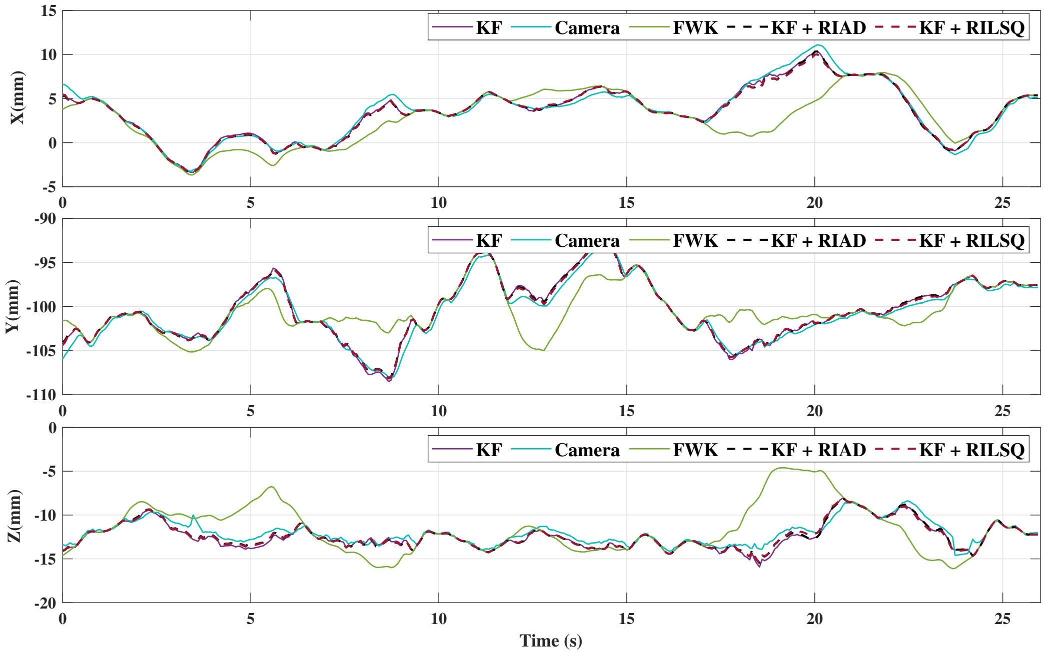

Figure 4.10: Tool tip coordinate positions in frame $\{B\}$ during dynamic experiments for RIAD and RILSQ identification methods. The KF curve indicates the tool tip position estimation obtained using θ_{off}.

The new set of camera data was synthesized for the third part of the above experiment by keeping the x and y coordinates the same as before, but the z component of the tool tip coordinate in the camera frame is subtracted by 10

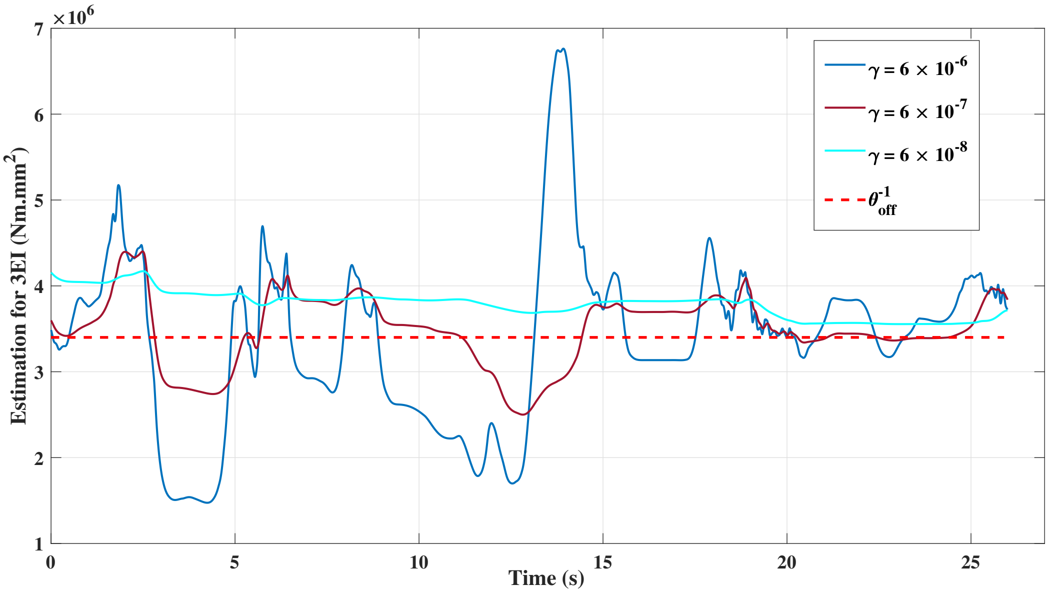

Figure 4.11: Online estimations for $\hat{\theta}^{-1}$ using the RIAD approach during the dynamic experiments. The estimations for three values of the adaptation coefficient γ are plotted.

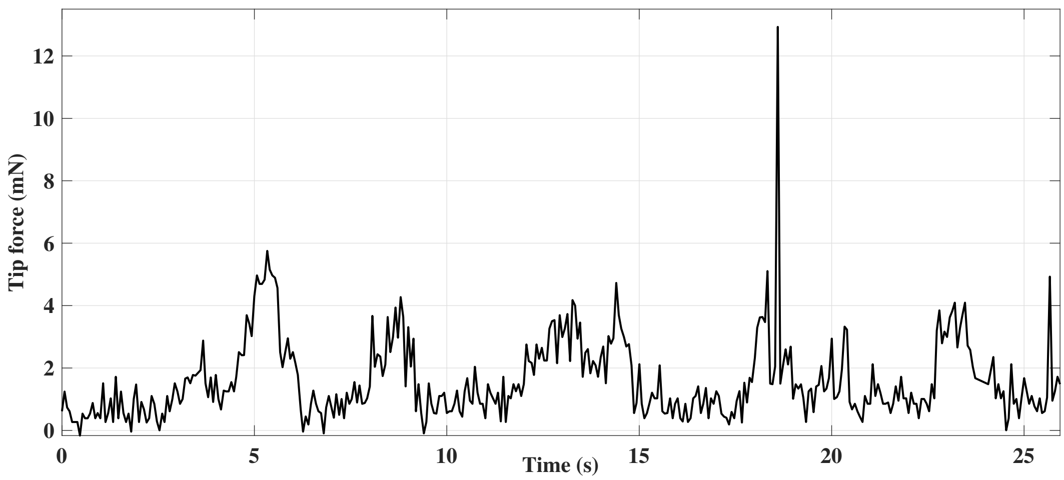

Figure 4.12: The interaction force between the instrument tip and the eye phantom posterior during the dynamic experiments.

mm for the entire data after $t = 10$ (s) during the static experiments (camera has moved 10 mm up). Then we ran the tip position estimation algorithm on

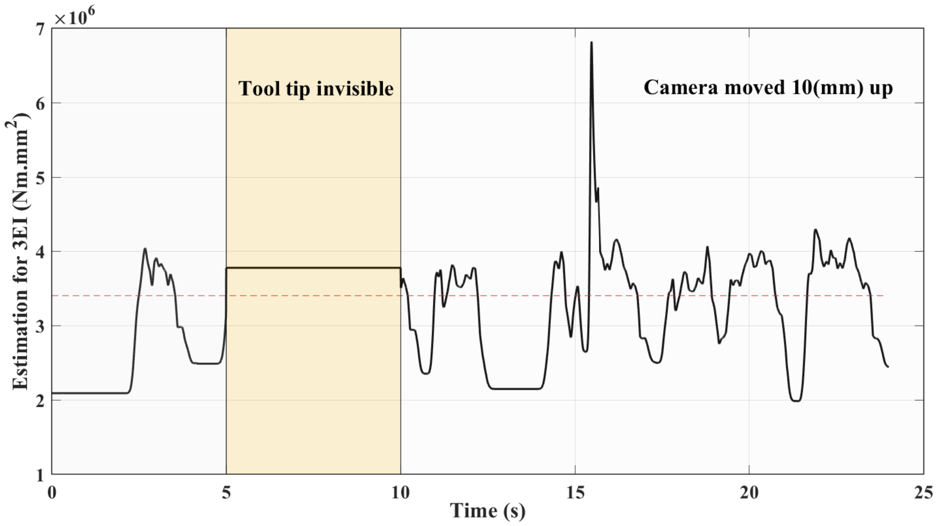

Figure 4.13: Variations of $\hat{\theta}^{-1}$ during the synthesised experiment when both invisible tool tip and camera movement happen. In the yellow-highlighted area the RILSQ estimation is used. In other areas the RIAD method is used with $\gamma = 0.001$.

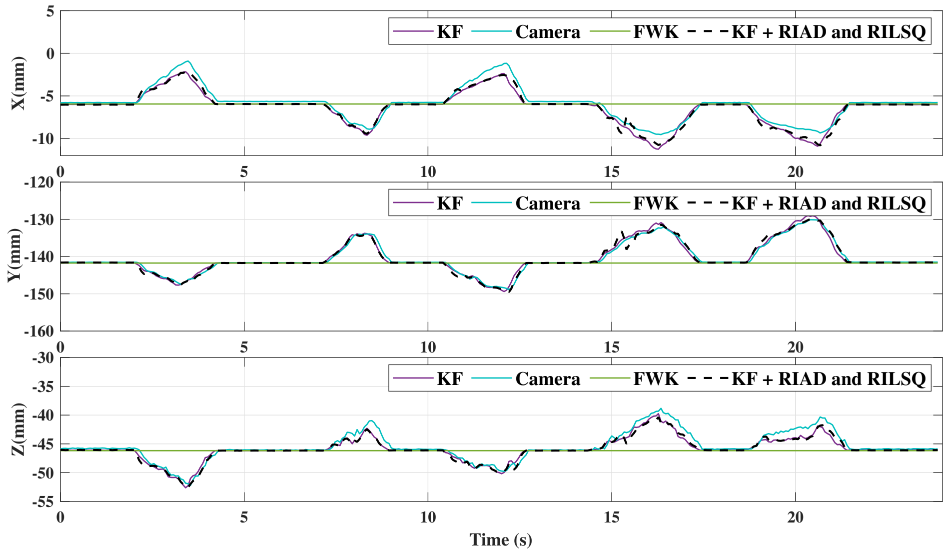

Figure 4.14: Tool tip coordinate positions in frame $\{B\}$ during the synthesised experiments when a combination of RIAD and RILSQ is used for stiffness identification.

the sequence of situations above. For the first part, the RIAD method was used to estimate θ. For the second part, we assumed the instrument tip is not visible and we did not use any camera data. For this reason, the least-squares estimation obtained prior to the experiment was used for the second part (RILSQ). For the third part, we re-ran the RIAD method on the new set of camera data (camera moved 10 (mm) up) and estimated θ again. The θ predicted during these scenarios were used in the KF framework to obtain the tool tip position. The plots for stiffness estimation and the tool tip position in the robot base frame for this experiment are provided in Figs. 4.13 and 4.14.

For all of the conducted experiments, the average magnitude value of the er-

Table 4.1: Error values for the static and dynamic experiments.

Experiment	Signal	Total Error (mm)	Error over deflected intervals (mm)	Error over not-deflected intervals (mm)
Static	KF (LSQ)	0.94	1.55	0.36
	KF (AD, $\gamma = 0.9$)	0.78	1.22	0.36
	KF (RILSQ)	0.93	1.53	0.36
	KF (RIAD, $\gamma = 1 \times 10^{-4}$)	0.90	1.46	0.36
	KF (Offline)	0.94	1.54	0.36
	KF (RIAD + RILSQ)	0.91	1.49	0.35
	Forward Kinematics	3.42	6.55	0.40
Dynamic	KF (LSQ)	0.77	0.95	0.44
	KF (AD, $\gamma = 1$)	0.62	0.70	0.47
	KF (RILSQ)	0.77	0.95	0.44
	KF (RIAD, $\gamma = 5 \times 10^{-7}$)	0.77	0.95	0.44
	KF (Offline)	0.81	1.02	0.44
	Forward Kinematics	2.98	4.38	0.44

ror vectors between the tool tip coordinate and the camera estimation (ground truth) are represented in Table 4.1. To better study the error values, they are calculated for the following two intervals as it is written in Table 4.1: 1) deflected 2) not-deflected. A deflected interval indicate all of the time interval during the experiment when the error between the associated method and the robot FWK output, which does not see the instrument deflection, for tip position is more than $0.1\ mm$. Any other time interval during the experiment is included in the not-deflected interval. We compared the errors during the deflected intervals (when the instrument is deflected) otherwise in non-deflected situations all of the methods would have similar outputs.

4.7 Discussion and Conclusion

In this chapter we developed a novel framework for estimating deflected surgical instrument tip position during robot-assisted ophthalmic procedures. This algorithm can be implemented using any of the online estimation methods for instrument stiffness namely AD, LSQ, RIAD, and RILSQ approaches combined with a KF-based sensor fusion algorithm. Compared to all other previously developed methods, when the RIAD and RILSQ methods are used there is no need to know the transformation between the robot and the visual modality coordinate frames. This is extremely beneficial as the visual modality (e.g. the surgical microscope) often moves during routine ophthalmic surgical procedures.

As a general overview when observing Figs. 4.3, 4.5, 4.8, and 4.10 as well as Table 4.1, it can be seen that all of the AD, LSQ, RIAD, and RILSQ algorithms, once combined with the KF estimation method provide accurate results for the instrument tip position even when the instrument undergoes deflections. In other methods, the KF estimations based on the developed methods follow the ground truth value for instrument tip position obtained from the camera. From the same figures, it is noted that the tip position obtained from the FWK does not detect the deflections.

By observing Fig. 4.7 we can see that the Z^e component of the deflection vector Ω is almost one tenth of its norm. Considering that the z deflection is one order of magnitude smaller than the deflection norm, we think that the displacement of the needle tip along the Z^e axis is negligible compared to the displacements of the needle tip perpendicular to the needle shaft, which was assumed in the Section 4.3.

Of note, the instrument is not necessarily a perfect cantilever beam. For this reason, the offline estimation for θ_{off}^{-1} is not the actual reference value that indicates the instrument stiffness. However, it is an average value of the instrument stiffness along the instrument shaft. This is the shortcoming of the least squares approach for online estimation, because it only calculates an average value of stiffness in the vicinity of the region where data is collected. For this reason, there are slight discrepancies between the estimations of least squares-based methods for stiffness during the static and dynamic experiments (e.g. $3.85 \times 10^6\, mN \cdot mm^2$ and $3.88 \times 10^6\, mN \cdot mm^2$) for LSQ method. However, the adaptive method keeps updating the instrument stiffness based on what portion of the instrument shaft is in contact with the tissue which in turn provides a better estimation of the local stiffness of the instrument shaft. That is why the adaptive estimations (i.e. in Figs. 4.4, 4.6, 4.9, 4.11) oscillate around the offline estimation value as different locations of the instrument shaft may have different local stiffness values. The online least squares-based methods, however, are advantageous for not requiring any continuous update of the stiffness estimation and can be used when the tool tip is not visualized in the microscope view (as demonstrated in Fig. 4.13).

Table 4.1 demonstrates that for both static and dynamic experiments, all of the online estimation methods have smaller average error values during deflected intervals compared to the corresponding error value for the offline estimation approach (except for the LSQ method during the static experiments, for which the averaged error is slightly larger than the offline method). Furthermore, in both static and dynamic experiments, the averaged error during deflected intervals is the lowest for AD estimation method (1.22 mm in static and 0.70 mm in dynamic experiments). This indicates the dual benefit of online estimation methods when combined with KF. They are not only independent of the need for pre-operative calibration of instrument stiffness, but also they provide more accurate results. Registration-independent approaches have the additional advantage of no requirement for prior knowledge for frame transformation between the robot base and the visual modality, while maintaining the two prior benefits for the online estimations.

The γ coefficient in the adaptive method is fine-tuned with trial and error for the AD and RIAD algorithms to have a fast convergence of $\hat{\theta}^{-1}$. Different values of γ lead to different behaviors of the $\hat{\theta}^{-1}$. For example, in Fig. 4.4, larger values of γ result in lower convergence time to the offline parameter with the cost of larger overshoots. Therefore, in Fig. 4.4, $\gamma = 0.9$ is chosen for KF+AD plot in Fig. 4.3. Because this γ value shows a fast convergence, the initial condition for $\hat{\theta}^{-1}$ does not affect the results and therefore is chosen randomly. On other hand, very large variations of $\hat{\theta}^{-1}$ can be seen, for example, in Fig. 4.11 for the largest value of γ ($\gamma = 6 \times 10^{-6}$), which is not an optimal behaviour. As it can be seen from the variations for adaptive estimations of $\hat{\theta}^{-1}$ (e.g. Figs. 4.4 and 4.9), the estimations are updated and converge to the local stiffness of the instrument shaft only when the input signal $U(t)$ is non-zero (as highlighted with light yellow in Figs. 4.4 and 4.9), which is what was proved in (4.28). From (4.5), it can be realized that $U(t)$ is non-zero only if $F(t)$, sclera forces, are not zero. This corresponds to when the instrument shaft is deflected. This conforms with intuition as well because the online estimation methods are only able to estimate the instrument stiffness if there is a deflection in the instrument shaft, otherwise there will not be any stiffness-related data available for identification. Of note, during zero sclera force intervals (highlighted with light gray in Figs. 4.4 and 4.9) the fixed value of $\hat{\theta}^{-1}$ does not have any effect on the tip position estimation algorithm output. This is because the adaptive estimation is not updated ($\dot{\hat{\theta}} = 0$ based on (4.13)) and the left hand side of (3.10) will be $Y^P = \frac{1}{\beta}\mathbf{R}_{be}^T S_{be}$ (because the sclera force vector F_s is zero). If we plug this Y^P into the second equation in (4.3) and multiply both sides of this equation by $\mathbf{R}_{be}\beta$, we will have $S_{be} = P + \mathbf{R}_{be}\beta V^P$ meaning that the sensor equation for the tip position state-space model is basically S_{be} and is independent of $\hat{\theta}^{-1}$. Therefore, although for example in Fig. 4.9 it may seem that $\hat{\theta}^{-1}$ has large variations, those variations in the grey-highlighted zones are meaningless, and they are just a bounded value that the non-updating $\hat{\theta}^{-1}$ converges to, and as explained does not have any effect on the algorithm output. Of note, in the yellow-highlighted areas in Fig. 4.9, the $\hat{\theta}^{-1}$ estimation has little variations and remains close to the θ_{off}^{-1}. For the LSQ and RILSQ methods also sufficient deflection on the instrument shaft is required for the learning algorithm to work. The learning time interval for the least square-based methods should especially be elongated (larger values of m in (4.9)) if not enough instrument bending is included in a learning time interval. Of note, the lengths of learning time interval for the static and dynamic experiments were different (1(s) and 5(s), respectively).

It is noteworthy to mention that the developed state-space model for KF as well as the online estimation methods encompass the assumption that only one force (sclera force) is applied to the instrument shaft. In other words, these algorithms will not output correct estimations if another force (e.g. tip force) is exerted to the tool shaft. During the dynamic experiments, it can be seen from Fig .4.12 around $t = 19\ (s)$ that a tip force with magnitude of 12 mN is applied. If we look at the same time in Figs. 4.8 and 4.10, it can be seen that although the algorithms still follow the ground truth the estimations are not as good due to the tip force.

As demonstrated in the current implementation, we attached a red marker to the instrument tip and used a stereo camera system and a color segmentation method to provide input to the online stiffness identification algorithms. The color segmentation method is susceptible to inconsistent results due to variations in environment lighting and existence of other similar colors in the camera view. However, because the focus of this study is a proof-of-concept evaluation of the developed algorithms, we used more straightforward vision and segmentation methods to view and localize the instrument tip. The stereo camera system is only a way to visualize the instrument tip position and is not the focus of the current study. Any other method to view, segment and localize the instrument tip can be substituted with the one used here, e.g. [131, 132]. We think that in a real ophthalmic surgical scenario, the availability of high-quality stereo microscopes as well as OCT imaging can provide more accurate localization of the instrument tip leading to more precise outcomes for the algorithm. It is noted that the current achieved accuracy, are still very beneficial for macro-manipulation tasks in robotic ophthalmic surgery, e.g. robot-assisted light probe holding.

In summary, this chapter reports the development of a novel force-based registration-independent framework in which we can simultaneously estimate the instrument stiffness as well as the bent instrument tip position in real-time. Compared to other tool tip localization approaches for robot-assisted eye surgery, the developed methods do not require a frame transformation between the visual modality and the robot base frame and can be potentially used in case of camera movement. Furthermore, other vision-based methods presented in the published literature fail to continue their estimation if the tool tip is not visible during surgery. The present developed framework, however, can continue to provide estimations of the tool tip position during periods that the tip is not visible, i.e using the least squares-based approaches where continuous update for the stiffness is not required. As it was observed from Figs. 4.13 and 4.14 and the numerical error results in Table 4.1, the algorithm can handle the camera movement and invisible tip position intervals and properly predict the deflected tip position.

4.8 Publications

Journal Publications:

- **Ali Ebrahimi**, Shahriar Sefati, Russell Taylor, Peter Gehlbach, and Iulian Iordachita *"Simultaneous Online Registration-Independent Stiffness Identification and Tip Localization of Surgical Instruments in Robot-assisted Eye Surgery"*, IEEE Transactions on Robotics (TRO), 2022.

Chapter 5

Conclusions and Outlook

5.1 Introduction

Retinal surgery continues to be one of the most demanding surgical practices entailing very sensitive tissue manipulation. Reducing surgeon hand tremor and consequently enhancing tool tip precision would be of principal importance, which have been successfully fulfilled by advancements in robot-assisted eye surgery, sensorized instruments, and state-of-the-art technology for visual modalities. Once optimized, it is believed that greater precision, safety efficiency are possible, which will offset any early increase in costs. Improved control and state estimation methods can substantially contribute to a safer robot-assisted surgical procedure and potentially broaden the present range of offered treatments and also provide automated procedures. This dissertation provides theoretical algorithms control, parameter and state estimation methods for robot-assisted. The developed methods are intended to enhance robot sensing capabilities of the surgical state and to provide autonomous safety control methods, in which the robot automatically guarantees safety in case of excessive tissue interaction forces.

In previous chapters, we developed control methods to autonomously control the tool-to-tissue sclera forces and the instrument insertion depth in safe ranges. State estimation methods were also developed to enhance precision in measurement of instrument insertion depth inside of the eye and the instrument needle tip position when it undergoes deflection. In this Chapter, the theoretical and technical achievements and contribution of this dissertation are summarized and future works and directions are discussed.

5.2 Summary of Chapters and Future Work

- **Chapter 1**:

  In chapter 1 the challenges for ophthalmic surgical tasks specially retinal vein cannulation (RVC) were discussed. Due to the formidable characteristics of RVC, it is not currently a regularly performed procedure. Surgeons physiological hand tremor adversely affects these procedures. On the other hand, interaction forces during RVC are below human tactile perception and any excessive forces due to targeting inaccuracies may put the retinal tissue at high risk of injury. Then the benefits of robotic and technological systems and sensors being incorporated into the surgical flow for such surgical procedures were delineated. Robotic systems have proven beneficial in substantially reducing the surgeon hand-tremor and providing a steadier tissue manipulation. Force-sensing instrument and advanced visual modalities can effectively increase the surgeons's awareness of the surgical state. However, in robot-assisted ophthalmic procedures we speculate that disconnecting the surgeon from sensory inputs that they used to rely on during manual surgeries may increase the risk of injury to the eye and affect the surgeon's usual technique. For this reason, we have tried to incorporate control methods and state estimation algorithms to the robot to enhance safety and improve the robot sensing capabilities.

- **Chapter 2**:

  In chapter 2, we argued that the elimination of hand tremor through the introduction of microsurgical robots diminishes the surgeon's tactile perception of useful and familiar tool-to-sclera forces. While the large mass and inertia of eye surgical robot prevents surgeon microtremor, loss of perception of small sclera forces may put the sclera at risk of injury during robot-assisted procedures. For this reason and to enhance robot safe manipulation, we have implemented an adaptive control scheme on the SHER to simultaneity control the sclera forces components and the instrument insertion depth using a customized FBG-equipped instrument. When any of these parameters tend to overstep safe values, the robot reduces the sclera forces or insertion depth to safe boundaries based predefined desired trajectories. The evaluation for two variants of the adaptive sclera force control (ACC and ANC) was carried out by enrolling ten robot-novice ophthalmology clinicians in simulated robot-assisted eye surgeries while the control methods were implemented on the SHER. We conclude that the ACC and the ANC methods are able to maintain sclera forces within safe boundaries, potentially enhancing safety for retinal surgery patients undergoing robot-assisted procedures. It is noted that for robot-novice users the test procedure was more comfortable to be performed freehand, and took longer when using the robot assistance. This was true for both the ACC and ANC control methods. It is possible that significant training may allow users to increase their acceptance of the control methods during retinal surgery. This is potentially important as both control methods successfully reduced the application of forces to the eye.

- **Chapter 3**:

  In Chapter 3, first we summarize the difficulties for needle tip localization during ophthalmic surgical tasks. Vision-based methods have certain limitations including poor depth perception and the need for continuous visibility of the tool tip in the microscope view. In contrast to vision-based methods, a force-based framework was developed for simultaneous improvement of measurements for instrument insertion depth inside of the eye as well as needle tip position when it undergoes deflection. Discrete state-space models were formulated for the evolution of insertion depth and tool tip position. Then the relevant sources of information obtained from FWK and FBG sensors for measuring insertion depth and tool tip position were combined using a Kalman Filtering approach. Of note, such information is critical for safety enhancement and more accurate feedback in semi-autonomous robot-assisted tasks in eye surgery. The associated estimations were significantly improved using the developed framework, which is not dependent on any vision source. Future work includes, but not limited to, the development of robot control schemes for autonomous surgical tasks utilizing the improved estimations. Although we predict that the developed method should work in a moving eye environment (because the algorithm is based on the relative motion of the instrument and the eye, rather than absolute motion and because this relative motion was simulated in the dynamic experiments), assessing the algorithm in the setting of a moving eye is important to validate the prediction. Furthermore, evaluating the algorithms *in vivo* is a necessary direction for the future work.

- **Chapter 4**:

  Chapter 4 describes how we build upon the force-based state space framework that was reported in Chapter 3 and add special features to the needle tip localization algorithm. The developed force-based method does not have the limitations of the algorithms for needle tip localization that work based on vision. However, it requires that the mechanical properties (stiffness) of all instruments be obtained during pre-operative calibration experiments. Chapter 4 explains how this dependency is removed by combining force- and vision-based methods to obtain online adaptive/least squares estimations of the instrument stiffness. Theory is further developed to make the entire framework independent of the frame transformation between the visual modality and the robot base, which is a primary limitation of all vision-based works reported in the literature. Because of this novel registration-independent property of the framework, it can be potentially used in case of microscope movement, which typically happens during a ophthalmic surgery. Furthermore, other vision-based methods presented in the published literature fail to continue their estimation if the tool tip is not visible during surgery. The present developed framework, however, can continue to provide estimations of the tool tip position during periods that the tip is not visible. The effectiveness of the developed method is evaluated during static and dynamic phantom experiments. The developed algorithm has the capability of providing more accurate tool tip localization if more precise visual modalities (e.g. OCT or available high-quality ophthalmic surgical microscopes) are used, which can be further researched in the future. Among other future directions of this work is testing the entire framework during realistic in-vivo experiments.

Bibliography

[1] I. I. Iordachita, M. D. De Smet, G. Naus, M. Mitsuishi, and C. N. Riviere, "Robotic assistance for intraocular microsurgery: Challenges and perspectives," *Proceedings of the IEEE*, vol. 110, no. 7, pp. 893–908, 2022.

[2] A. George and D. Larkin, "Corneal transplantation: the forgotten graft," *American Journal of Transplantation*, vol. 4, no. 5, pp. 678–685, 2004.

[3] E. Skiadaresi, C. McAlinden, K. Pesudovs, S. Polizzi, J. Khadka, and G. Ravalico, "Subjective quality of vision before and after cataract surgery," *Archives of ophthalmology*, vol. 130, no. 11, pp. 1377–1382, 2012.

[4] P. K. Gupta, P. S. Jensen, and E. d. Juan, "Surgical forces and tactile perception during retinal microsurgery," in *International conference on medical image computing and computer-assisted intervention*. Springer, 1999, pp. 1218–1225.

[5] Z. Nagy, A. Takacs, T. Filkorn, and M. Sarayba, "Initial clinical evalua-

tion of an intraocular femtosecond laser in cataract surgery," *Journal of refractive surgery*, vol. 25, no. 12, pp. 1053–1060, 2009.

[6] E. J. Linebarger, D. R. Hardten, G. K. Shah, and R. L. Lindstrom, "Phacoemulsification and modern cataract surgery," *Survey of ophthalmology*, vol. 44, no. 2, pp. 123–147, 1999.

[7] N. Congdon, B. O'Colmain, C. Klaver, R. Klein, B. Muñoz, D. S. Friedman, J. Kempen, H. R. Taylor, P. Mitchell *et al.*, "Causes and prevalence of visual impairment among adults in the united states." *Archives of Ophthalmology (Chicago, Ill.: 1960)*, vol. 122, no. 4, pp. 477–485, 2004.

[8] D. Pascolini, S. Mariotti, G. Pokharel, R. Pararajasegaram, D. Etya'Ale, A.-D. Négrel, and S. Resnikoff, "2002 global update of available data on visual impairment: a compilation of population-based prevalence studies," *Ophthalmic epidemiology*, vol. 11, no. 2, pp. 67–115, 2004.

[9] B. E. Kobrin Klein, "Overview of epidemiologic studies of diabetic retinopathy," *Ophthalmic epidemiology*, vol. 14, no. 4, pp. 179–183, 2007.

[10] A. Mariotti and D. Pascolini, "Global estimates of visual impairment," *Br J Ophthalmol*, vol. 96, no. 5, pp. 614–8, 2012.

[11] D. Yorston, "Retinal diseases and vision 2020," *Community Eye Health*, vol. 16, no. 46, pp. 19–20, 2003.

[12] H. Nazimul, K. Rohit, and H. Anjli, “Trend of retinal diseases in developing countries,” *Expert Review of Ophthalmology*, vol. 3, no. 1, pp. 43–50, 2008.

[13] T. H. Williamson, “Introduction to vitreoretinal surgery,” in *Vitreoretinal surgery*. Springer, 2013, pp. 21–60.

[14] J. Rehak and M. Rehak, “Branch retinal vein occlusion: pathogenesis, visual prognosis, and treatment modalities,” *Current eye research*, vol. 33, no. 2, pp. 111–131, 2008.

[15] K. Willekens, A. Gijbels, L. Schoevaerdts, L. Esteveny, T. Janssens, B. Jonckx, J. H. Feyen, C. Meers, D. Reynaerts, E. Vander Poorten, and P. Stalmans, “Robot-assisted retinal vein cannulation in an in vivo porcine retinal vein occlusion model,” *Acta ophthalmologica*, vol. 95, no. 3, pp. 270–275, 2017.

[16] T. Y. Wong and I. U. Scott, “Retinal-vein occlusion,” *New England Journal of Medicine*, vol. 363, no. 22, pp. 2135–2144, 2010.

[17] S. Rogers, R. L. McIntosh, N. Cheung, L. Lim, J. J. Wang, P. Mitchell, J. W. Kowalski, H. Nguyen, T. Y. Wong, and I. E. D. Consortium, “The prevalence of retinal vein occlusion: pooled data from population studies from the United States, Europe, Asia, and Australia,” *Ophthalmology*, vol. 117, no. 2, pp. 313–319, 2010.

[18] R. Klein, S. E. Moss, S. M. Meuer, and B. E. Klein, “The 15-year cumulative incidence of retinal vein occlusion: the beaver dam eye study,” *Archives of ophthalmology*, vol. 126, no. 4, pp. 513–518, 2008.

[19] P. Kolar, “Risk factors for central and branch retinal vein occlusion: a meta-analysis of published clinical data,” *Journal of ophthalmology*, vol. 2014, no. 724780.

[20] P. Jefferies, R. Clemett, and T. Day, “An anatomical study of retinal arteriovenous crossings and their role in the pathogenesis of retinal branch vein occlusions,” *Australian and New Zealand journal of ophthalmology*, vol. 21, no. 4, pp. 213–217, 1993.

[21] S. S. Hayreh, M. B. Zimmerman, and P. Podhajsky, “Incidence of various types of retinal vein occlusion and their recurrence and demographic characteristics,” *American journal of ophthalmology*, vol. 117, no. 4, pp. 429–441, 1994.

[22] “Natural history and clinical management of central retinal vein occlusion,” *Archives of Ophthalmology*, vol. 115, pp. 486–491, 1997.

[23] K. Inagaki, K. Ohkoshi, S. Ohde, G. A. Deshpande, N. Ebihara, and A. Murakami, “Subthreshold micropulse photocoagulation for persistent macular edema secondary to branch retinal vein occlusion including

best-corrected visual acuity greater than 20/40," *Journal of Ophthalmology*, vol. 2014, no. 251257, 2014.

[24] A. Glacet-Bernard, M. Atassi, C. Fardeau, J.-P. Romanet, M. Tonini, J. Conrath, P. Denis, M. Mauget-Faÿsse, G. Coscas, and G. Soubrane, "Hemodilution therapy using automated erythrocytapheresis in central retinal vein occlusion: results of a multicenter randomized controlled study," *Graefe's Archive for Clinical and Experimental Ophthalmology*, vol. 249, no. 4, pp. 505–512, 2011.

[25] J. Garcia-Arumi, A. Boixadera, V. Martinez-Castillo, M. Montolio, A. Verdugo, and B. Corcostegui, "Radial optic neurotomy in central retinal vein occlusion: comparison of outcome in younger vs older patients," *American Journal of Ophthalmology*, vol. 143, no. 1, pp. 134–140, 2007.

[26] K. Kumagai, M. Furukawa, N. Ogino, A. Uemura, and E. Larson, "Long-term outcomes of vitrectomy with or without arteriovenous sheathotomy in branch retinal vein occlusion," *Retina*, vol. 27, no. 1, pp. 49–54, 2007.

[27] E. Moisseiev, M. Goldstein, M. Waisbourd, A. Barak, and A. Loewenstein, "Long-term evaluation of patients treated with dexamethasone intravitreal implant for macular edema due to retinal vein occlusion," *Eye*, vol. 27, no. 1, pp. 65–71, 2013.

[28] A. R. Berger, A. F. Cruess, F. Altomare, V. Chaudhary, K. Colleaux,

M. Greve, A. Kherani, E. D. Mandelcorn, H. Parsons, and M.-A. Rhéaume, “Optimal treatment of retinal vein occlusion: Canadian expert consensus,” *Ophthalmologica*, vol. 234, no. 1, pp. 6–25, 2015.

[29] I. L. McAllister and I. J. Constable, “Laser-induced chorioretinal venous anastomosis for treatment of nonischemic central retinal vein occlusion,” *Archives of Ophthalmology*, vol. 113, no. 4, pp. 456–462, 1995.

[30] S. Yamamoto, W. Saito, F. Yagi, S. Takeuchi, E. Sato, and S. Mizunoya, “Vitrectomy with or without arteriovenous adventitial sheathotomy for macular edema associated with branch retinal vein occlusion,” *American journal of ophthalmology*, vol. 138, no. 6, pp. 907–914, 2004.

[31] E. M. Opremcak, A. J. Rehmar, C. D. Ridenour, and D. E. Kurz, “Radial optic neurotomy for central retinal vein occlusion: 117 consecutive cases,” *Retina*, vol. 26, no. 3, pp. 297–305, 2006.

[32] J. F. Arevalo, R. A. Garcia, L. Wu, F. J. Rodriguez, J. Dalma-Weiszhausz, H. Quiroz-Mercado, V. Morales-Canton, J. A. Roca, M. H. Berrocal, and F. Graue-Wiechers, “Radial optic neurotomy for central retinal vein occlusion: results of the pan-american collaborative retina study group (pacores),” *Retina*, vol. 28, no. 8, pp. 1044–1052, 2008.

[33] A. Glacet-Bernard, D. Kuhn, A. K. Vine, H. Oubraham, G. Coscas, and G. Soubrane, “Treatment of recent onset central retinal vein occlusion

with intravitreal tissue plasminogen activator: a pilot study," *British Journal of Ophthalmology*, vol. 84, no. 6, pp. 609–613, 2000.

[34] J. N. Weiss and L. A. Bynoe, "Injection of tissue plasminogen activator into a branch retinal vein in eyes with central retinal vein occlusion," *Ophthalmology*, vol. 108, no. 12, pp. 2249–2257, 2001.

[35] L.-O. Hattenbach, C. F. Arndt, R. Lerche, I. Scharrer, H. Baatz, F. Margaron, G. Richard, W. Behrens-Baumann, and C. Ohrloff, "Retinal vein occlusion and low-dose fibrinolytic therapy (rolf): a prospective, randomized, controlled multicenter study of low-dose recombinant tissue plasminogen activator versus hemodilution in retinal vein occlusion," *Retina*, vol. 29, no. 7, pp. 932–940, 2009.

[36] C. N. Riviere and P. S. Jensen, "A study of instrument motion in retinal microsurgery," in *Proceedings of the 22nd Annual International Conference of the IEEE Engineering in Medicine and Biology Society (Cat. No. 00CH37143)*, vol. 1. IEEE, 2000, pp. 59–60.

[37] L. A. Bynoe, R. K. Hutchins, H. S. Lazarus, and M. A. Friedberg, "Retinal endovascular surgery for central retinal vein occlusion: initial experience of four surgeons," *Retina*, vol. 25, no. 5, pp. 625–632, 2005.

[38] T. Leng, J. M. Miller, K. V. Bilbao, D. V. Palanker, P. Huie, and M. S. Blumenkranz, "The chick chorioallantoic membrane as a model tissue

for surgical retinal research and simulation," *Retina*, vol. 24, no. 3, pp. 427–434, 2004.

[39] R. Taylor, P. Jensen, L. Whitcomb, A. Barnes, R. Kumar, D. Stoianovici, P. Gupta, Z. Wang, E. Dejuan, and L. Kavoussi, "A steady-hand robotic system for microsurgical augmentation," *The International Journal of Robotics Research*, vol. 18, no. 12, pp. 1201–1210, 1999.

[40] H. Saito and T. Togawa, "Detection of needle puncture to blood vessel using puncture force measurement," *Medical and Biological Engineering and Computing*, vol. 43, no. 2, pp. 240–244, 2005.

[41] T. Ueta, T. Nakano, Y. Ida, N. Sugita, M. Mitsuishi, and Y. Tamaki, "Comparison of robot-assisted and manual retinal vessel microcannulation in an animal model," *British Journal of Ophthalmology*, vol. 95, no. 5, pp. 731–734, 2011.

[42] M. F. Jacobsen, L. Konge, M. Alberti, M. La Cour, Y. S. Park, and A. S. S. Thomsen, "Robot-assisted vitreoretinal surgery improves surgical accuracy compared with manual surgery: a randomized trial in a simulated setting," *Retina (Philadelphia, Pa.)*, vol. 40, no. 11, p. 2091, 2020.

[43] H. Yu, J.-H. Shen, R. J. Shah, N. Simaan, and K. M. Joos, "Evaluation of microsurgical tasks with oct-guided and/or robot-assisted ophthalmic forceps," *Biomedical optics express*, vol. 6, no. 2, pp. 457–472, 2015.

[44] S. L. Charreyron, Q. Boehler, A. N. Danun, A. Mesot, M. Becker, and B. J. Nelson, "A magnetically navigated microcannula for subretinal injections," *IEEE transactions on biomedical engineering*, vol. 68, no. 1, pp. 119–129, 2020.

[45] M. A. Nasseri, M. Eder, S. Nair, E. Dean, M. Maier, D. Zapp, C. P. Lohmann, and A. Knoll, "The introduction of a new robot for assistance in ophthalmic surgery," in *35th Annual International Conference of the IEEE Engineering in Medicine and Biology Society (EMBC)*. IEEE, 2013, pp. 5682–5685.

[46] S. Tanaka, K. Harada, Y. Ida, K. Tomita, I. Kato, F. Arai, T. Ueta, Y. Noda, N. Sugita, and M. Mitsuishi, "Quantitative assessment of manual and robotic microcannulation for eye surgery using new eye model," *The International Journal of Medical Robotics and Computer Assisted Surgery*, vol. 11, no. 2, pp. 210–217, 2015.

[47] C. He, L. Huang, Y. Yang, Q. Liang, and Y. Li, "Research and realization of a master-slave robotic system for retinal vascular bypass surgery," *Chinese Journal of Mechanical Engineering*, vol. 31, no. 1, p. 78, 2018.

[48] J. T. Wilson, M. J. Gerber, S. W. Prince, C.-W. Chen, S. D. Schwartz, J.-P. Hubschman, and T.-C. Tsao, "Intraocular robotic interventional surgical system (IRISS): Mechanical design, evaluation, and master–slave

manipulation," *The International Journal of Medical Robotics and Computer Assisted Surgery*, vol. 14, no. 1, p. e1842, 2018.

[49] Z. Li, M. Shahbazi, N. Patel, E. O. Sullivan, H. Zhang, K. Vyas, P. Chalasani, A. Deguet, P. L. Gehlbach, I. Iordachita *et al.*, "Hybrid robotic-assisted frameworks for endomicroscopy scanning in retinal surgeries," *arXiv preprint arXiv:1909.06852*, 2019.

[50] I. Fleming, M. Balicki, J. Koo, I. Iordachita, B. Mitchell, J. Handa, G. Hager, and R. Taylor, "Cooperative robot assistant for retinal microsurgery," in *International conference on medical image computing and computer-assisted intervention*. Springer, 2008, pp. 543–550.

[51] A. Gijbels, J. Smits, L. Schoevaerdts, K. Willekens, E. B. Vander Poorten, P. Stalmans, and D. Reynaerts, "In-human robot-assisted retinal vein cannulation, a world first," *Annals of Biomedical Engineering*, pp. 1–10, 2018.

[52] R. Kumar, P. Berkelman, P. Gupta, A. Barnes, P. S. Jensen, L. L. Whitcomb, and R. H. Taylor, "Preliminary experiments in cooperative human/robot force control for robot assisted microsurgical manipulation," in *Proceedings 2000 ICRA. Millennium Conference. IEEE International Conference on Robotics and Automation. Symposia Proceedings (Cat. No. 00CH37065)*, vol. 1. IEEE, 2000, pp. 610–617.

[53] B. Mitchell, J. Koo, I. Iordachita, P. Kazanzides, A. Kapoor, J. Handa, G. Hager, and R. Taylor, “Development and application of a new steady-hand manipulator for retinal surgery,” in *Proceedings 2007 IEEE International Conference on Robotics and Automation (ICRA)*, 2007, pp. 623–629.

[54] A. Üneri, M. A. Balicki, J. Handa, P. Gehlbach, R. H. Taylor, and I. Iordachita, “New steady-hand eye robot with micro-force sensing for vitreoretinal surgery,” in *2010 3rd IEEE RAS & EMBS International Conference on Biomedical Robotics and Biomechatronics*. IEEE, 2010, pp. 814–819.

[55] X. He, D. Roppenecker, D. Gierlach, M. Balicki, K. Olds, P. Gehlbach, J. Handa, R. Taylor, and I. Iordachita, “Toward clinically applicable steady-hand eye robot for vitreoretinal surgery,” in *ASME 2012 international mechanical engineering congress and exposition*. American Society of Mechanical Engineers, 2012, pp. 145–153.

[56] T. Edwards, K. Xue, H. Meenink, M. Beelen, G. Naus, M. Simunovic, M. Latasiewicz, A. Farmery, M. de Smet, and R. MacLaren, “First-in-human study of the safety and viability of intraocular robotic surgery,” *Nature biomedical engineering*, vol. 2, no. 9, pp. 649–656, 2018.

[57] B. C. Becker, S. Yang, R. A. MacLachlan, and C. N. Riviere, “Towards vision-based control of a handheld micromanipulator for retinal cannu-

lation in an eyeball phantom," in *2012 4th IEEE RAS & EMBS International Conference on Biomedical Robotics and Biomechatronics (BioRob)*. IEEE, 2012, pp. 44–49.

[58] W. Latt, U.-X. Tan, C. Shee, and W. Ang, "A compact hand-held active physiological tremor compensation instrument," in *2009 IEEE/ASME International Conference on Advanced Intelligent Mechatronics*. IEEE, 2009, pp. 711–716.

[59] C. J. Payne, K.-W. Kwok, and G.-Z. Yang, "An ungrounded hand-held surgical device incorporating active constraints with force-feedback," in *2013 IEEE/RSJ International Conference on Intelligent Robots and Systems*. IEEE, 2013, pp. 2559–2565.

[60] D. Chang, G. M. Gu, and J. Kim, "Design of a novel tremor suppression device using a linear delta manipulator for micromanipulation," in *2013 IEEE/RSJ International Conference on Intelligent Robots and Systems*. IEEE, 2013, pp. 413–418.

[61] A. Saxena and R. V. Patel, "An active handheld device for compensation of physiological tremor using an ionic polymer metallic composite actuator," in *2013 IEEE/RSJ International Conference on Intelligent Robots and Systems*. IEEE, 2013, pp. 4275–4280.

[62] S. Kyeong, D. Chang, Y. Kim, G. M. Gu, S. Lee, S. Jeong, and J. Kim, "A

hand-held micro surgical device for contact force regulation against involuntary movements," in *2015 37th Annual International Conference of the IEEE Engineering in Medicine and Biology Society (EMBC)*. IEEE, 2015, pp. 869–872.

[63] G. W. Cheon, P. Lee, B. Gonenc, P. L. Gehlbach, and J. U. Kang, "Active depth-guiding handheld micro-forceps for membranectomy based on cp-ssoct," in *Optical Fibers and Sensors for Medical Diagnostics and Treatment Applications XVI*, vol. 9702. SPIE, 2016, pp. 60–66.

[64] C. N. Riviere, W. T. Ang, and P. K. Khosla, "Toward active tremor canceling in handheld microsurgical instruments," *IEEE Transactions on Robotics and Automation*, vol. 19, no. 5, pp. 793–800, 2003.

[65] R. A. MacLachlan, B. C. Becker, J. C. Tabarés, G. W. Podnar, L. A. Lobes Jr, and C. N. Riviere, "Micron: an actively stabilized handheld tool for microsurgery," *IEEE Transactions on Robotics*, vol. 28, no. 1, pp. 195–212, 2011.

[66] N. Patel, M. Urias, A. Ebrahimi, P. Gehlbach, and I. Iordachita, "Scleral force evaluation during vitreoretinal surgery: in an in vivo rabbit eye model," in *2020 42nd Annual International Conference of the IEEE Engineering in Medicine & Biology Society (EMBC)*. IEEE, 2020, pp. 6049–6053.

[67] S. Sunshine, M. Balicki, X. He, K. Olds, J. U. Kang, P. Gehlbach, R. Taylor, I. Iordachita, and J. T. Handa, "A force-sensing microsurgical instrument that detects forces below human tactile sensation," *Retina (Philadelphia, Pa.)*, vol. 33, no. 1, 2013.

[68] H. Zhang, H. Yi, Z. Fan, L. Pang, M. Bai, C. Wang, and J. Zhao, "An fbg-based 3-DoF force sensor with simplified structure for retinal microsurgery," *IEEE Sensors Journal*, vol. 22, no. 15, pp. 14 911–14 920, 2022.

[69] J. Li, C. Wang, Z. Mao, Y. Liu, Z. Wang, and H. Liu, "A compact fbg-based triaxial force sensor with parallel helical beams for robotic-assisted surgery," *IEEE Transactions on Instrumentation and Measurement*, vol. 71, pp. 1–9, 2022.

[70] S. Sefati, R. Hegeman, I. Iordachita, R. H. Taylor, and M. Armand, "A dexterous robotic system for autonomous debridement of osteolytic bone lesions in confined spaces: Human cadaver studies," *IEEE Transactions on Robotics*, vol. 38, no. 2, pp. 1213–1229, 2021.

[71] S. Sefati, F. Alambeigi, I. Iordachita, M. Armand, and R. J. Murphy, "FBG-based large deflection shape sensing of a continuum manipulator: Manufacturing optimization," in *2016 IEEE SENSORS*. IEEE, 2016, pp. 1–3.

[72] D. Tosi, E. Macchi, G. Braschi, M. Gallati, A. Cigada, S. Poeggel, G. Leen,

and E. Lewis, "Monitoring of radiofrequency thermal ablation in liver tissue through Fiber Bragg Grating sensors array," *Electronics Letters*, vol. 50, no. 14, pp. 981–983, 2014.

[73] X. He, M. Balicki, P. Gehlbach, J. Handa, R. Taylor, and I. Iordachita, "A multi-function force sensing instrument for variable admittance robot control in retinal microsurgery," in *Robotics and Automation (ICRA), 2014 IEEE International Conference on*. IEEE, 2014, pp. 1411–1418.

[74] A. Gijbels, E. B. Vander Poorten, P. Stalmans, and D. Reynaerts, "Development and experimental validation of a force sensing needle for robotically assisted retinal vein cannulations," in *2015 IEEE International Conference on Robotics and Automation (ICRA)*. IEEE, 2015, pp. 2270–2276.

[75] J. Weiss, N. Rieke, M. A. Nasseri, M. Maier, A. Eslami, and N. Navab, "Fast 5-DoF needle tracking in iOCT," *International journal of computer assisted radiology and surgery*, vol. 13, no. 6, pp. 787–796, 2018.

[76] J. Ehlers, "Intraoperative optical coherence tomography: past, present, and future," *Eye*, vol. 30, no. 2, pp. 193–201, 2016.

[77] H. Yu, J.-H. Shen, K. M. Joos, and N. Simaan, "Design, calibration and preliminary testing of a robotic telemanipulator for oct guided retinal

surgery," in *2013 IEEE International Conference on Robotics and Automation*. IEEE, 2013, pp. 225–231.

[78] Y. Koyama, M. M. Marinho, M. Mitsuishi, and K. Harada, "Autonomous coordinated control of the light guide for positioning in vitreoretinal surgery," *IEEE Transactions on Medical Robotics and Bionics*, vol. 4, no. 1, pp. 156–171, 2022.

[79] J. P. Ehlers, Y. S. Modi, P. E. Pecen, J. Goshe, W. J. Dupps, A. Rachitskaya, S. Sharma, A. Yuan, R. Singh, and P. K. Kaiser, "The discover study 3-year results: feasibility and usefulness of microscope-integrated intraoperative oct during ophthalmic surgery," *Ophthalmology*, vol. 125, no. 7, pp. 1014–1027, 2018.

[80] Y. Li, W. Zhang, V. P. Nguyen, R. Rosen, X. Wang, X. Xia, and Y. M. Paulus, "Real-time OCT guidance and multimodal imaging monitoring of subretinal injection induced choroidal neovascularization in rabbit eyes," *Experimental eye research*, vol. 186, p. 107714, 2019.

[81] N. Z. Gregori, B. L. Lam, and J. L. Davis, "Intraoperative use of microscope-integrated optical coherence tomography for subretinal gene therapy delivery," *Retina*, vol. 39, pp. S9–S12, 2019.

[82] M. Sommersperger, J. Weiss, M. A. Nasseri, P. Gehlbach, I. Iordachita, and N. Navab, "Real-time tool to layer distance estimation for robotic

subretinal injection using intraoperative 4D OCT," *Biomedical Optics Express*, vol. 12, no. 2, pp. 1085–1104, 2021.

[83] M. A. Nasseri, M. Maier, and C. P. Lohmann, "A targeted drug delivery platform for assisting retinal surgeons for treating age-related macular degeneration (AMD)," in *39th Annual International Conference of the IEEE Engineering in Medicine and Biology Society (EMBC)*. IEEE, 2017, pp. 4333–4338.

[84] J. Smits, A. Gijbels, K. Willekens, B. Stanzel, and D. Reynaerts, "Robot-assisted subretinal surgery: initial in-vivo animal validation," *Hamlyn Symposium on Medical Robotics 2018*, pp. 91–92, 2018.

[85] B. C. Becker, S. Voros, L. A. Lobes, J. T. Handa, G. D. Hager, and C. N. Riviere, "Retinal vessel cannulation with an image-guided handheld robot," in *2010 Annual International Conference of the IEEE Engineering in Medicine and Biology*. IEEE, 2010, pp. 5420–5423.

[86] E. Rahimy, J. Wilson, T. Tsao, S. Schwartz, and J. Hubschman, "Robot-assisted intraocular surgery: development of the iriss and feasibility studies in an animal model," *Eye*, vol. 27, no. 8, pp. 972–978, 2013.

[87] Y. Noda, Y. Ida, S. Tanaka, T. Toyama, M. F. Roggia, Y. Tamaki, N. Sugita, M. Mitsuishi, and T. Ueta, "Impact of robotic assistance on precision of vitreoretinal surgical procedures," *PloS one*, vol. 8, no. 1, p. e54116, 2013.

[88] M. D. de Smet, T. C. Meenink, T. Janssens, V. Vanheukelom, G. J. Naus, M. J. Beelen, C. Meers, B. Jonckx, and J.-M. Stassen, "Robotic assisted cannulation of occluded retinal veins," *PloS one*, vol. 11, no. 9, p. e0162037, 2016.

[89] M. D. de Smet, J. M. Stassen, T. C. Meenink, T. Janssens, V. Vanheukelom, G. J. Naus, M. J. Beelen, and B. Jonckx, "Release of experimental retinal vein occlusions by direct intraluminal injection of ocriplasmin," *British Journal of Ophthalmology*, vol. 100, no. 12, pp. 1742–1746, 2016.

[90] B. Keller, M. Draelos, K. Zhou, R. Qian, A. N. Kuo, G. Konidaris, K. Hauser, and J. A. Izatt, "Optical coherence tomography-guided robotic ophthalmic microsurgery via reinforcement learning from demonstration," *IEEE Transactions on Robotics*, vol. 36, no. 4, pp. 1207–1218, 2020.

[91] "Live volumetric (4d."

[92] R. Channa, I. Iordachita, and J. T. Handa, "Robotic eye surgery," *Retina (Philadelphia, Pa.)*, vol. 37, no. 7, p. 1220, 2017.

[93] C. He, E. Yang, N. Patel, A. Ebrahimi, M. Shahbazi, P. Gehlbach, and I. Iordachita, "Automatic light pipe actuating system for bimanual robot-assisted retinal surgery," *IEEE/ASME Transactions on Mechatronics*, vol. 25, no. 6, pp. 2846–2857, 2020.

[94] S. Yang, L. A. Lobes Jr, J. N. Martel, and C. N. Riviere, "Handheld-automated microsurgical instrumentation for intraocular laser surgery," *Lasers in surgery and medicine*, vol. 47, no. 8, pp. 658–668, 2015.

[95] J. W. Kim, C. He, M. Urias, P. Gehlbach, G. D. Hager, I. Iordachita, and M. Kobilarov, "Autonomously navigating a surgical tool inside the eye by learning from demonstration," in *2020 IEEE International Conference on Robotics and Automation (ICRA)*. IEEE, 2020, pp. 7351–7357.

[96] C. He, A. Ebrahimi, M. Roizenblatt, N. Patel, Y. Yang, P. L. Gehlbach, and I. Iordachita, "User behavior evaluation in robot-assisted retinal surgery," in *2018 27th IEEE International Symposium on Robot and Human Interactive Communication (RO-MAN)*. IEEE, 2018, pp. 174–179.

[97] W. Wei and N. Simaan, "Modeling, force sensing, and control of flexible cannulas for microstent delivery," *Journal of Dynamic Systems, Measurement, and Control*, vol. 134, no. 4, 2012.

[98] B. C. Becker, R. A. MacLachlan, L. A. Lobes, G. D. Hager, and C. N. Riviere, "Vision-based control of a handheld surgical micromanipulator with virtual fixtures," *IEEE Transactions on Robotics*, vol. 29, no. 3, pp. 674–683, 2013.

[99] T. Probst, K.-K. Maninis, A. Chhatkuli, M. Ourak, E. Vander Poorten, and L. Van Gool, "Automatic tool landmark detection for stereo vision in

robot-assisted retinal surgery," *IEEE Robotics and Automation Letters*, vol. 3, no. 1, pp. 612–619, 2017.

[100] S. Yang, M. Balicki, R. A. MacLachlan, X. Liu, J. U. Kang, R. H. Taylor, and C. N. Riviere, "Optical coherence tomography scanning with a handheld vitreoretinal micromanipulator," in *2012 Annual International Conference of the IEEE Engineering in Medicine and Biology Society*. IEEE, 2012, pp. 948–951.

[101] H. Yu, J.-H. Shen, K. M. Joos, and N. Simaan, "Calibration and integration of b-mode optical coherence tomography for assistive control in robotic microsurgery," *IEEE/ASME Transactions on Mechatronics*, vol. 21, no. 6, pp. 2613–2623, 2016.

[102] G. W. Cheon, B. Gonenc, R. H. Taylor, P. L. Gehlbach, and J. U. Kang, "Motorized microforceps with active motion guidance based on common-path ssoct for epiretinal membranectomy," *IEEE/ASME Transactions on Mechatronics*, vol. 22, no. 6, pp. 2440–2448, 2017.

[103] M. Zhou, K. Huang, A. Eslami, H. Roodaki, D. Zapp, M. Maier, C. P. Lohmann, A. Knoll, and M. A. Nasseri, "Precision needle tip localization using optical coherence tomography images for subretinal injection," in *2018 IEEE International Conference on Robotics and Automation (ICRA)*. IEEE, 2018, pp. 1–8.

[104] B. C. Becker, R. A. MacLachlan, and C. N. Riviere, "State estimation and feedforward tremor suppression for a handheld micromanipulator with a kalman filter," in *2011 IEEE/RSJ International Conference on Intelligent Robots and Systems*. IEEE, 2011, pp. 5160–5165.

[105] T. Tayama, Y. Kurose, M. M. Marinho, Y. Koyama, K. Harada, S. Omata, F. Arai, K. Sugimoto, F. Araki, K. Totsuka *et al.*, "Autonomous positioning of eye surgical robot using the tool shadow and kalman filtering," in *2018 40th Annual International Conference of the IEEE Engineering in Medicine and Biology Society (EMBC)*. IEEE, 2018, pp. 1723–1726.

[106] J. W. Kim, P. Zhang, P. Gehlbach, I. Iordachita, and M. Kobilarov, "Towards autonomous eye surgery by combining deep imitation learning with optimal control," *Proceedings of Machine Learning Research*, vol. 155, p. 2347, 2021.

[107] A. Chan, J. S. Duker, T. H. Ko, J. G. Fujimoto, and J. S. Schuman, "Normal macular thickness measurements in healthy eyes using stratus optical coherence tomography," *Archives of ophthalmology*, vol. 124, no. 2, pp. 193–198, 2006.

[108] A. Gijbels, N. Wouters, P. Stalmans, H. Van Brussel, D. Reynaerts, and E. Vander Poorten, "Design and realisation of a novel robotic manipula-

tor for retinal surgery," in *Intelligent Robots and Systems (IROS), 2013 IEEE/RSJ International Conference on*. IEEE, 2013, pp. 3598–3603.

[109] T. Ueta, Y. Yamaguchi, Y. Shirakawa, T. Nakano, R. Ideta, Y. Noda, A. Morita, R. Mochizuki, N. Sugita, M. Mitsuishi *et al.*, "Robot-assisted vitreoretinal surgery: Development of a prototype and feasibility studies in an animal model," *Ophthalmology*, vol. 116, no. 8, pp. 1538–1543, 2009.

[110] R. A. MacLachlan, B. C. Becker, J. C. Tabarés, G. W. Podnar, L. A. Lobes Jr, and C. N. Riviere, "Micron: an actively stabilized handheld tool for microsurgery," *IEEE transactions on robotics: a publication of the IEEE Robotics and Automation Society*, vol. 28, no. 1, p. 195, 2012.

[111] D. Braun, S. Yang, J. N. Martel, C. N. Riviere, and B. C. Becker, "Eye-SLAM: Real-time simultaneous localization and mapping of retinal vessels during intraocular microsurgery," *The International Journal of Medical Robotics and Computer Assisted Surgery*, vol. 14, no. 1, p. e1848, 2018.

[112] S. Yang, J. N. Martel, L. A. Lobes Jr, and C. N. Riviere, "Techniques for robot-aided intraocular surgery using monocular vision," *The International Journal of Robotics Research*, vol. 37, no. 8, pp. 931–952, 2018.

[113] C. He, N. Patel, A. Ebrahimi, M. Kobilarov, and I. Iordachita, "Prelimi-

nary study of an RNN-based active interventional robotic system (airs) in retinal microsurgery," *International Journal of Computer Assisted Radiology and Surgery*, vol. 14, no. 6, pp. 945–954, 2019.

[114] C. He, N. Patel, M. Shahbazi, Y. Yang, P. Gehlbach, M. Kobilarov, and I. Iordachita, "Toward safe retinal microsurgery: Development and evaluation of an rnn-based active interventional control framework," *IEEE Transactions on Biomedical Engineering*, vol. 67, no. 4, pp. 966–977, 2019.

[115] A. Ebrahimi, C. He, M. Roizenblatt, N. Patel, S. Sefati, P. Gehlbach, and I. Iordachita, "Real-time sclera force feedback for enabling safe robot-assisted vitreoretinal surgery," in *2018 40th Annual International Conference of the IEEE Engineering in Medicine and Biology Society (EMBC)*, July 2018, pp. 3650–3655.

[116] R. M. Murray, Z. Li, S. S. Sastry, and S. S. Sastry, *A Mathematical Introduction to Robotic Manipulation*. CRC press, 1994.

[117] A. Ebrahimi, N. Patel, C. He, P. Gehlbach, M. Kobilarov, and I. Iordachita, "Adaptive control of sclera force and insertion depth for safe robot-assisted retinal surgery," in *2019 International Conference on Robotics and Automation (ICRA)*. IEEE, 2019, pp. 9073–9079.

[118] J. Roy and L. L. Whitcomb, "Adaptive force control of position/velocity

controlled robots: theory and experiment," *IEEE Transactions on Robotics and Automation*, vol. 18, no. 2, pp. 121–137, 2002.

[119] A. Deguet, R. Kumar, R. Taylor, and P. Kazanzides, "The cisst libraries for computer assisted intervention systems," in *MICCAI Workshop on Systems and Arch. for Computer Assisted Interventions, Midas Journal*, vol. 71, 2008.

[120] M. Dewan, P. Marayong, A. M. Okamura, and G. D. Hager, "Vision-based assistance for ophthalmic micro-surgery," in *International Conference on Medical Image Computing and Computer-Assisted Intervention*. Springer, 2004, pp. 49–57.

[121] H. Hibbler, "Mechanics of Materials SI Edition," Pearson Prentice Hall, Singapore, 2004.

[122] D. Simon, *Optimal State Estimation: Kalman, H-infinity, and Nonlinear Approaches*. John Wiley & Sons, 2006.

[123] H. M. Choset, S. Hutchinson, K. M. Lynch, G. Kantor, W. Burgard, L. E. Kavraki, and S. Thrun, *Principles of robot motion: theory, algorithms, and implementation*. MIT press, 2005.

[124] R. Hartley and A. Zisserman, *Multiple View Geometry in Computer Vision*. Cambridge University Press, 2003.

[125] P. J. Besl and N. D. McKay, "Method for registration of 3D shapes," in *Sensor fusion IV: Control Paradigms and Data Structures*, vol. 1611. International Society for Optics and Photonics, 1992, pp. 586–606.

[126] M. Quigley, K. Conley, B. Gerkey, J. Faust, T. Foote, J. Leibs, R. Wheeler, and A. Y. Ng, "ROS: an open-source robot operating system," in *ICRA workshop on open source software*, vol. 3, no. 3.2. Kobe, Japan, 2009, p. 5.

[127] C. Yang, Y. Xie, S. Liu, and D. Sun, "Force modeling, identification, and feedback control of robot-assisted needle insertion: a survey of the literature," *Sensors*, vol. 18, no. 2, p. 561, 2018.

[128] A. Asadian, R. V. Patel, and M. R. Kermani, "Dynamics of translational friction in needle–tissue interaction during needle insertion," *Annals of Biomedical Engineering*, vol. 42, no. 1, pp. 73–85, 2014.

[129] L. Barbé, B. Bayle, M. de Mathelin, and A. Gangi, "In vivo model estimation and haptic characterization of needle insertions," *The International Journal of Robotics Research*, vol. 26, no. 11-12, pp. 1283–1301, 2007.

[130] Y. Fukushima and K. Naemura, "Estimation of the friction force during the needle insertion using the disturbance observer and the recursive least square," *Robomech Journal*, vol. 1, no. 1, pp. 1–8, 2014.

[131] M. Zhou, H. Roodaki, A. Eslami, G. Chen, K. Huang, M. Maier, C. P. Lohmann, A. Knoll, and M. A. Nasseri, “Needle segmentation in volumetric optical coherence tomography images for ophthalmic microsurgery,” *Applied Sciences*, vol. 7, no. 8, p. 748, 2017.

[132] A. Mehrtash, M. Ghafoorian, G. Pernelle, A. Ziaei, F. G. Heslinga, K. Tuncali, A. Fedorov, R. Kikinis, C. M. Tempany, W. M. Wells *et al.*, “Automatic needle segmentation and localization in MRI with 3D convolutional neural networks: application to mri-targeted prostate biopsy,” *IEEE Transactions on Medical Imaging*, vol. 38, no. 4, pp. 1026–1036, 2018.